DTIC FILE COPY

AFWAL-TR-88-2007

A NUMERICAL SIMULATION OF THE FLOW FIELD
AND HEAT TRANSFER IN A RECTANGULAR PASSAGE
WITH A TURBULENCE PROMOTER

DTIC
ELECTE
AUG 0 5 1988
D

Bryan R. Becker, Ph.D., P.E.
University of Missouri
Kansas City, MO

Richard B. Rivir, Ph.D.
Components Branch
Turbine Engine Division

June 1988

Final Report for Period June 1987 - September 1987

NOTICE

WHEN GOVERNMENT DRAWINGS, SPECIFICATIONS, OR OTHER DATA ARE USED FOR ANY PURPOSE OTHER THAN IN CONNECTION WITH A DEFINITELY GOVERNMENT-RELATED PROCUREMENT, THE UNITED STATES GOVERNMENT INCURS NO RESPONSIBILITY OR ANY OBLIGATION WHATSOEVER. THE FACT THAT THE GOVERNMENT MAY HAVE FORMULATED OR IN ANY WAY SUPPLIED THE SAID DRAWINGS, SPECIFICATIONS, OR OTHER DATA, IS NOT TO BE REGARDED BY IMPLICATION, OR OTHERWISE IN ANY MANNER CONSTRUED, AS LICENSING THE HOLDER, OR ANY OTHER PERSON OR CORPORATION; OR AS CONVEYING ANY RIGHTS OR PERMISSION TO MANUFACTURE, USE, OR SELL ANY PATENTED INVENTION THAT MAY IN ANY WAY BE RELATED THERETO.

THIS REPORT HAS BEEN REVIEWED BY THE OFFICE OF PUBLIC AFFAIRS (ASD/CPA) AND IS RELEASABLE TO THE NATIONAL TECHNICAL INFORMATION SERVICE (NTIS). AT NTIS, IT WILL BE AVAILABLE TO THE GENERAL PUBLIC, INCLUDING FOREIGN NATIONS.

THIS TECHNICAL REPORT HAS BEEN REVIEWED AND IS APPROVED FOR PUBLICATION.

R. B. RIVIR
Project Engineer
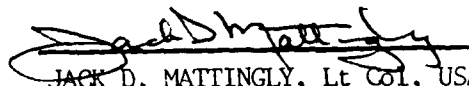
JACK D. MATTINGLY, Lt Col, USAF
Chief, Components Branch

FOR THE COMMANDER
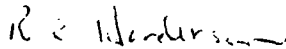
R. E. HENDERSON
Deputy for Technology
Turbine Engine Division

IF YOUR ADDRESS HAS CHANGED, IF YOU WISH TO BE REMOVED FROM OUR MAILING LIST, OR IF THE ADDRESSEE IS NO LONGER EMPLOYED BY YOUR ORGANIZATION PLEASE NOTIFY AFWAL/POTC , WRIGHT-PATTERSON AFB, OH 45433-6563 TO HELP MAINTAIN A CURRENT MAILING LIST.

COPIES OF THIS REPORT SHOULD NOT BE RETURNED UNLESS RETURN IS REQUIRED BY SECURITY CONSIDERATIONS, CONTRACTUAL OBLIGATIONS, OR NOTICE ON A SPECIFIC DOCUMENT.

REPORT DOCUMENTATION PAGE			Form Approved OMB No. 0704-0188

1a. REPORT SECURITY CLASSIFICATION UNCLASSIFIED		1b. RESTRICTIVE MARKINGS N/A	
2a. SECURITY CLASSIFICATION AUTHORITY N/A		3. DISTRIBUTION/AVAILABILITY OF REPORT Approved for public; distribution unlimited.	
2b. DECLASSIFICATION/DOWNGRADING SCHEDULE N/A			
4. PERFORMING ORGANIZATION REPORT NUMBER(S) AFWAL-TR-88-2007		5. MONITORING ORGANIZATION REPORT NUMBER(S)	

6a. NAME OF PERFORMING ORGANIZATION Components Branch	6b. OFFICE SYMBOL (If applicable) AFWAL/POTC	7a. NAME OF MONITORING ORGANIZATION
6c. ADDRESS (City, State, and ZIP Code) AFWAL/POTC Wright-Patterson AFB OH 45433-6563		7b. ADDRESS (City, State, and ZIP Code)
8a. NAME OF FUNDING/SPONSORING ORGANIZATION AFOSR	8b. OFFICE SYMBOL (If applicable) AFOSR/NA	9. PROCUREMENT INSTRUMENT IDENTIFICATION NUMBER

8c. ADDRESS (City, State, and ZIP Code) Bolling Air Force Base Washington DC 20332	10. SOURCE OF FUNDING NUMBERS			
	PROGRAM ELEMENT NO 61102F	PROJECT NO. 2307	TASK NO A3	WORK UNIT ACCESSION NO 15

11. TITLE (Include Security Classification) A Numerical Simulation of the Flow Field and Heat Transfer in a Rectangular Passage with a Turbulence Promoter

12. PERSONAL AUTHOR(S) Bryan R. Becker and Richard B. Rivir

13a. TYPE OF REPORT FINAL	13b. TIME COVERED FROM Jun 87 TO Sep 87	14. DATE OF REPORT (Year, Month, Day) June 1988	15. PAGE COUNT 92

16. SUPPLEMENTARY NOTATION

17. COSATI CODES			18. SUBJECT TERMS (Continue on reverse if necessary and identify by block number)
FIELD	GROUP	SUB-GROUP	Heat Transfer, Turbulence Augmentation
11	02		
11	04		

19. ABSTRACT (Continue on reverse if necessary and identify by block number)

A numerical study of the flow field and heat transfer in a turbine blade internal cooling passage is described. Attention is focused on a short straight section of the rectangular passage which includes a single turbulator protruding from its floor. The two dimensional, transient, Reynolds averaged Navier Stokes, continuity and energy equations are iterated to a steady state solution using the MacCormack explicit predictor-corrector algorithm. Turbulence closure is achieved through the use of the Baldwin-Lomax form of the Cebeci-Smith algebraic two layer eddy viscosity model.

Plots of skin friction, local heat transfer rate, streamlines, velocity profiles and temperature profiles are given. It was found that the widely used Reynolds Analogy greatly underpredicts the heat transfer rate as given by a direct calculation using Fourier's law.

20. DISTRIBUTION/AVAILABILITY OF ABSTRACT ☒ UNCLASSIFIED/UNLIMITED ☐ SAME AS RPT ☐ DTIC USERS	21. ABSTRACT SECURITY CLASSIFICATION UNCLASSIFIED	
22a. NAME OF RESPONSIBLE INDIVIDUAL RICHARD B. RIVIR	22b. TELEPHONE (Include Area Code) 513/255-6768	22c. OFFICE SYMBOL AFWAL/POTC

DD Form 1473, JUN 86   Previous editions are obsolete   SECURITY CLASSIFICATION OF THIS PAGE

UNCLASSIFIED

TABLE OF CONTENTS

LIST OF ILLUSTRATIONS

INTRODUCTION

In the design of the advanced gas turbine engines, which will power the Nation's future aircraft, there are numerous fluid flow and heat transfer phenomena which need to be better understood. As gas turbine operating speeds, temperatures, and pressures increase, the heat loads on the turbine blades increase which can result in high metal temperatures and structural failure caused by thermal stress concentrations due to severe thermal gradients. To reduce the effects of these heat loads, cooling air is extracted from the compressor and is routed through small rectangular cooling passages within the turbine blades.

The cooling air enters the root of each turbine blade and flows through complex, serpentine passages until it exits through the blade's surface into the cavity surrounding the turbine rotor-stator. Since the pressure drop, and thus the mass flowrate, along these cooling passages is limited by the pressure differential between the compressor and the turbine stage, methods other than increased coolant flow, such as the introduction of turbulators, must be used to enhance the heat transfer. These turbulators or turbulence promoters, which consist of ribs protruding from the walls of the internal cooling passages, increase the turbulence level within the cooling air flow and thus augment the rate of energy transfer from the turbine blade through the cooling passage wall and into the cooling air flow. Thus, the resulting coolant flows contain many complex phenomena which are not adequately included in the current heat transfer design of turbine blades. The detailed modeling of these flows is essential to the accurate prediction of the distribution of the local heat transfer coefficient along the cooling

passages. Such prediction is necessary to achieve a thermal design of these components which incorporates efficient cooling and thereby alleviates the effects of the increased heat load.

There have been numerous experimental and analytical studies of the fluid flow and heat transfer within straight rectangular ducts which simulate the flow within the internal cooling passages inside a turbine blade. Several investigators have studied the phenomena of secondary flows in ducts with noncircular cross section. These secondary flows, transverse to the main flow direction, are composed of eight counter-rotating vortices which convect momentum, vorticity and total energy into the corners of the duct.

In an early study, Gessner and Jones [6] utilized hot wire anemometry to study secondary flow effects in fully developed turbulent air flows within rectangular channels. They studied flows in channels with smooth internal surfaces and reported that the secondary flow velocity, when normalized by the axial mean flow velocity, decreased with increasing Reynolds number. They also deduced that secondary flows, composed of eight counterrotating streamwise vortices, are caused by an imbalance between Reynolds stresses and static pressure gradients. However, they presented no heat transfer results.

Launder and Ying [10] expanded upon the work of Gessner and Jones [6] by again using hot wire anemometry to study secondary air flows in a duct of square cross section. However, they considered ducts whose surfaces were roughened with transverse mounted square turbulators and concluded that the secondary flow velocity, when normalized by the average friction velocity, became independent of Reynolds number and surface roughness. Again, no heat transfer results were reported.

Later, Gessner [5] reported a detailed analysis of the mechanisms which initiate secondary flow in developing turbulent air flow along a corner. He concluded that transverse gradients of the Reynolds shear stress components are responsible for the generation of secondary flow within turbulent flows along a corner. Also, he reiterated that secondary flows act as a significant convective transport agent of the momentum, vorticity and total energy of the main axial motion.

Melling and Whitelaw [12] were the first investigators to apply laser-Doppler anemometry to the study of secondary flows within developing turbulent flow inside rectangular ducts. They used water as the working fluid and their results confirm the qualitative results published by earlier investigators but they indicated quantitative differences. Their data are valuable for the verification of mathematical turbulence models. Also, their work showed that the developing flow is much more sensitive to inlet conditions than is a nominally fully developed flow. They did not study heat transfer effects.

In summary, the focus of the above mentioned experimental investigations was upon the cause and structure of secondary flows within turbulent flows inside rectangular ducts. None of these investigations studied the heat transfer phenomena occurring within these duct flows.

Experimental studies more closely related to the thermal design of turbine blade cooling passages began to appear in the 1980's. For example, Han [7] studied the effects of square turbulator geometry upon the heat transfer coefficient and friction factor in fully developed turbulent air flow through a square duct with two opposite ribbed walls.

He used a blower to force room air through a test section consisting of
four heated aluminum plates of which the two vertical plates were
ribbed. The heaters were independently controlled so as to provide a
controllable constant heat flux throughout the test section. The test
section was instrumented with thermocouples and pressure taps while the
inlet air flowrate and temperature as well as the exit air temperature
were monitored. The friction factor was determined from the pressure
drop data and the Stanton number was determined from the air and wall
temperatures with the constant wall heat flux as a known boundary
condition. In this investigation Han studied the effects of rib height
to equivalent duct diameter (H/D) and rib height to rib pitch or spacing
along the duct (H/P). He reports that both the friction factor and the
Stanton number increase with increasing H/D and likewise for increasing
H/P. He also presents an empirical prediction method for determining
the friction factor and the Stanton number for flows with this geometry.

In an additional study using the same experimental techniques, Han
et al [9] investigated the combined effects of rib angle of attack (α)
and rib height to pitch (H/P). They report that the maximum heat
transfer and friction factor occurred at α of 60-75 degrees. They also
report that as α decreased from 90 degrees to approximately 45-30
degrees, the heat conductance, at a constant pressure drop, increased to
its maximum value while the pressure drop required for a constant heat
transfer rate decreased to its minimum value. Thus, it appears that an
angle of attack in the range of 45-30 degrees produces the optimal
thermal performance for a given axial pressure drop. They also report
that as the H/P ratio decreases the same trends are evident but are
relatively reduced.

Finally, Han et al [8] measured the combined effects of rib angle
of attack (α) and duct aspect ratio. Whereas previous work by Han had
been concerned with ducts of square cross section, this study involved
rectangular ducts whose ribbed walls were 2 to 4 times wider than their
smooth walls. They found that, for this type of duct, the heat transfer
and friction factor varied only slightly as α varied from 45 degrees to
90 degrees, with the maximums occurring at α equal to 90 degrees. They
also found that the heat transfer and friction factor increased as the
width of the ribbed wall increased relative to the width of the smooth
wall.

Several numerical studies of the flows in rectangular channels with
turbulators have also been reported. For example, Durst and Rastogi
[3] performed both experimental and numerical studies of the turbulent
flow over a transverse mounted square turbulator in a two dimensional
channel. Their experimental work involved the use of a one dimensional
laser-Doppler anemometer to measure turbulence characteristics in a
plane two dimensional water channel. They used the TEACH numerical
algorithm with a K-ε turbulence model to simulate the two dimensional
flow in the recirculation region near the turbulator. However, the
velocity and turbulence profiles near the wall as well as the wall shear
stress and hence the heat transfer at the wall were all determined by a
"law of the wall" rather than calculated as part of a detailed numerical
analysis.

Fujita et al [4] numerically analyzed fully developed turbulent
flow in a square duct with two opposite roughened walls. They used a
stream function-vorticity formulation to solve for the flow field in
planes orthogonal to the main flow direction and then marched this

solution in the streamwise direction. Their results show the presence of only four streamwise vortices rather than the eight reported by the experimentalists mentioned above. Also, their calculations were performed on a very coarse 11 by 11 uniform mesh over a quadrant of the cross section of a rectangular duct and hence do not capture much of the detail of the heat transfer phenomena near the solid wall.

Linton and Shang [11] investigated jet impingement cooling of turbine blades in a rotating frame of reference. They numerically solved the laminar three-dimensional, compressible Navier-Stokes equations to yield a description of the flow field for both rotating and stationary cases. However, their calculations omitted both the effects of turbulence and surface roughness.

In conclusion, the authors feel that there remains a need for the detailed numerical modeling of the heat transfer and fluid flow processes very near the fluid-solid interface. This paper reports on an initial, two dimensional modeling effort which begins to address this need. In terms of long range goals, this detailed numerical model will be expanded to include the effects of rotation, multiple turbulence promoters and three dimensional secondary flows. In this way, as more detail and completeness is added to the model, the local heat transfer rate along the cooling passage will be more accurately predicted, thereby enabling the optimization of cooling configuration design prior to full scale prototype testing and at a greatly reduced cost. This optimal heat transfer design will result in lower metal temperatures and reduced thermal gradients, thus enabling the turbine blades to withstand the increased operating conditions necessary to improve engine efficiency.

SECTION II

THE NUMERICAL MODEL

A. Computational Domain

In this initial numerical study of the fluid flow and heat transfer
in a turbine blade internal cooling passage, attention is focused on a
two dimensional flow over a single turbulator of approximately square
cross section which protrudes upward from the floor of the passage,
transverse to the main flow direction. The X-coordinate is oriented
along the length of the passage, coincident with the bulk flow direction
while the Y-coordinate is oriented in the direction of the turbulator
height, normal to the passage floor. This two dimensional
approximation, which greatly reduces the computational complexity and
cost, is considered to be sufficient for this initial study. The
accuracy of this two dimensional assumption increases as the passage
aspect ratio (height/transverse width) decreases and is a very
reasonable numerical approximation to the experimental study reported by
Han et al [8] for a passage aspect of 0.25.

An outline of the computational mesh or domain is shown in Figure
1. The main flow direction is from left to right with the left and
right boundaries being the inflow and outflow boundaries, respectively.
The lower boundary is a solid wall boundary while the top boundary is a
symmetry boundary which simulates the centerline of the flow passage.
The turbulence promoter or rib is modelled as an obstruction protruding
upward from the bottom boundary with a flat top whose length in the
streamwise direction is equal to its height. The upstream and down-
stream faces of the rib are modelled as $\sin [(x \cdot a)/(2 \cdot \text{rib height})]$,

so that the total width of the rib is three rib heights, measured from the point of departure from horizontal to the point of return to horizontal.

The computational domain extends 20.0 rib heights in the streamwise X-direction and 4.2 rib heights in the vertical Y-direction with the upstream face of the rib beginning its departure from horizontal at approximately 4.0 rib heights from the inflow boundary. There are 100 grid lines in the X-direction, clustered around the turbulence promoter with the distance between grid lines growing geometrically from an initial spacing of 0.1 rib heights. There are 60 grid lines in the vertical Y-direction with 44 within the first rib height which is well within the turbulent boundary layer. The mesh spacing grows in the Y-direction as a geometric progression from an initial spacing of 0.01 rib heights. From this description, it can be seen that the computational mesh has very high resolution and is capable of revealing considerable detail of the flow field and heat transfer near the turbulence promoter.

B. Governing Equations

The governing equations for this simulation consist of the two dimensional, Reynolds averaged form of the following turbulent, compressible, unsteady equations -- continuity, viscous Navier Stokes, and energy:

$$\frac{\partial \rho}{\partial t} + \vec{\nabla} \cdot (\rho \vec{u}) = 0 \tag{1}$$

$$\frac{\partial (\rho \vec{u})}{\partial t} + \vec{\nabla} \cdot (\rho \vec{u}\vec{u} - \bar{\tau}) = 0 \tag{2}$$

$$\frac{\partial (\rho e)}{\partial t} + \vec{\nabla} \cdot (\rho e \vec{u} - \bar{\tau} \cdot \vec{u} + \vec{q}) = 0 \tag{3}$$

8

The dependent variables in these equations are the time averaged values of density, x-momentum, y-momentum and total energy: ρ, ρu, ρv, and $\rho e = \rho [c_v T + \frac{1}{2}(u^2 + v^2)]$.

The Reynolds averaging of the turbulent equations produces components of Reynolds stress which appear in the stress tensor, $\bar{\bar{\tau}}$, and correlations of velocity and temperature fluctuations which appear in the heat flux vector, $\vec{q}$. The required turbulence closure is achieved through the use of the Baldwin-Lomax form of the Cebeci-Smith algebraic two layer eddy viscosity model [1]. The Reynolds stress components are then modelled as the product of the eddy viscosity, ϵ, times the velocity gradient of the mean flow while the correlations of velocity and temperature fluctuations are represented with a turbulent Prandtl number ($Pr_t = 0.9$):

$$\tau_{ij} = (\mu + \epsilon)\left(\frac{\partial u_i}{\partial x_j} + \frac{\partial u_j}{\partial x_i}\right) - \left[\frac{2}{3}(\mu + \epsilon)\left(\frac{\partial u_i}{\partial x_j}\right) + P_i\right]\delta_{ij} \tag{4}$$

$$q_i = -c_p\left(\frac{\mu}{Pr} + \frac{\epsilon}{Pr_t}\right)\frac{\partial T}{\partial x_i} \tag{5}$$

Sutherland's law is used to calculate the molecular viscosity of air, μ, as a function of temperature. The molecular Prandtl number, Pr, is assumed to have a constant value of 0.73 while the constant volume specific heat of air, c_v, is taken to be 4290.0 ft^2/s^2-°R; ($\gamma = c_p/c_v = 1.4$). The equation of state is assumed to be the ideal gas law with the gas constant for air equal to 1716.0 ft^2/s^2-°R.

As shown in Figure 1, the (X,Y) coordinate system is a body fitted coordinate system which is deformed to account for the rib on the lower boundary. This deformed coordinate system results in computational cells which are not rectangular but rather distorted quadrilaterals. In

order to maintain second order calculational accuracy in the spatial domain, a coordinate transformation is made to a uniform rectangular (ξ, η) grid. By means of the chain rule, the governing equations in the transformed space can be written in conservation law form as follows:

$$\frac{\partial \vec{U}}{\partial t} + \xi_x \frac{\partial \vec{F}}{\partial \xi} + \eta_x \frac{\partial \vec{F}}{\partial \eta} + \xi_y \frac{\partial \vec{G}}{\partial \xi} + \eta_y \frac{\partial \vec{G}}{\partial \eta} = 0 \tag{6}$$

In Equation (6), ξ_x, η_x, ξ_y, and η_y are the first order partial derivatives of the transformed independent variables (ξ, η) with respect to the coordinates (X, Y), and the vectors $\vec{U}$, $\vec{F}$ and $\vec{G}$ are defined as follows:

$$\vec{U} = \begin{Bmatrix} \rho \\ \rho u \\ \rho v \\ \rho e \end{Bmatrix} \tag{7}$$

$$\vec{F} = \begin{Bmatrix} \rho u \\ \rho u^2 - \tau_{xx} \\ \rho uv - \tau_{xy} \\ (\rho e - \tau_{xx})u - v\tau_{xy} + q_x \end{Bmatrix} \tag{8}$$

$$\vec{G} = \begin{Bmatrix} \rho v \\ \rho uv - \tau_{xy} \\ \rho v^2 - \tau_{yy} \\ (\rho e - \tau_{yy})v - u\tau_{xy} + q_y \end{Bmatrix} \tag{9}$$

This set of equations along with the appropriate boundary and initial conditions constitutes the mathematical model of the cooling air flow through a rectangular passage with a turbulence promoter.

C. Boundary Conditions

Specification of appropriate and consistent boundary conditions is essential to achieving a realistic and stable numerical solution for any fluid flow or heat transfer problem. In the current simulation there are four boundaries which must be considered: bottom, top, inflow, and outflow. Since there are four unknowns, then at each boundary, four conditions must be specified.

The bottom boundary, $J = 1$, is a solid, isothermal, no slip boundary maintained at $T_{wall} = 580.0°R$, which implies the following conditions:

$$(\rho u)_{J=1} = (\rho v)_{J=1} = 0 \tag{10}$$

$$(\rho e)_{J=1} = \rho_{wall} c_v T_{wall} \tag{11}$$

The assumption that the normal derivative of the pressure vanishes at the wall, coupled with the specification of the wall temperature, implies the following condition on the density at the wall:

$$(\rho)_{J=1} = \rho_{wall} = \frac{(\rho T)_{J=2}}{T_{wall}} \tag{12}$$

The top boundary, $J = JMAX$, which is located at the centerline of the rectangular passage, is a symmetry boundary within the free stream. Symmetry implies that the vertical velocity vanishes:

$$(\rho v)_{JMAX} = 0 \tag{13}$$

Since the top boundary is within the free stream, the horizontal velocity, pressure, temperature, and density are all equal to the free stream values which are specified as follows:

$$u_\infty = 262.21 \text{ ft/s} \tag{14}$$

$$P_\infty = 2116.8 \text{ lb}_f/\text{ft}^2 \tag{15}$$

$$T_\infty = 540.0°R \tag{16}$$

$$\rho_\infty = 0.002284 \text{ lb}_f \cdot s^2/ft^4 \tag{17}$$

These specifications imply the following boundary conditions:

$$\rho_{JMAX} = \rho_\infty \tag{18}$$

$$(\rho u)_{JMAX} = \rho_\infty u_\infty \tag{19}$$

$$(\rho e)_{JMAX} = \rho_\infty [c_v T_\infty + \tfrac{1}{2} (u_\infty)^2] \tag{20}$$

At the upstream inflow boundary, $I = 1$, it is assumed that the flow experiences reversible, adiabatic acceleration from stagnation conditions in a settling tank upstream of the inflow boundary. To determine the corresponding stagnation temperature and pressure, it is assumed that the air in the settling tank contains the total energy of the free stream. That is, the stagnation temperature and pressure are determined by applying the first law of thermodynamics and Bernoulli's equation to a reversible adiabatic total deceleration from the free stream velocity, pressure, and temperature specified above in Equations (14) through (16). The resulting stagnation temperature and pressure are thus calculated to have the following values:

$$T_o = 545.72°R \tag{21}$$

$$P_o = 2195.33 \; lb_f/ft^2 \tag{22}$$

These upstream settling tank conditions are then used to determine the inflow boundary conditions. First, it is assumed that the flow has been conditioned prior to entering the rectangular passage so that it enters as parallel flow with no vertical component which imposes the following boundary condition on vertical momentum:

$$(\rho v)_{I=1} = 0 \tag{23}$$

Second, it is assumed that the normal gradient of the temperature vanishes at the inflow which implies that the temperature is extrapolated from the interior of the flow field:

$$T_{I=1} = T_{I=2} \tag{24}$$

12

Thus, the horizontal velocity component can be calculated by applying the first law to the reversible adiabatic acceleration of the air from the settling tank:

$$u_{I=1} = [2c_p(T_0-T_1)]^{1/2} \tag{25}$$

The isentropic pressure relation is then used to determine the pressure at the inflow:

$$P_{I=1} = P_o(T_1/T_0)^{\gamma/\gamma-1} \tag{26}$$

Finally, the boundary condition on the density at the inflow is given by using the ideal gas law:

$$\rho_{I=1} = P_1/(R_{AIR}T_1) \tag{27}$$

and,

$$(\rho u)_{I=1} = \rho_1 u_1 \tag{28}$$

$$(\rho e)_{I=1} = \rho_1[c_v T_1 + \tfrac{1}{2}(u_1)^2] \tag{29}$$

At the downstream outflow boundary, $I = IMAX$, the pressure is specified to be the free stream value while the normal gradients of the velocities and total energy are set to zero which implies that the values of these variables are extrapolated from the interior of the flow field:

$$P_{IMAX} = P_\infty \tag{30}$$

$$u_{IMAX} = u_{IMAX-1} \tag{31}$$

$$v_{IMAX} = v_{IMAX-1} \tag{32}$$

$$e_{IMAX} = e_{IMAX-1} \tag{33}$$

The conditions on the velocities and the total energy at the outflow imply a specification of the temperature at the outflow which in turn implies a boundary condition on the density at the outflow via the ideal gas law:

13

$$\rho_{IMAX} = P_{IMAX} / (R_{AIR} \cdot T_{IMAX}) \tag{34}$$

and,

$$(\rho u)_{IMAX} = \rho_{IMAX} u_{IMAX} \tag{35}$$

$$(\rho v)_{IMAX} = \rho_{IMAX} v_{IMAX} \tag{36}$$

$$(\rho e)_{IMAX} = \rho_{IMAX} e_{IMAX} \tag{37}$$

D. Initial Conditions

In the current simulation, no attempt was made to produce a time accurate solution of the initial transient of the developing flow. Therefore, the initial conditions were used only as a starting point from which the algorithm could begin calculation of a steady state solution.

To this end, at the beginning of the calculation, it was assumed that a turbulent boundary layer, two rib heights in thickness, δ, existed throughout the rectangular channel. Within this boundary layer, the horizontal velocity was given by the 1/7 power law:

$$u(y) = u_\infty (y/\delta)^{1/7} \tag{38}$$

Above the boundary layer, the horizontal velocity was set equal to the free stream velocity, Equation (14).

Throughout the flow field, the vertical component of velocity was set to zero; while the pressure, temperature and density were set equal to the free stream values, Equations (15) − (17). The initial conditions on the momentum and total energy were then calculated using the initial values of these primitive variables. Finally, the density and energy at the solid boundary were modified to account for the higher temperature of the wall.

E. Numerical Algorithm

The current mathematical model of the cooling air flow through a rectangular passage with a turbulence promoter is composed of the computational domain, the set of governing equations, the boundary conditions, and the initial conditions. The numerical algorithm used to calculate the solution to this model is the MacCormack explicit predictor-corrector technique as implemented by Shang and Hankey [14].

Although this computer code can be utilized to achieve a time accurate transient solution, it also contains an option which allows accelerated convergence to a steady state solution through the use of local time stepping. This local time stepping option was invoked in the current simulation to produce the steady state solution described in the following section.

SECTION III

RESULTS

A. Convergence

In Shang's implementation of the MacCormack algorithm, various options exist to accelerate convergence and/or maintain numerical stability. The algorithm can be run in the local time step mode to accelerate convergence or the time accurate mode to maintain stability. The algorithm contains a numerical smoothing, which when invoked promotes stability, but can also degrade the solution. Finally, the turbulent viscosity can be omitted from the iteration which promotes stability but also produces a less realistic solution. Therefore, a strategy must be developed for the use of these various options so as to achieve a stable but realistic solution while minimizing the number of iterations required. For example, the iteration could be initiated with all options turned to full stability. Then, after a number of iterations, options could be switched to maximize the rate of convergence. Finally, a number of iterations should be run with the options switched to produce the most realistic solution. The strategy used in the current simulation is shown in Table 1.

In Shang's implementation, convergence is measured by the L-2 norm of the change in the normalized global solution vector between successive iterations, $\left\| \delta \vec{U}_{n+1} \right\|$. The global solution vector, $\vec{U}$, is the concatenation of all of the nodal solution vectors as given in Equation (7). Each component of the change in the global solution vector is

16

Table 1. Iteration Strategy

Iteration Count	Time Step	Smoothing	Turbulent Viscosity
0– 5,000	Time Accurate	On	Off
5,001–10,000	Local Time Step	On	Off
10,001–45,000	Local Time Step	On	On
45,001–99,999	Time Accurate	Off	On

Table 2. L-2 Norm of Increments of the Solution Vector

Iteration Count	$\left\lVert \delta \vec{U}_{n+1} \right\rVert$
0	0.7137 E+1
5,000	0.8197 E-2
10,000	0.7993 E-2
15,000	0.3739 E-2
45,000	0.3735 E-2
50,000	0.2662 E-2
55,000	0.2415 E-2
65,000	0.2560 E-2
75,000	0.2353 E-2
99,999	0.2414 E-2

squared, normalized by the free stream value of the respective variable, and summed:

$$\left|\left| \delta \vec{U}_{n+1} \right|\right| = \sum_i \sum_j \left[\left(\frac{\rho_{ij}^{n+1} - \rho_{ij}^{n}}{\rho_\infty}\right)^2 + \left(\frac{(\rho u)_{ij}^{n+1} - (\rho u)_{ij}^{n}}{(\rho u)_\infty}\right)^2 \right.$$

$$\left. + \left(\frac{(\rho v)_{ij}^{n+1} - (\rho v)_{ij}^{n}}{(\rho u)_\infty}\right)^2 + \left(\frac{(\rho e)_{ij}^{n+1} - (\rho e)_{ij}^{n}}{(\rho e)_\infty}\right)^2 \right] \tag{39}$$

Typically, in the iteration to a converged steady state solution, the value of this norm will drop 3 orders of magnitude from the initial conditions and then oscillate about this reduced value, indicating that convergence has been achieved [13]. As shown in Table 2 for the current simulation, the value of this norm decreased from 7.137 at the outset to 0.002662 after 50,000 iterations and oscillated near that value for the remaining 49,999 iterations. This behavior is typical of convergence to the steady state solution. The current simulation required 92 minutes of execution time on a Cray-1 computer.

B. Velocity and Temperature Profiles

As described in Section II.A., the computational grid is 20 rib heights in length with the top front corner of the rib located 5 rib heights downstream from the inflow boundary, and the top back corner of the rib located 6 rib heights downstream from the inflow boundary. There are 100 grid lines in the streamwise X-direction, clustered around the rib. These grid lines are numbered as the K index starting at the inflow boundary. Hence, $K = 1$ corresponds to the inflow boundary.

Profiles of u/u_∞, v/v_∞, and T/T_∞ were plotted against Y/YMAX at the 16 streamwise locations listed in Table 3. In these profile plots, given in Figures 2 through 49, a rib height corresponds to Y/YMAX = 0.237. Hence, in the profile plots for K values of 28, 33, 38, and 47,

18

Table 3. Profile Locations

K (Streamwise Index)	Distance from Inflow Boundary Measured in Rib Heights
1	0
6	2
11	3
18 (Front bottom corner of rib)	4
28 (Front top corner of rib)	5
33 (Rib centerline)	5.5
38 (Back top corner of rib)	6
47 (Back bottom corner of rib)	7
57	8
67	9
75	10
80	11
83	12
85	13
89	15
100	20

the curve does not reach Y/YMAX = 0 because the bottom of the computational mesh coincides with the top of the rib or turbulence promoter which has a Y/YMAX value greater than zero.

The profiles at K = 1 represent the inflow boundary conditions where the flow has not yet properly developed. This explains the uniformly zero vertical velocity and the fluctuating horizontal velocity.

At K = 6, the profiles show that the momentum and thermal boundary layers are beginning to develop. Since this flow is predominately in the horizontal direction, the vertical velocity is very small compared to the horizontal velocity. Therefore, the small variations, which are due to round off in the calculation of the vertical velocity, are nearly the same magnitude as the actual vertical velocity, thus producing the exaggerated fluctuation exhibited in the vertical velocity profile.

At K = 11, and 18, the profiles show the continued development of the momentum and thermal boundary layers and a vertical acceleration as the flow begins to move up and over the turbulence promoter. Also at K = 18, both the vertical and horizontal velocities are negative near the solid wall which indicates the presence of a recirculation zone which will be discussed later.

The locations, K = 28. 33, and 38, are at the front top corner, midline and back top corner of the rib, respectively. The vertical velocity is positive, indicating that the flow is moving up over the rib. The horizontal velocity is greatly accelerated near the solid wall, exhibiting a uniform profile at K = 38, typical of a fully developed turbulent flow. Both the momentum and thermal boundary layers have been destroyed due to the intense turbulent mixing which is

occurring. The temperature near the wall is much lower than at previous

streamwise locations and exhibits some numerical overshoot. This

overshoot as well as the fluctuations in both temperature and horizontal

velocity profiles are numerical artifacts produced by over restrictive

boundary conditions at the top boundary which will be corrected in

future calculations.

The streamwise locations, K = 47 through K = 83, start at the back

bottom corner of the rib and extend to the reattachment point which

marks the end of the large recirculation bubble downwind of the rib.

The temperature profiles show that the turbulent mixing behind the rib

has greatly diffused the energy from the hot solid wall to form a warm

air region which extends almost 2 rib heights vertically from the solid

wall. The horizontal velocity profile is typical of a recirculation

zone with a negative upstream flow near the wall changing to a positive

downstream flow higher in the flow field. The vertical velocity

profiles also show evidence of flow recirculation.

The profiles at K = 85, 89, and 100, demonstrate that both the

momentum and thermal boundary layers are reestablished downstream of the

recirculation bubble. However, comparison of these profiles to those at

K = 6, 11, and 18, upstream of the turbulence promoter, show that the

downstream boundary layers are much thicker and well mixed, illustrating

the effects of the intense turbulent mixing caused by the flow over the

turbulence promoter.

C. Streamlines, Skin Friction, and Heat Transfer Rates

Careful analysis of the printed output at each of the 100 streamwise locations reveals the interesting details of the flow pattern shown in Figure 50. There are five recirculation zones or bubbles produced by the flow over the turbulence promoter. There is a clockwise rotating zone, 1.0 rib height in length, which begins 1.0 rib height upstream of the rib and is approximately 0.1 rib height tall. The second clockwise rotating bubble, which is about a half rib height in length and very thin, begins just downstream from the top front corner of the rib. Behind the rib there are two counterclockwise vortices which are separated by a clockwise vortex. The first clockwise vortex, which is 1.0 rib height in length, begins just behind the back top corner and is 0.54 rib height in thickness. Adjacent to this clockwise vortex is a counterclockwise vortex of approximately the same size. Finally, there is the very large recirculation bubble which begins just downstream of the back top corner of the rib and attains a maximum thickness of 0.71 rib height just behind the rib. This large bubble extends to the reattachment point which is located approximately 7.0 rib heights from the back top corner or 6.0 rib heights from the back bottom corner.

The location of the reattachment point agrees very well with the wind tunnel investigations of flow over a surface mounted cube conducted by Castro and Robins [2]. They report that the wake produced by a uniform turbulent stream completely decayed within 6.0 cube heights downstream.

Skin friction and heat transfer rates were calculated at the 16 streamwise locations listed in Table 3. The values of local skin friction, shown in Table 4 and plotted in Figure 51, were calculated from the following equation:

$$c'_f = \frac{\tau_{wall}}{\frac{1}{2}\rho_\infty u_\infty^2} = \frac{\mu(\frac{\partial u}{\partial y})_{y=0}}{\frac{1}{2}\rho_\infty u_\infty^2} \tag{40}$$

The normal derivative of the horizontal velocity was approximated as a central difference between the $J = 1$ node (solid wall) and the $J = 2$ node ($Y \leq 0.3281$ E-4 feet). The viscosity was determined by averaging the values given by Sutherland's Law evaluated at $T_{J=1}$ and $T_{J=2}$.

Table 4. Local Skin Friction Coefficient

K (Streamwise Index)	Skin Friction Coefficient (c_f' x 10^4)
1	0
6	62.28
11	7.43
18	47.62
28	77.39
33	34.11
38	12.23
47	1.34
57	15.50
67	42.67
75	52.06
80	47.80
83	55.38
85	2.24
89	20.44
100	35.57

The local heat transfer rates, given in Table 5 and plotted in Figure 52, are expressed in terms of the nondimensional Stanton number:

$$St = \frac{Q_{wall}}{c_p \rho_\infty u_\infty (T_{wall} - T_\infty)} \tag{41}$$

These heat transfer rates were calculated by two different methods. In the first method, the Reynolds Analogy was used, in which the heat transfer rate is related to the skin friction as follows:

$$\text{Stanton Number} = \tfrac{1}{2} c_f' \tag{42}$$

This method is widely used in turbomachinery calculations but these calculations greatly underpredict the heat transfer rates measured experimentally.

In the second method, Fourier's Conduction Law was used to evaluate the heat transfer rate at the wall, Q_{wall}, which appears in Equation (41):

$$Q_{wall} = -K \left(\frac{\partial T}{\partial y} \right)_{y=0} \tag{43}$$

In this calculation, the thermal conductivity was treated as a constant and the normal derivative of temperature was evaluated in a manner similar to that used for the normal derivative of the horizontal velocity discussed above.

In the convection heat transfer process, the energy is first transferred by conduction from the solid wall to the fluid particles adjacent to the wall. These fluid particles are then transported away from the solid wall by the bulk mixing of the fluid which results in the diffusion of energy from the solid wall. The basis for the Reynolds Analogy is the assumption that the same mechanism is responsible for the exchange of both heat and momentum. This assumption disregards the details of the energy transfer process at the solid wall-fluid

25

Table 5. Local Heat Transfer Rates

| K | Stanton Number x 10^3 | |
(Streamwise Index)	via Reynolds Analogy	via Fourier's Law
1	0.0	24.33
6	3.11	4.38
11	0.37	1.20
18	2.38	4.03
28	3.87	3.62
33	1.71	3.71
38	0.61	3.15
47	0.07	1.54
57	0.78	1.48
67	2.13	2.33
75	2.60	2.83
80	2.39	3.11
83	2.77	4.24
85	0.11	3.39
89	1.02	3.11
100	1.78	2.90

interface. As shown in Table 5 and Figure 52, the direct calculation of the heat transfer rate via Fourier's Law predicts heat transfer rates which can be as great as 30 times that given by the Reynolds Analogy. This great discrepancy can be explained by the fact that the Reynolds Analogy is derived for laminar or fully turbulent flows over a flat plate with laminar and turbulent Prandtl number, $Pr = Pr_t = 1.0$. Thus, the Reynolds Analogy is not applicable to flows with recirculation zones and flow reversals which cause the normal gradient of velocity to differ greatly from the normal gradient of temperature.

SECTION IV

CONCLUSIONS

The flow field and heat transfer along a turbine blade internal cooling passage was numerically simulated using a two dimensional geometry. Attention was focused on the flow along a short straight section of a rectangular passage with a single transverse mounted turbulator protruding from its floor. The two dimensional, transient, Reynolds averaged Navier Stokes, continuity and energy equations were iterated to a steady state solution using the second order accurate MacCormack explicit predictor-corrector algorithm. Turbulence closure was achieved through the use of the Baldwin-Lomax form of the Cebeci-Smith algebraic two layer eddy viscosity model.

In contrast to the work done by earlier investigators, this study was performed using a computational mesh which had very high resolution. There were 100 grid lines in the horizontal (axial) direction clustered around the turbulator and 60 grid lines in the vertical direction with 44 within the first rib height which was well within the turbulent boundary layer. This high resolution mesh revealed considerable detail of the flow field and heat transfer near the turbulator.

The calculation revealed a complex flow structure near the turbulator with five stationary or standing vortices. This flow structure, which is more complex than is ordinarily expected for such a simple passage/turbulator geometry, has a pronounced effect upon the heat transfer as shown in Table 5 and Figure 52. This significant insight indicates that further study is needed into the effects of turbulator geometry and spacing (or pitch) as a means of heat transfer enhancement.

Furthermore, this calculation revealed a considerable difference between the heat transfer rate calculated by using the Reynolds Analogy and that given by a direct calculation using Fourier's law. This discrepancy results from the complex flow structure near the turbulator which causes the normal gradient of velocity to differ greatly from the normal gradient of temperature. Similar flow structures exist throughout many turbomachinery components, and therefore, corresponding heat transfer effects may occur in those components which would also be inadequately predicted by the Reynolds Analogy. This significant insight may lead to remedies for the underprediction of heat transfer rates in many turbomachinery calculations.

REFERENCES

1. Baldwin, B. and Lomax, H., 1978, "Thin Layer Approximation and Algebraic Model for Separated Turbulent Flows," AIAA-78-257, AIAA 16th Aerospace Sciences Meeting, Huntsville, Alabama.

2. Castro, I. P. and Robins, A. G., 1977, "The Flow Around a Surface-Mounted Cube in Uniform and Turbulent Streams," Journal of Fluid Mechanics, Vol. 79, pp. 307-335.

3. Durst, F. and Rastogi, A. K., 1979, "Theoretical and Experimental Investigations of Turbulent Flows with Separation," Turbulent Shear Flows I, F. Durst et al., ed., Springer-Verlag, Berlin, pp. 208-219.

4. Fujita, H., Yokosawa, H., and Nagata, C., 1986 "The Numerical Prediction of Fully Developed Turbulent Flow and Heat Transfer in a Square Duct with Two Roughened Facing Walls," Proceedings of the Eighth International Heat Transfer Conference, C. L. Tien et al., ed., Hemisphere Publishing Corp., Washington, DC, Vol. 3, pp. 919-924.

5. Gessner, F. B., 1973, "The Origin of Secondary Flow in Turbulent Flow Along a Corner," Journal of Fluid Mechanics, Vol. 58, pp. 1-25.

6. Gessner, F. B. and Jones, J. B., 1965, "On Some Aspects of Fully Developed Turbulent Flow in Rectangular Channels," Journal of Fluid Mechanics, Vol. 23, pp. 689-713.

7. Han, J. C., 1984, "Heat Transfer and Friction in Channels with Two Opposite Rib-Roughened Walls," Transactions of the ASME, Journal of Heat Transfer, Vol. 106, pp. 774-781.

8. Han, J. C., Park, J. S., and Ibrahim, M. Y., 1986, "Measurement of Heat Transfer and Pressure Drop in Rectangular Channels with Turbulence Promoters," NASA Contractor Report 4015.

9. Han, J. C., Park, J. S., and Lei, C. K., 1985, "Heat Transfer Enhancement in Channels with Turbulence Promoters," Transactions of the ASME, Journal of Engineering for Gas Turbines and Power, Vol. 107, pp. 628-635.

10. Launder, B. E. and Ying, W. M., 1972, "Secondary Flows in Ducts of Square Cross Section," Journal of Fluid Mechanics, Vol. 54, pp. 289-295.

11. Linton, S. W. and Shang, J. S., 1987, "A Numerical Simulation of Jet Impingement Cooling in a Rotating Frame of Reference," AIAA-87-0609, AIAA 25th Aerospace Sciences Meeting, Reno, Nevada.

12. Melling, A. and Whitelaw, J. H., 1976, "Turbulent Flow in a Rectangular Duct," Journal of Fluid Mechanics, Vol. 78, pp. 289-315.

13. Rizzetta, D. P., 1987, Private communication, Flight Dynamics Laboratory, Wright Patterson AFB, Ohio.

14. Shang, J. S. and Hankey, Jr., W. L., 1975, "Numerical Solution for Supersonic Turbulent Flow over a Compression Ramp," AIAA-75-3, AIAA 13th Aerospace Sciences Meeting, Pasadena, California.

NOMENCLATURE

c_f' = skin friction

c_p = constant pressure specific heat of air

c_v = constant volume specific heat of air

D   = equivalent passage diameter

e   = total energy

$\vec{F}$ = flux vector

$\vec{G}$ = flux vector

H   = rib or turbulator height

I   = horizontal index

IMAX   = maximum horizontal index

J   = vertical index

JMAX   = maximum vertical index

P   = pitch, spacing between ribs or turbulators

P_i = flow field pressure

Pr   = molecular Prandtl number

Pr_t = turbulent Prandtl number

Q,q   = heat flux

St   = Stanton number

T   = air temperature

t   = time

$\vec{U}$ = solution vector

u   = horizontal velocity

X,x   = horizontal, axial coordinate

Y,y   = vertical coordinate

YMAX   = maximum vertical coordinate

Greek

α = rib or turbulator angle of attack

γ = ratio of specific heats

δ = turbulent boundary layer thickness

δ_{ij} = Kronecker delta

ε = turbulent eddy viscosity

η = transformed coordinate

μ = molecular viscosity of air

ξ = transformed coordinate

ρ = air density

τ = stress tensor

Subscript

o = total values

∞ = free stream value

wall = value at solid boundary
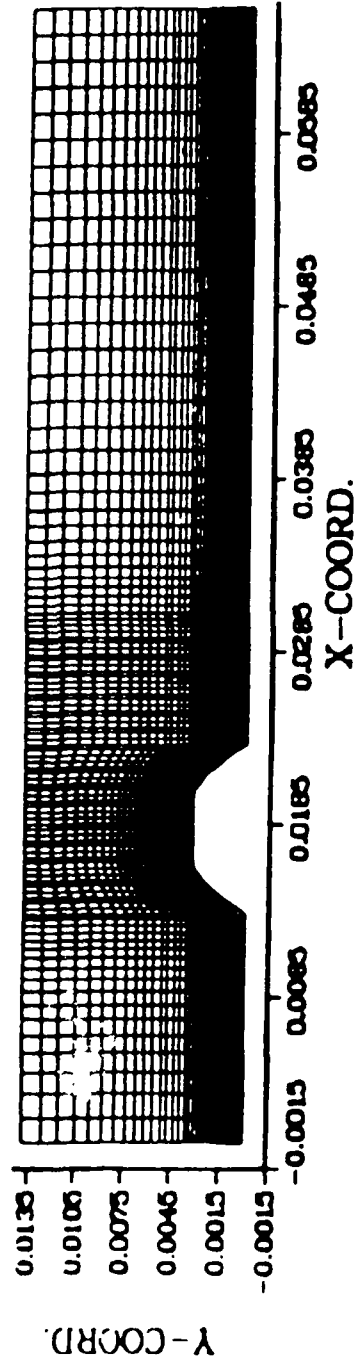
Figure 1. The 100 by 60, (X,Y), computational mesh used in this numerical study.
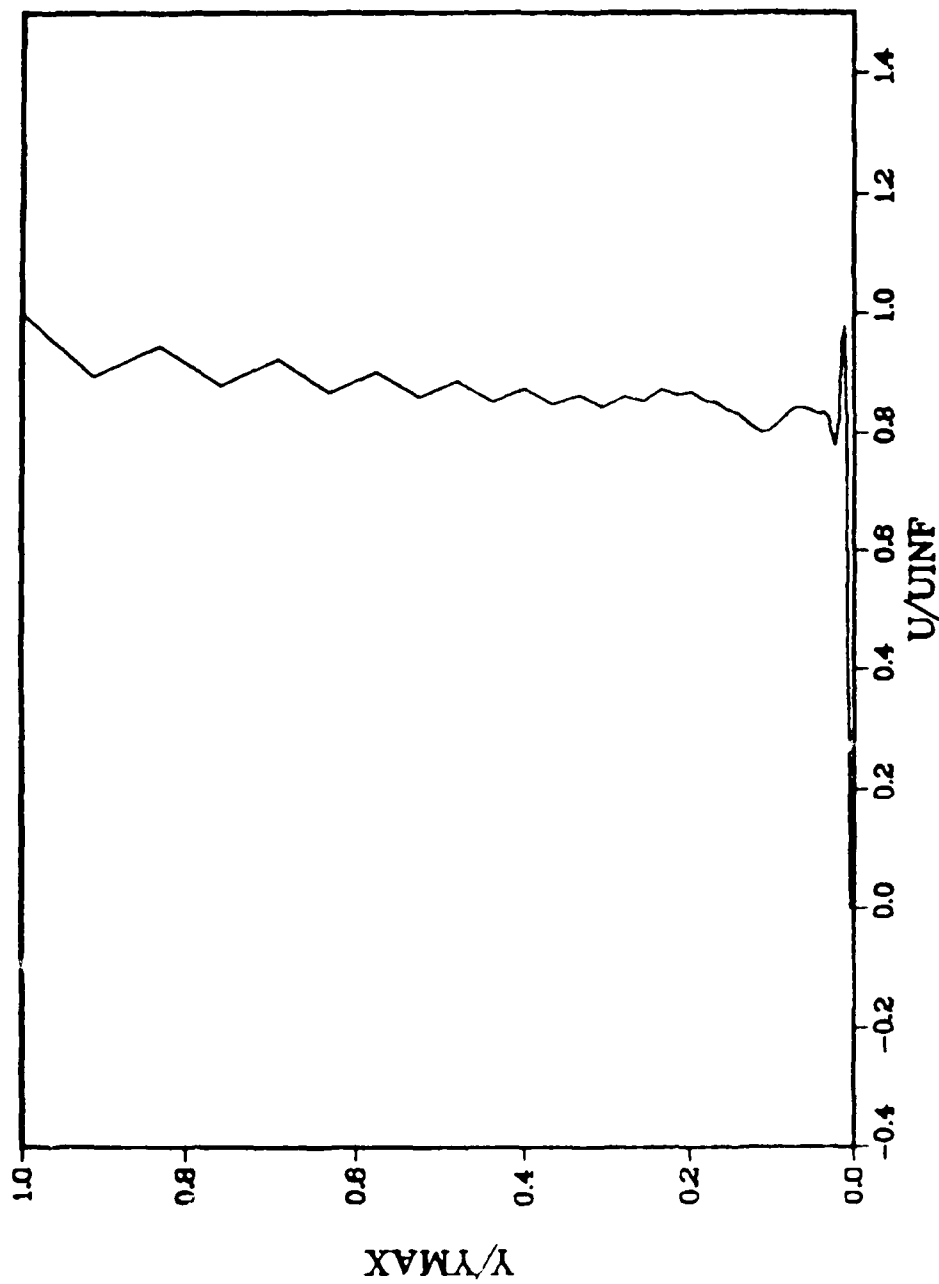
Figure 2. Horizontal velocity profile at K = 1.
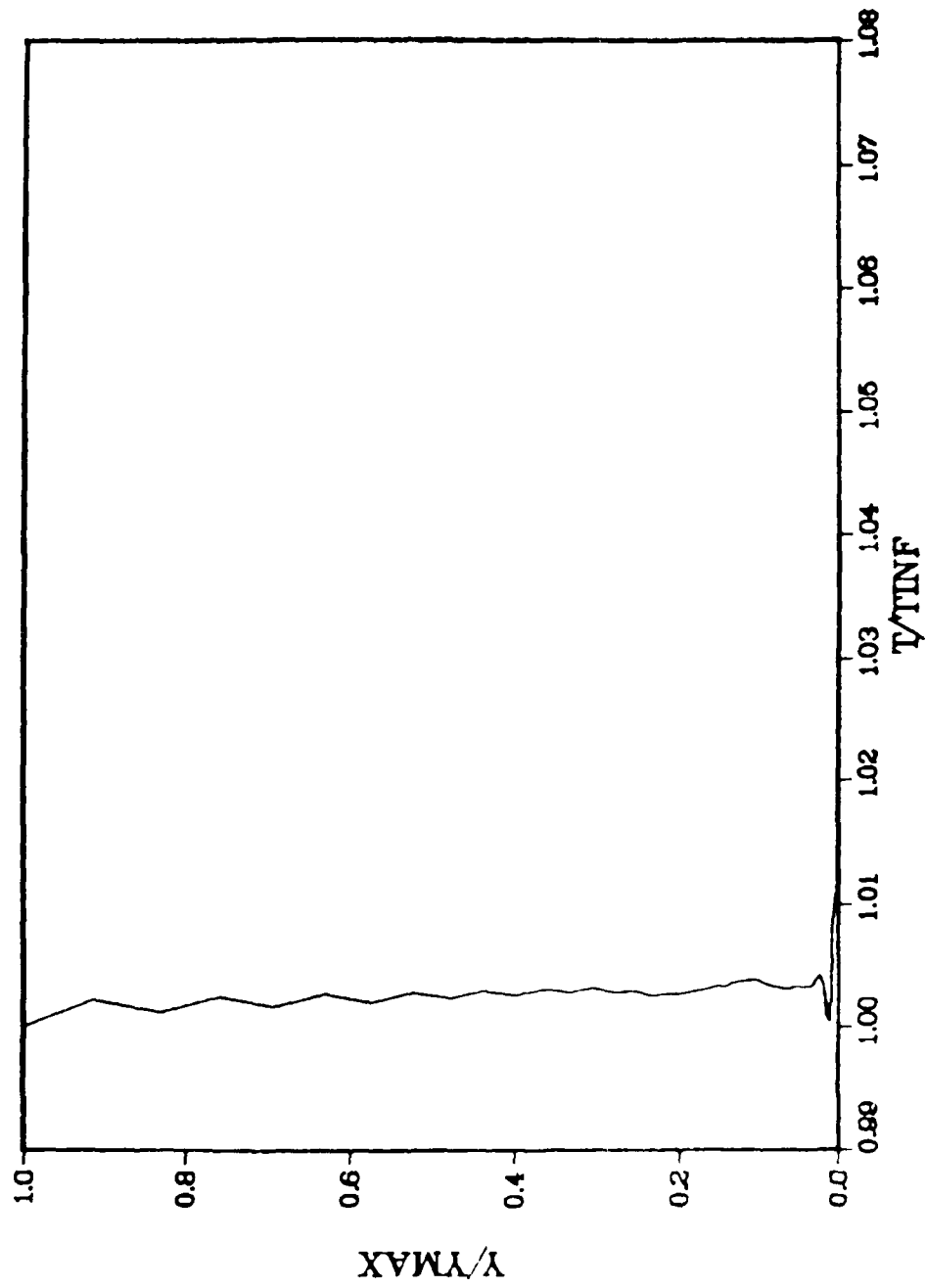
Figure 3. Temperature profile at K = 1.
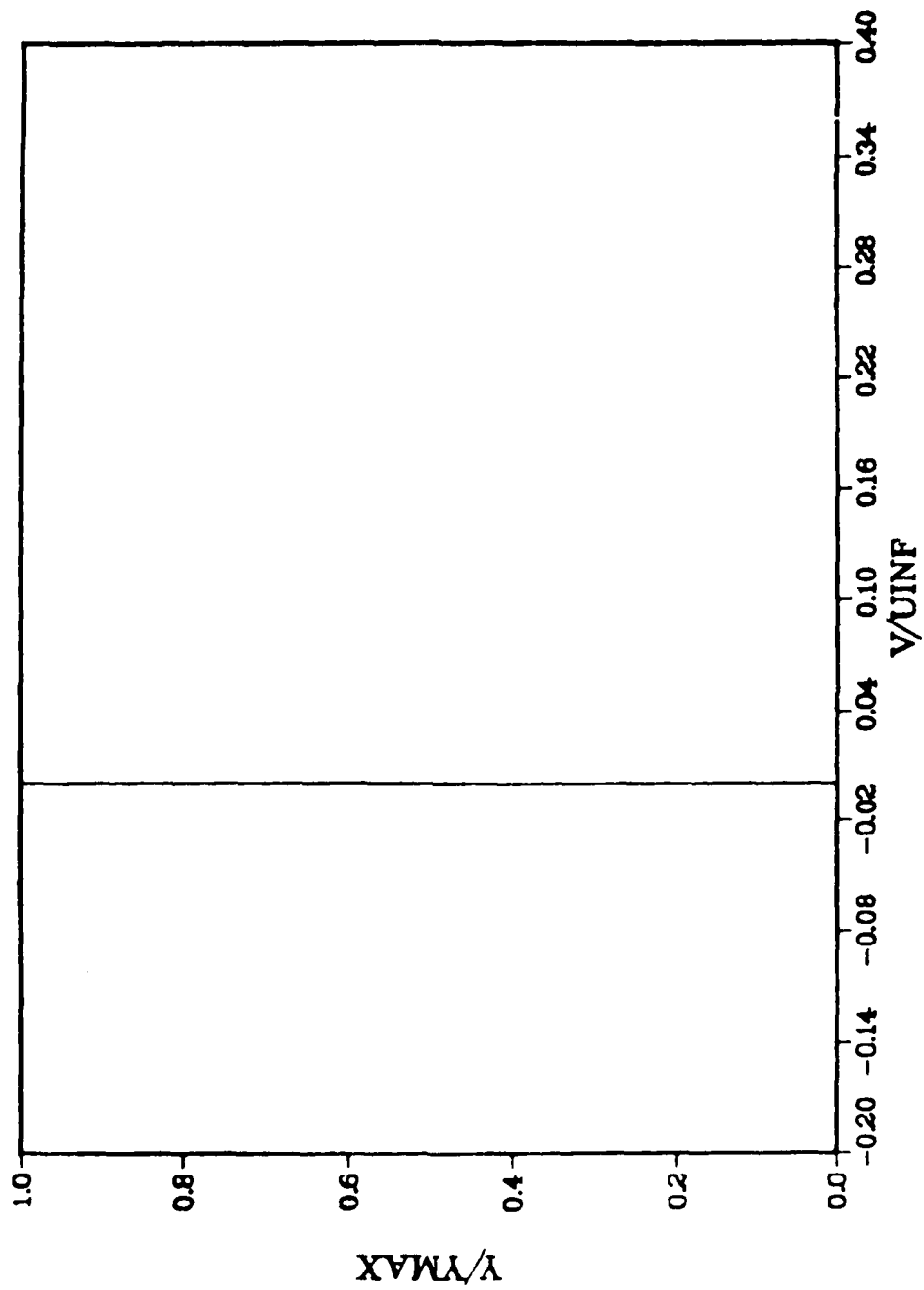
Figure 4. Vertical velocity profile at K = 1.

37
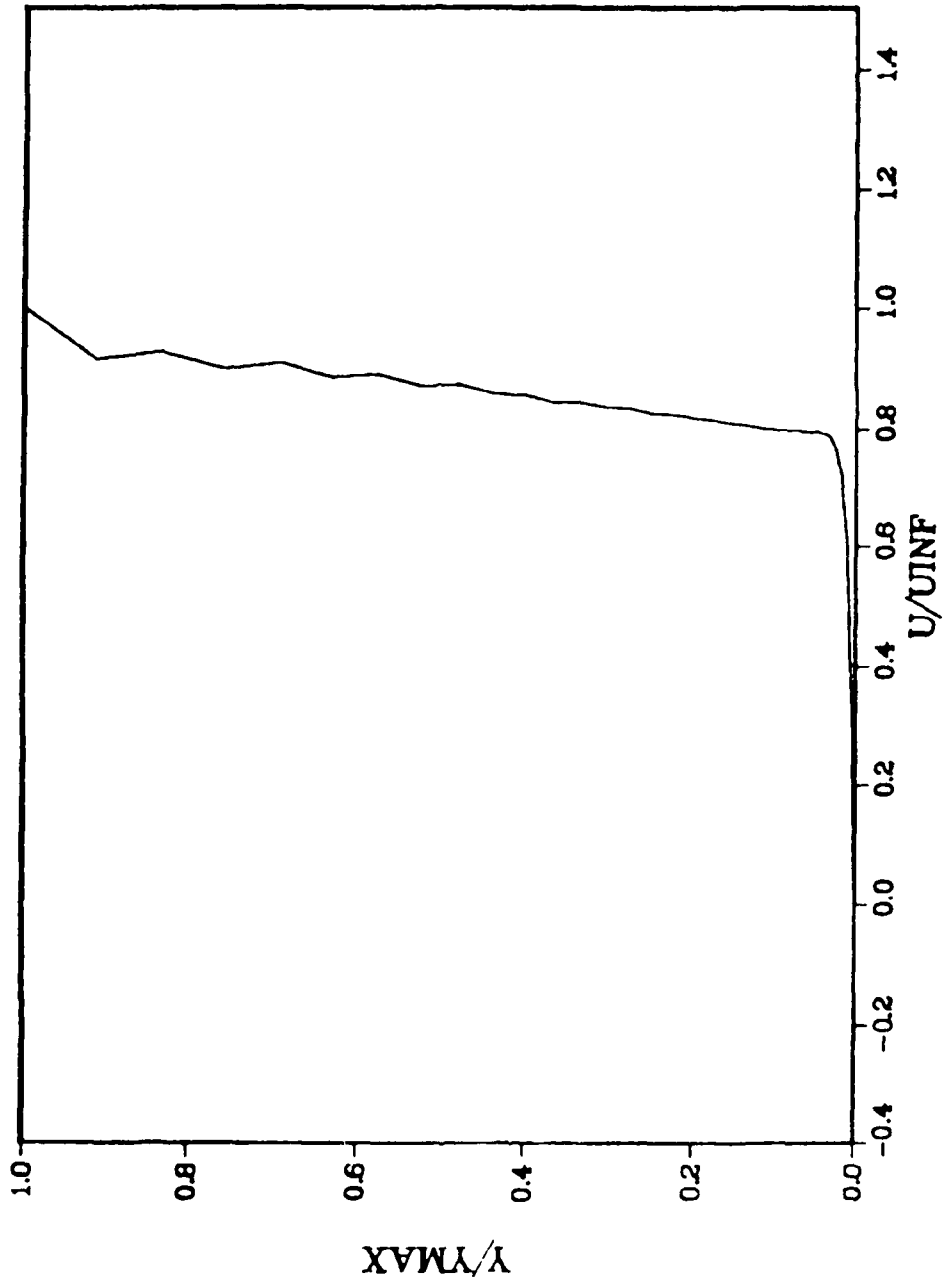
Figure 5. Horizontal velocity profile at K = 6.
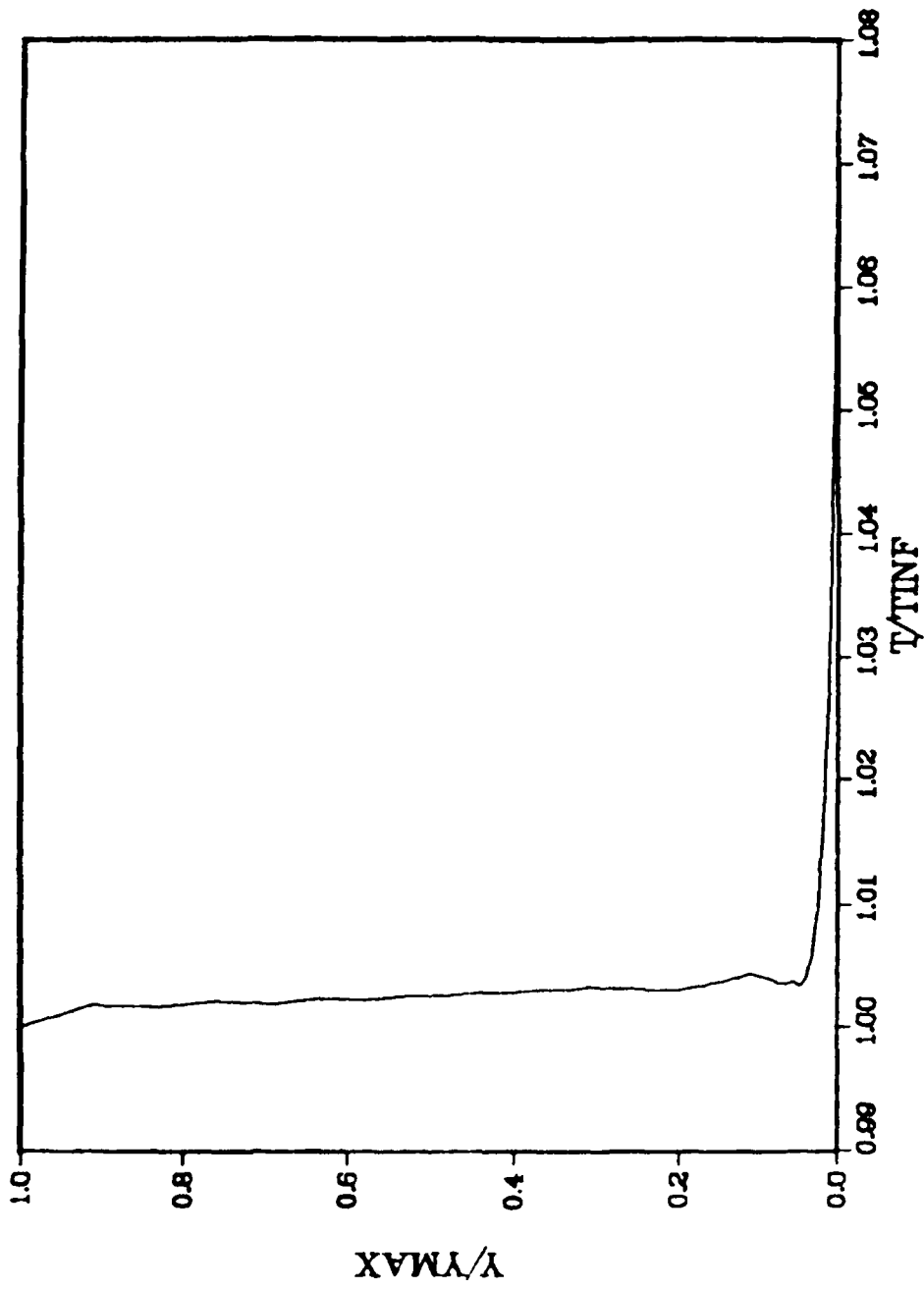
Figure 6.   Temperature profile at K = 6.

39
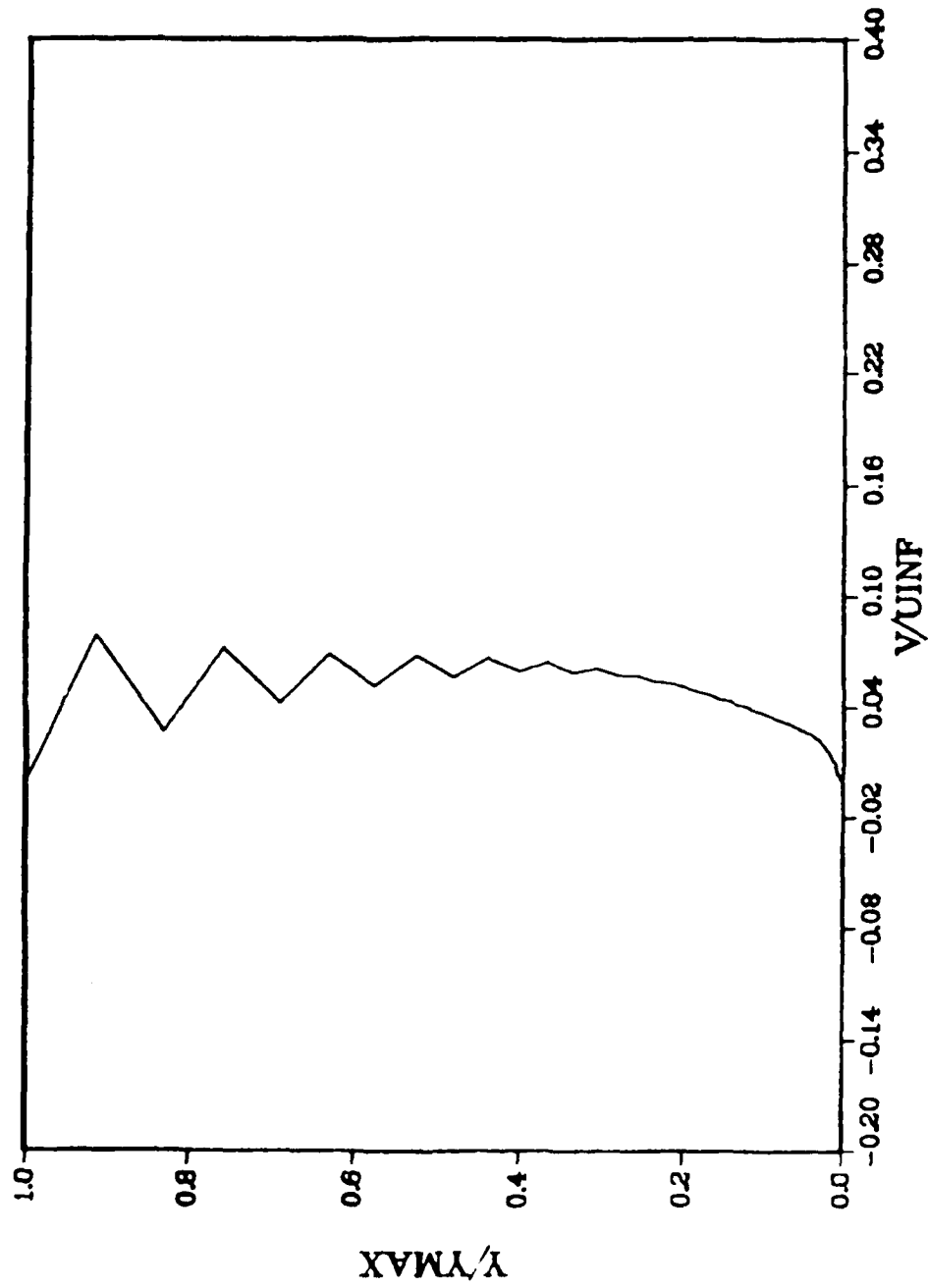
Figure 7. Vertical velocity profile at K = 6.
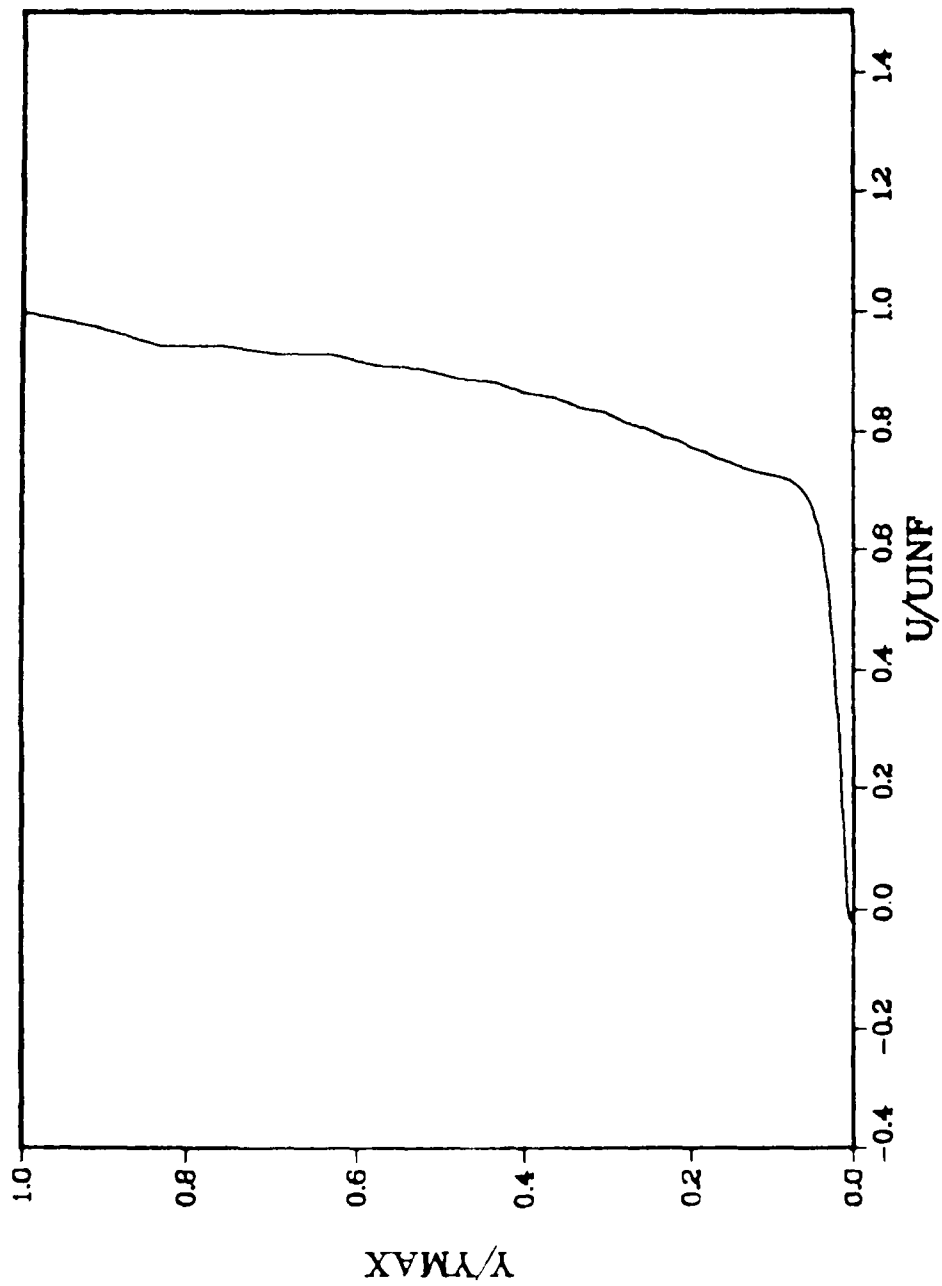
Figure 8. Horizontal velocity profile at K = 11.

41
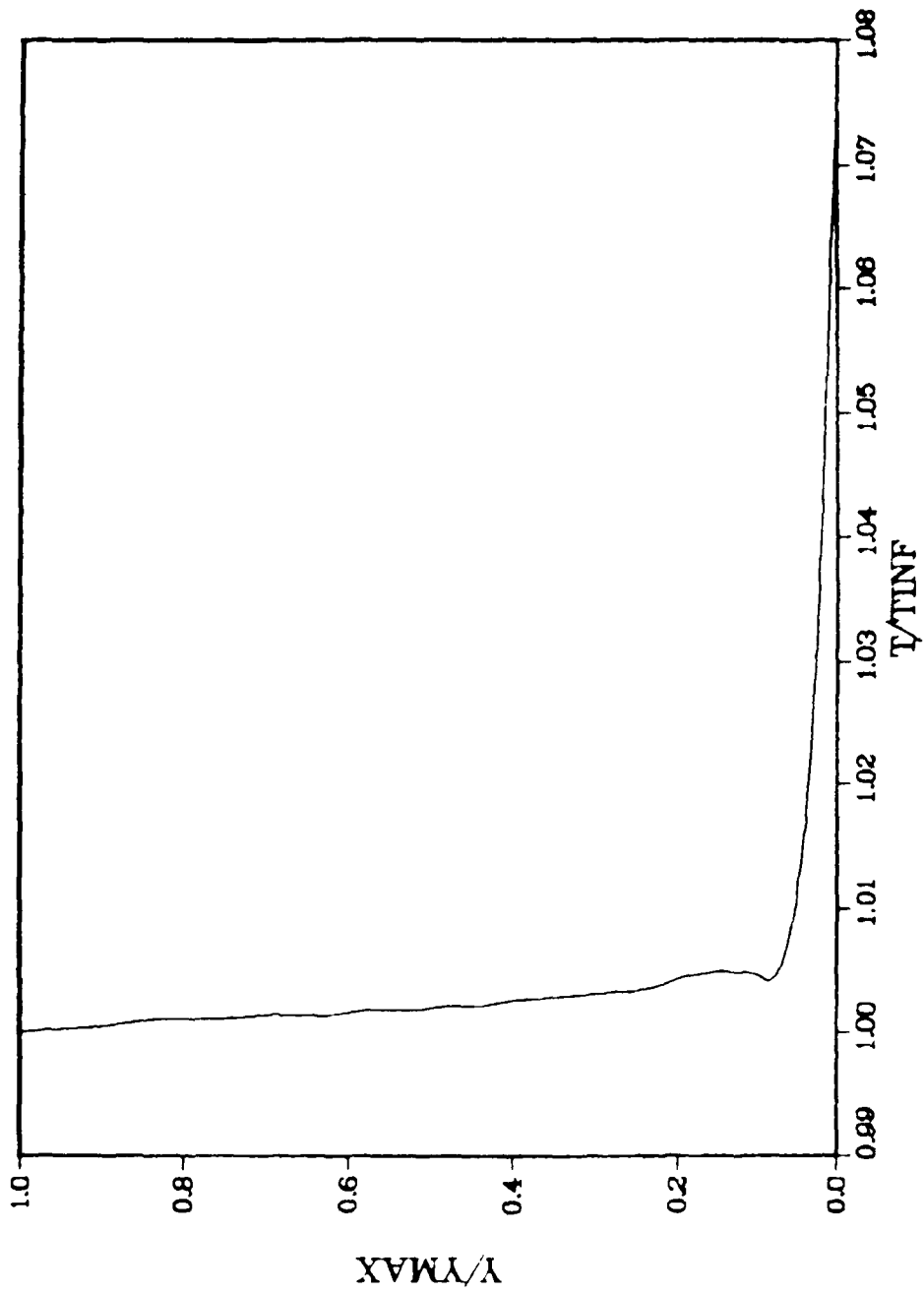
Figure 9. Temperature profile at K = 11.
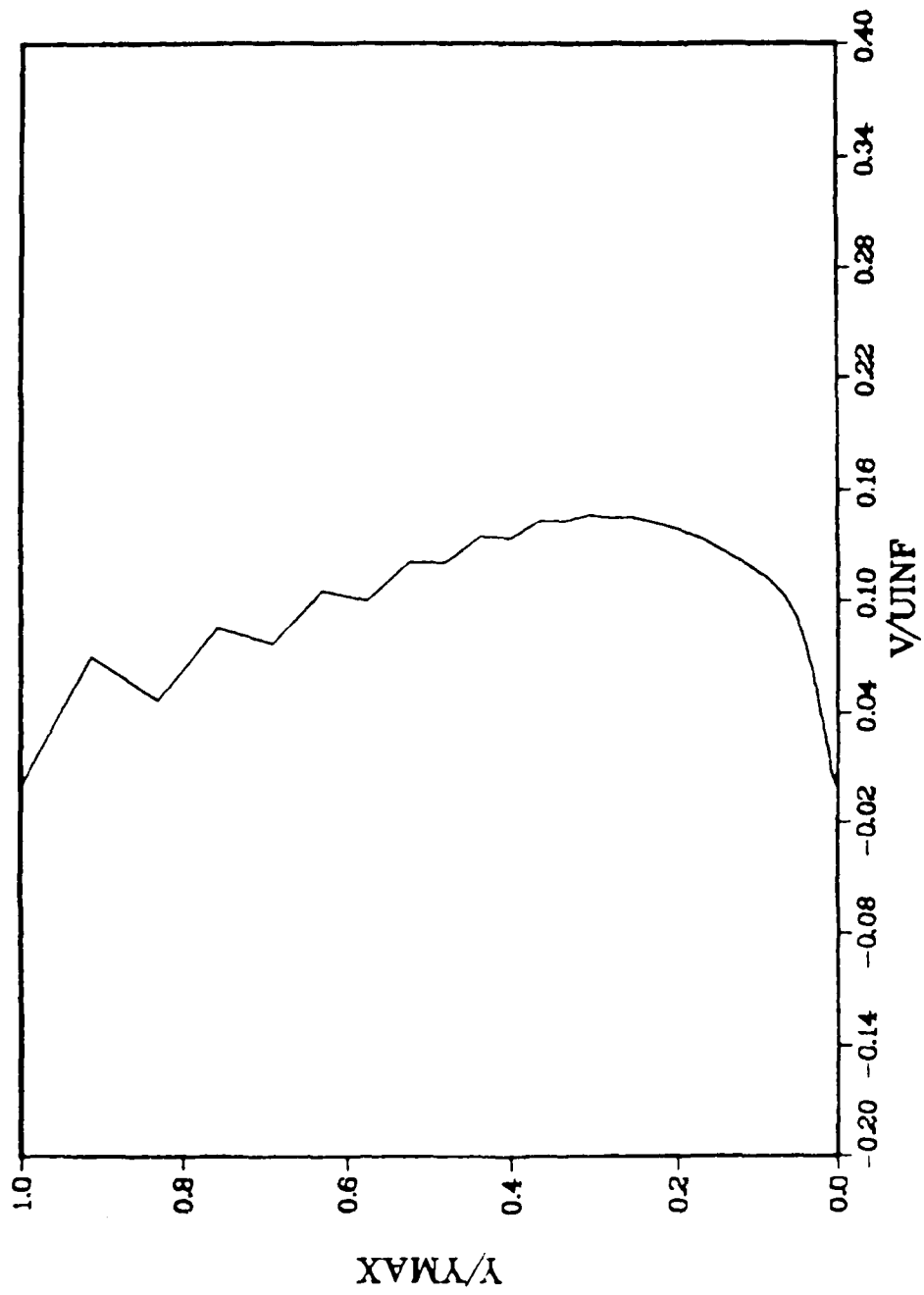
Figure 10. Vertical velocity profile at K = 11.
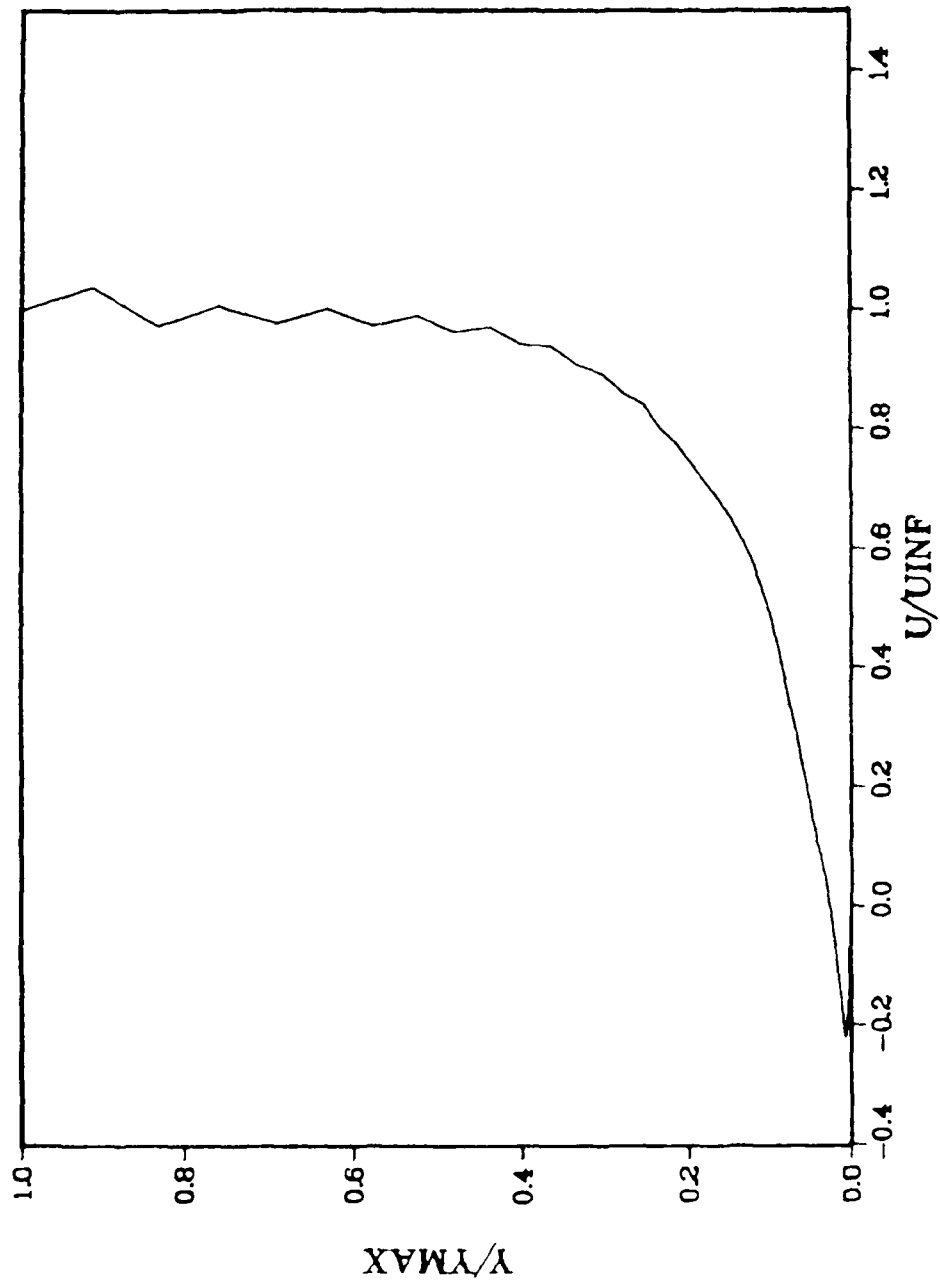
Figure 11. Horizontal velocity profile at K = 18.

49
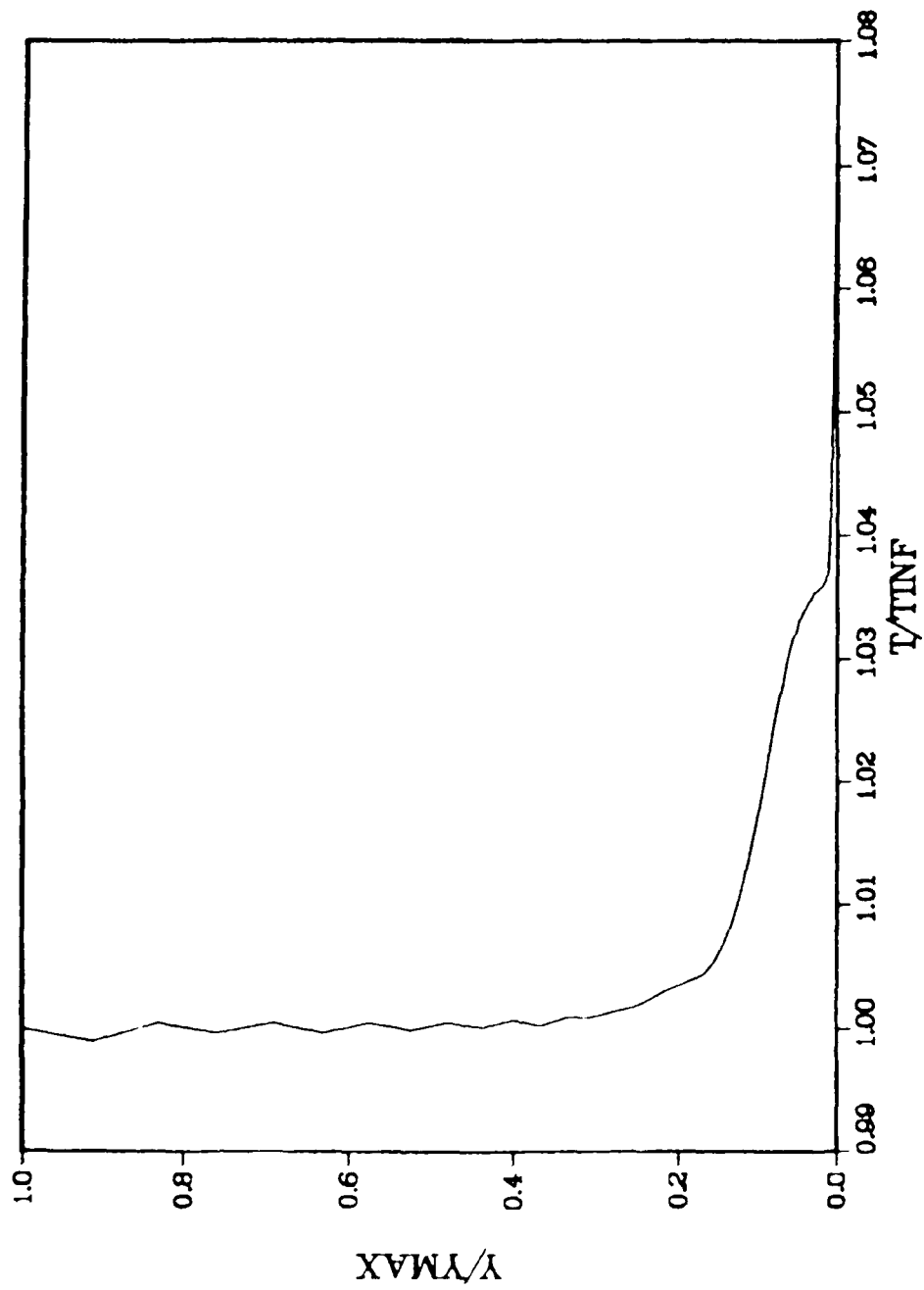
Figure 12. Temperature profile at K = 18.
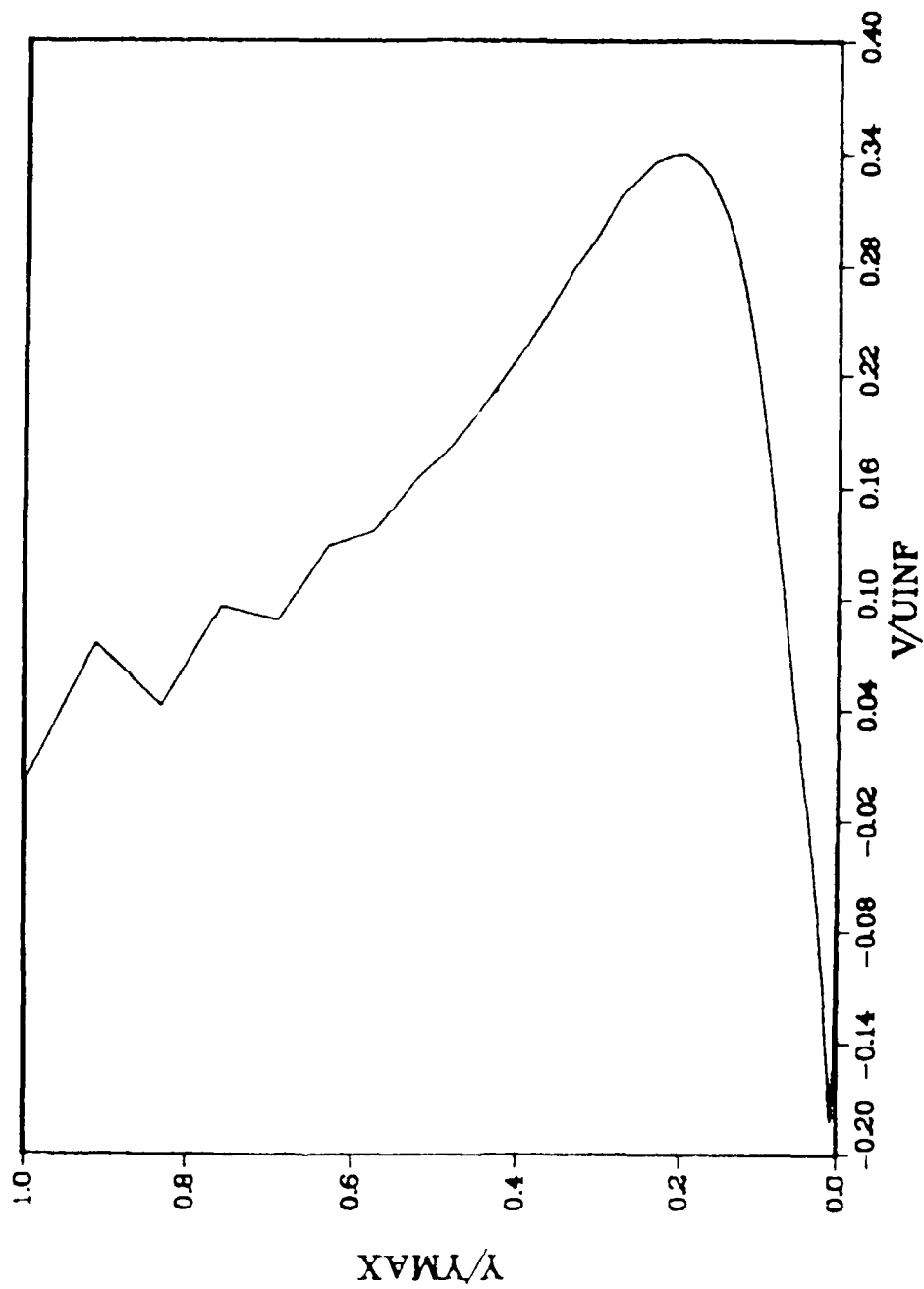
Figure 13. Vertical velocity profile at K = 18.
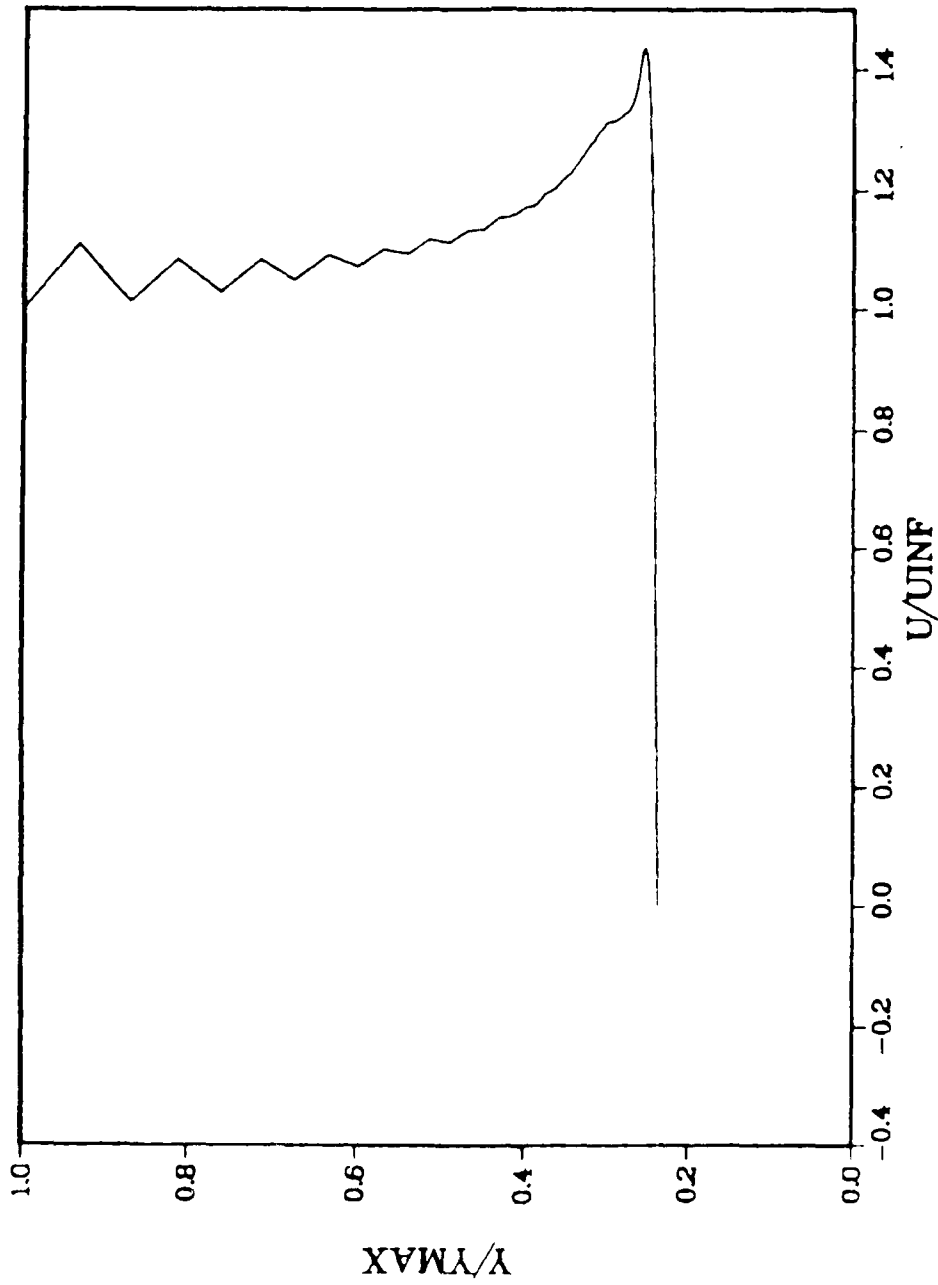
Figure 14. Horizontal velocity profile at K = 28.
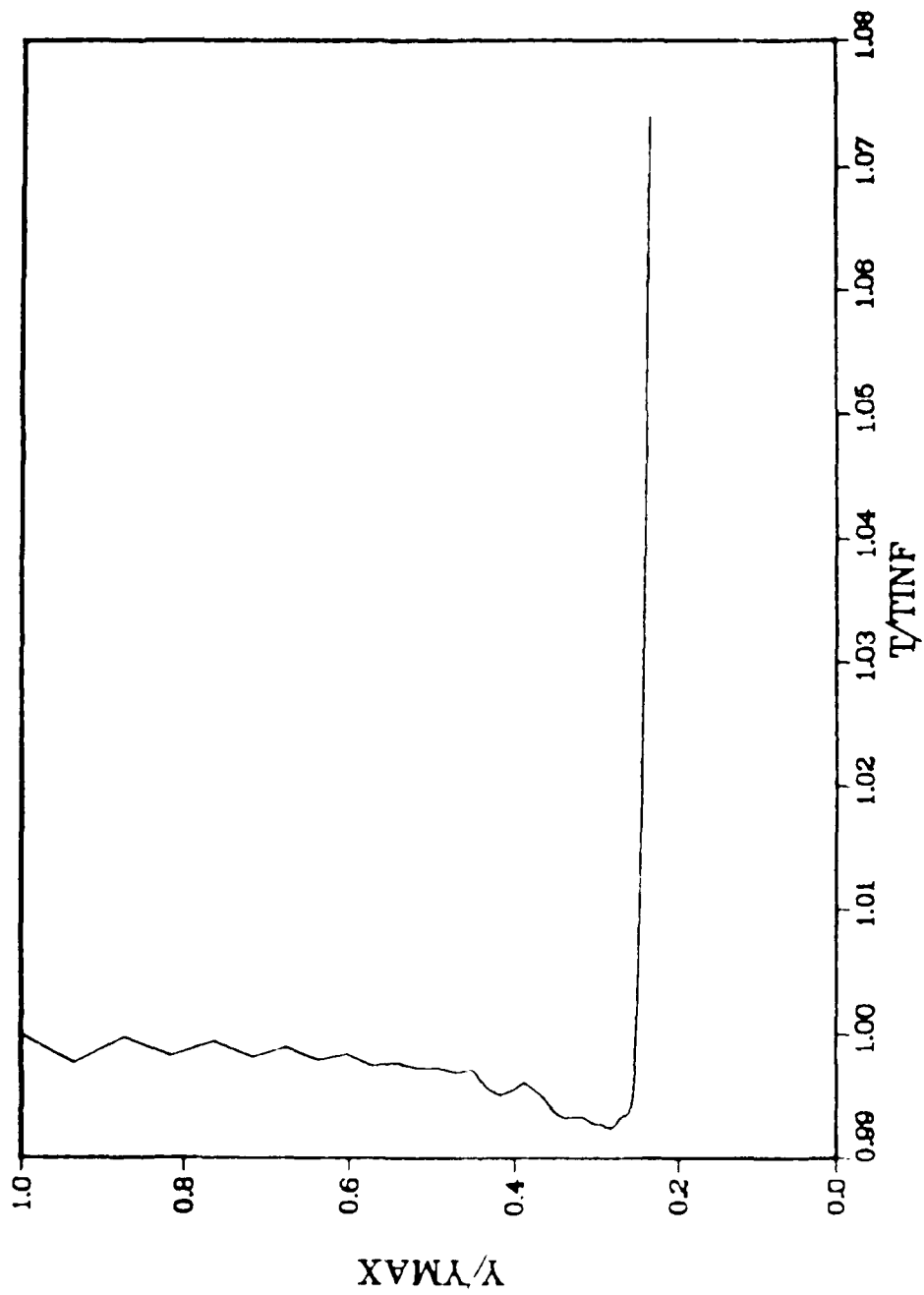
Figure 15. Temperature profile at K = 28.
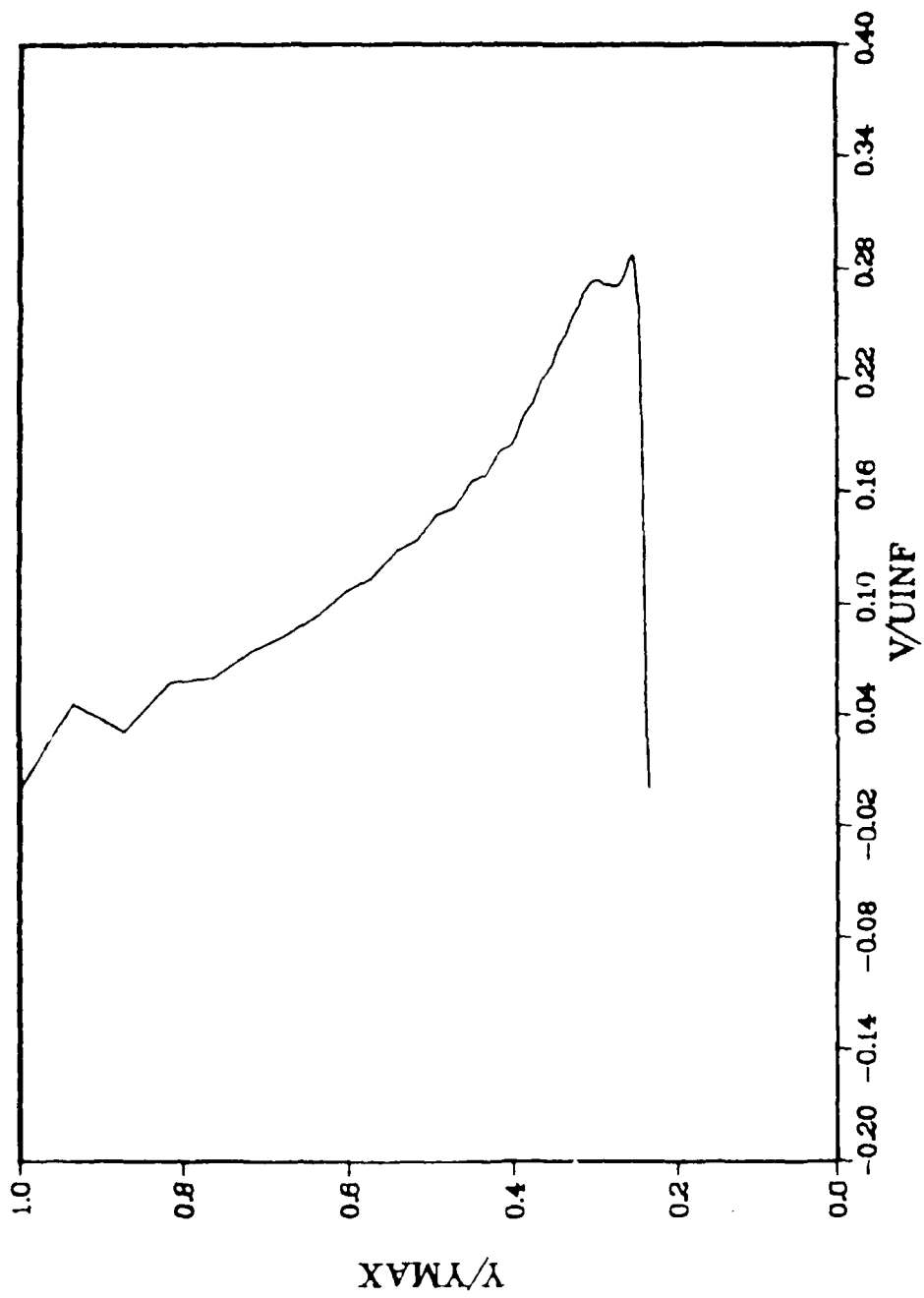
Figure 16. Vertical velocity profile at K = 28.

49
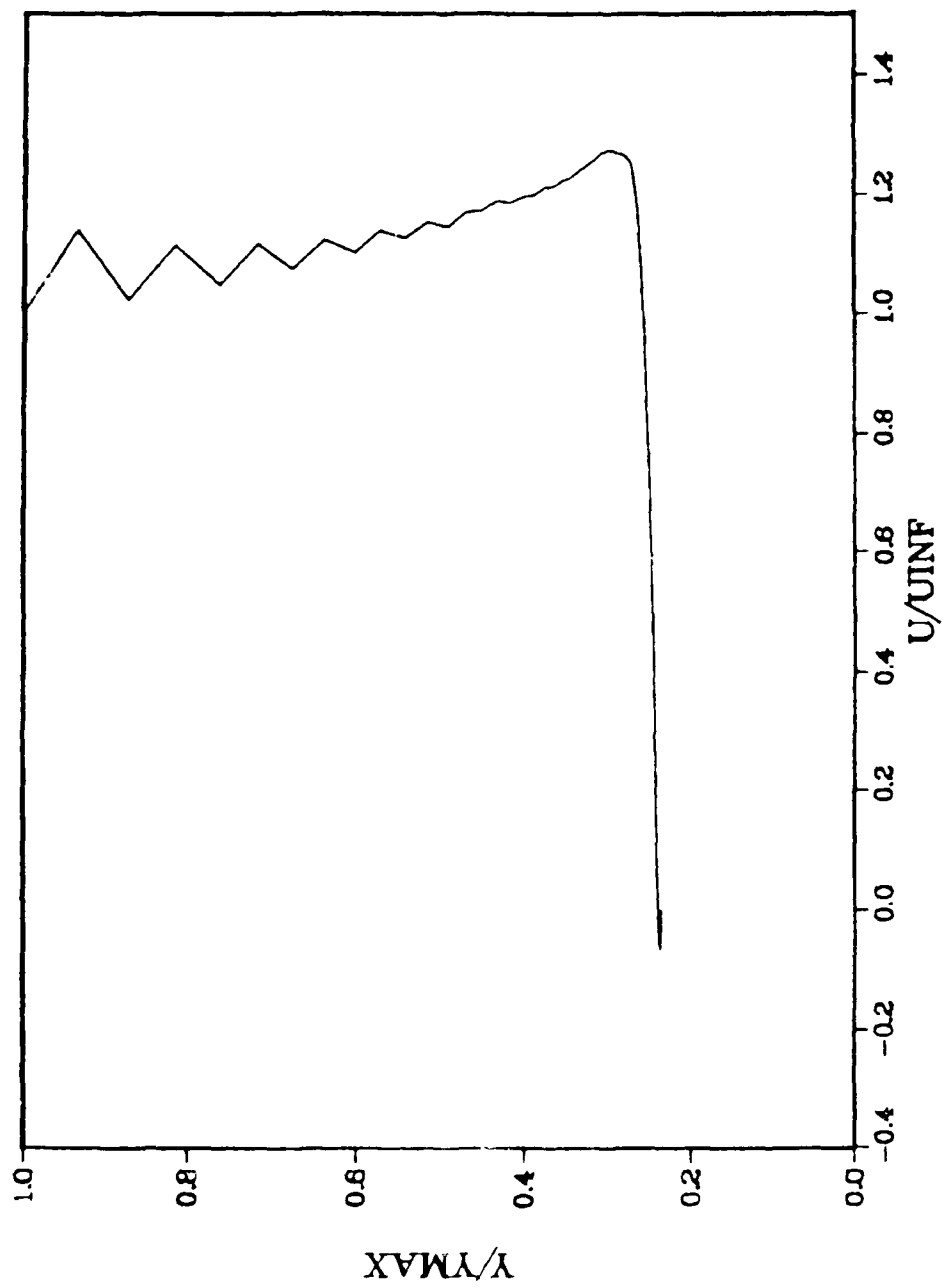
Figure 17. Horizontal velocity profile at K = 33.
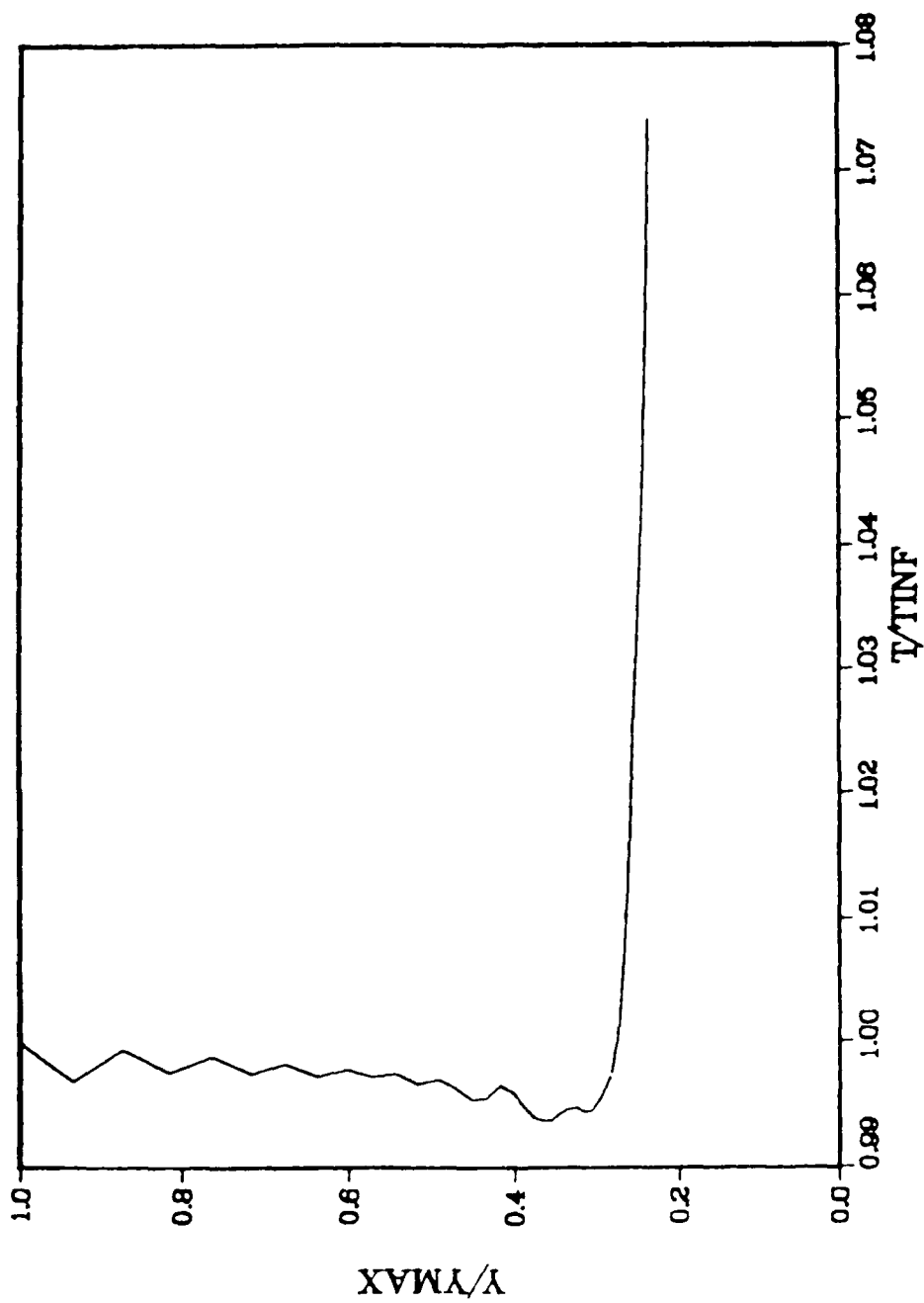
Figure 18. Temperature profile at K = 33.

51
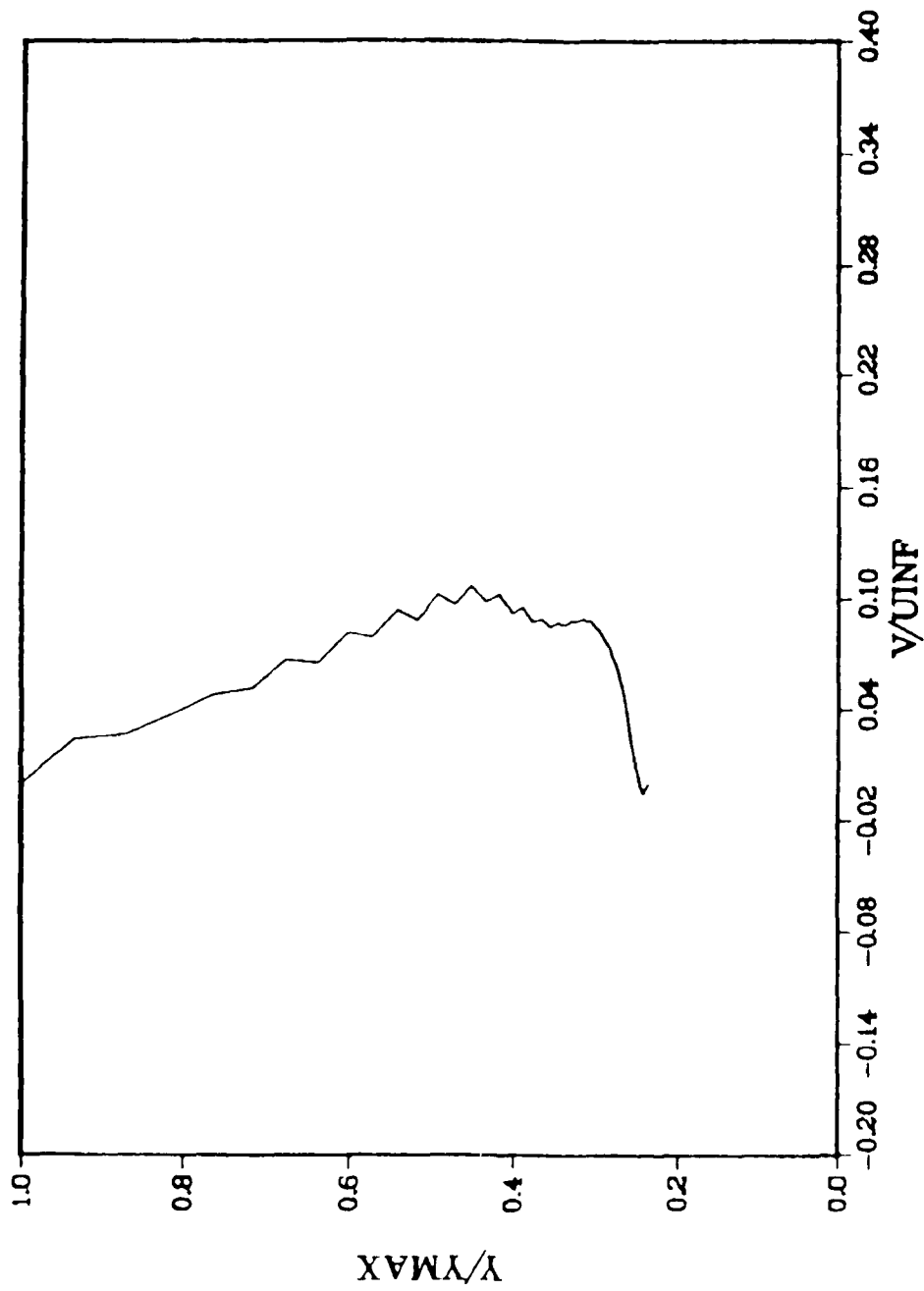
Figure 19. Vertical velocity profile at K = 33.

52
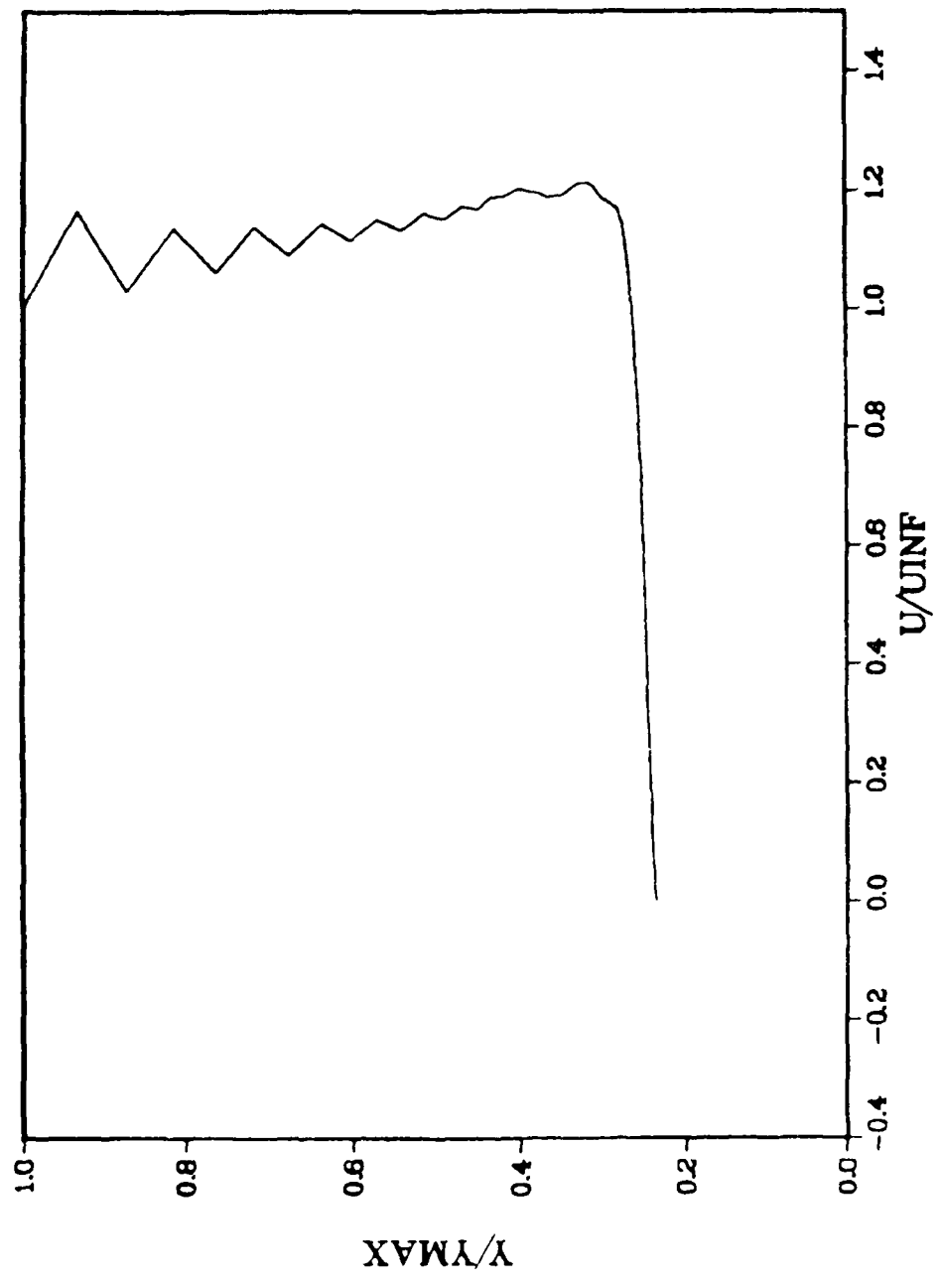
Figure 20. Horizontal velocity profile at K = 38.

53
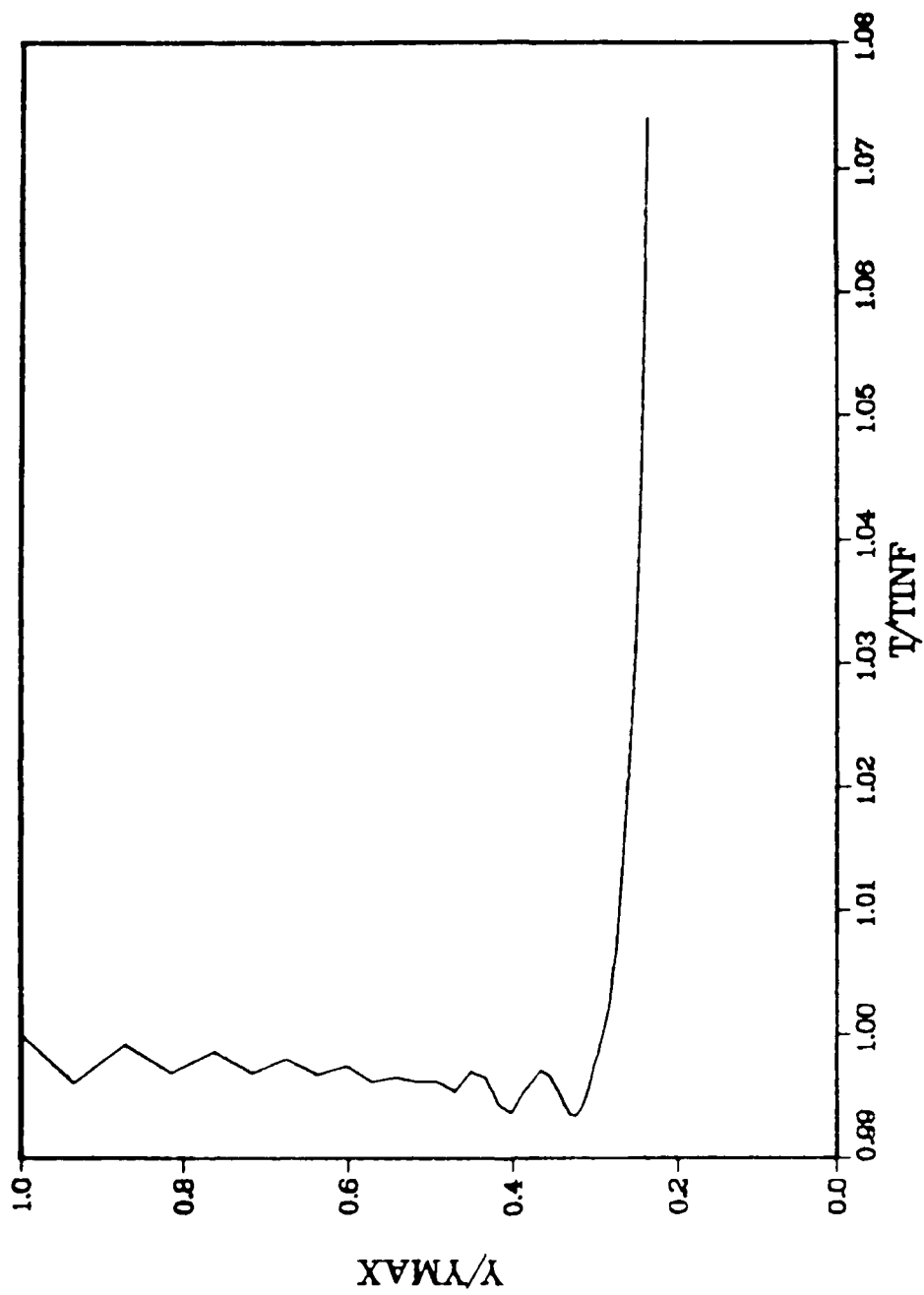
Figure 21. Temperature profile at K = 38.

54

V/UINF

0.40   0.34   0.28   0.22   0.16   0.10   0.04   -0.02   -0.08   -0.14   -0.20

Y/YMAX

1.0   0.8   0.6   0.4   0.2   0.0
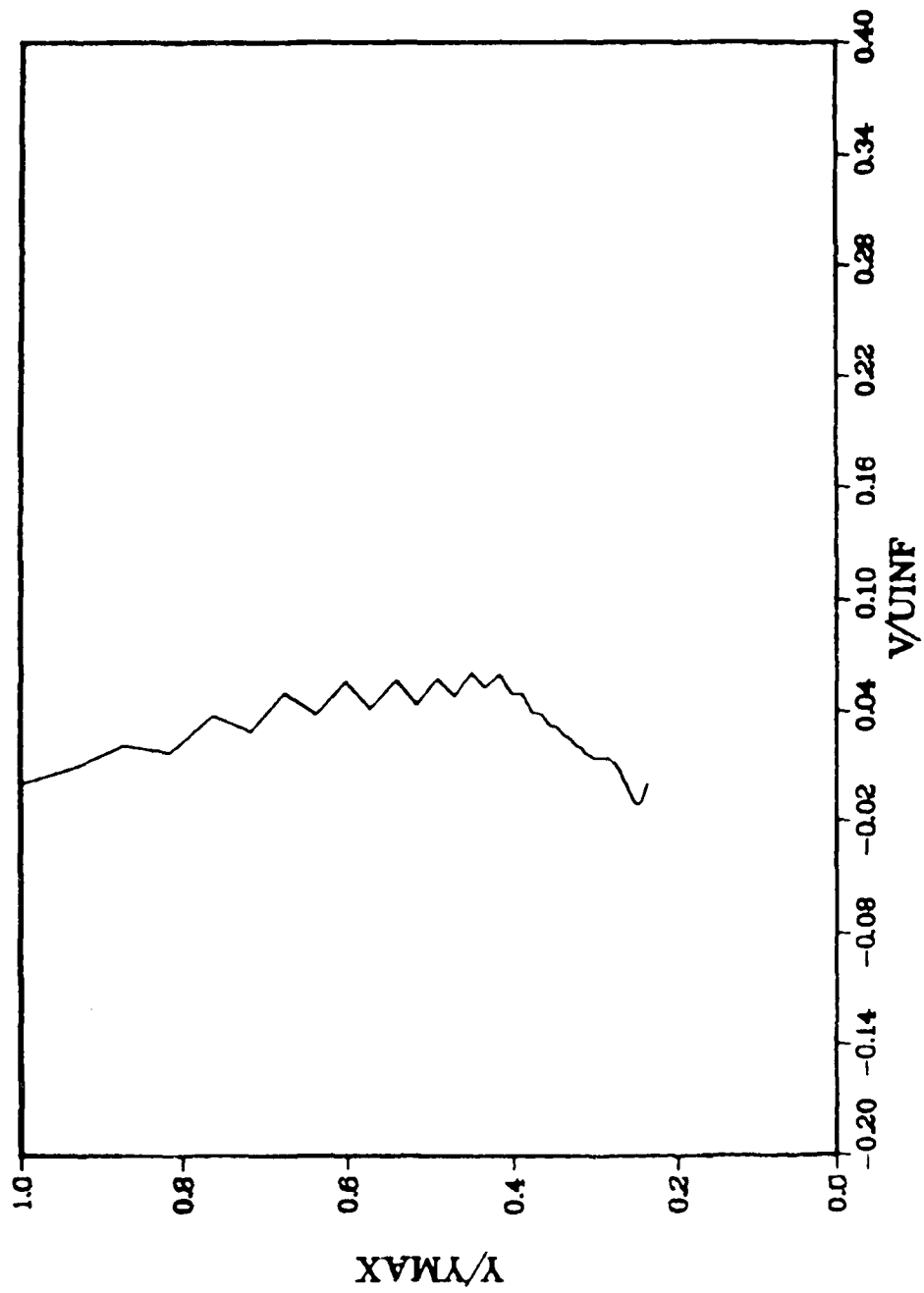
Figure 22. Vertical velocity profile at K = 38.

55
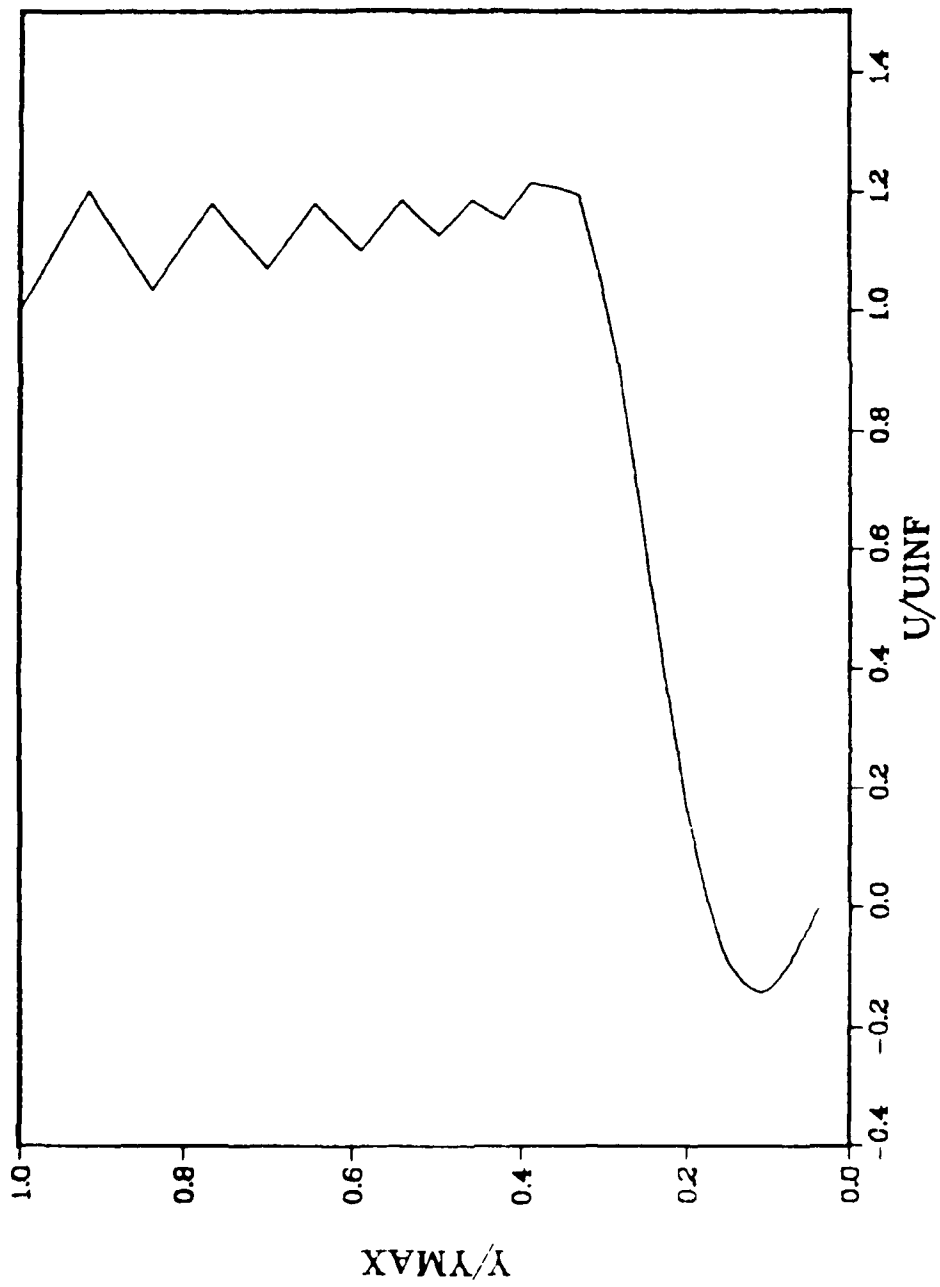
Figure 23. Horizontal velocity profile at K = 47.

56
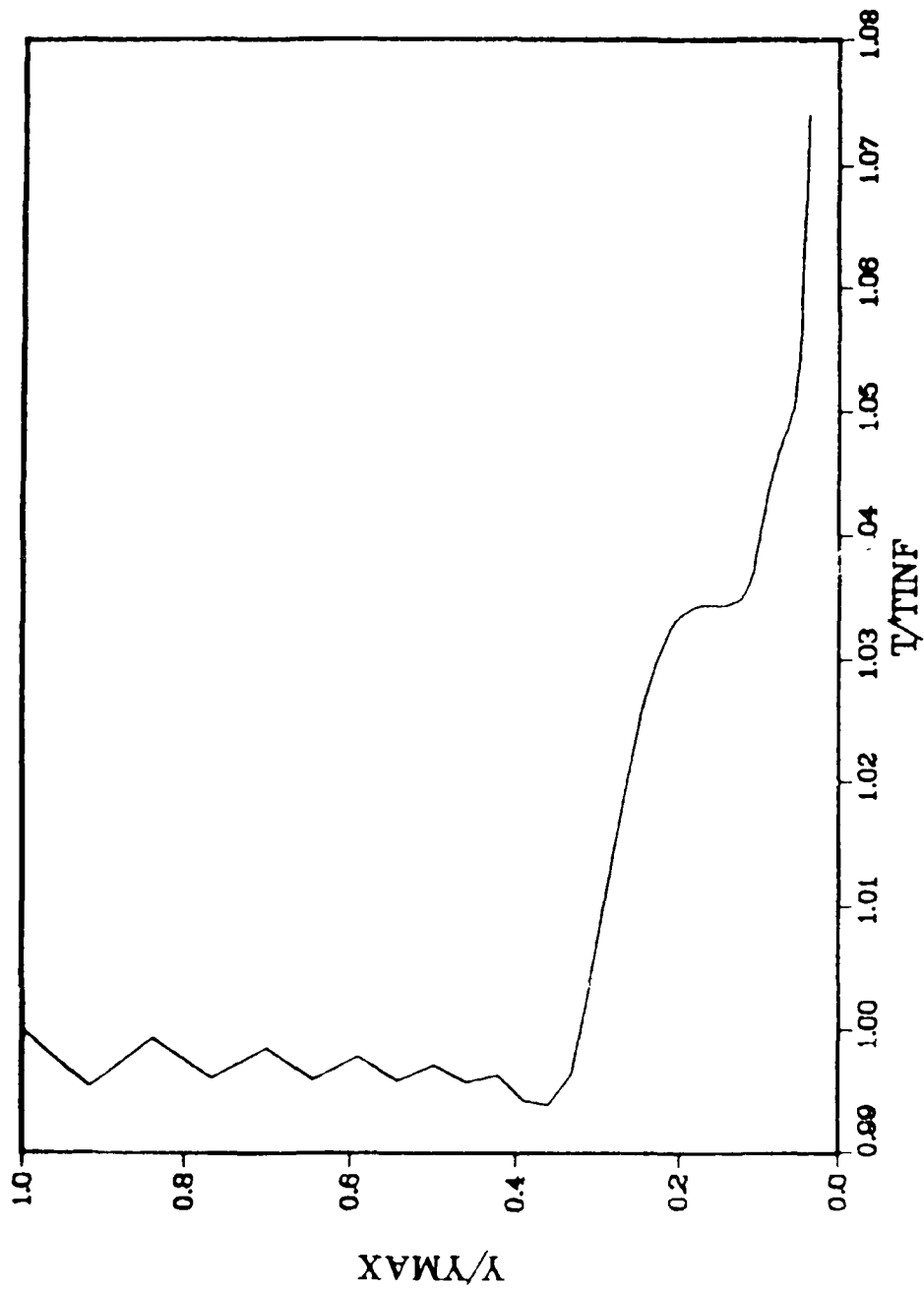
Figure 24. Temperature profile at K = 47.

57
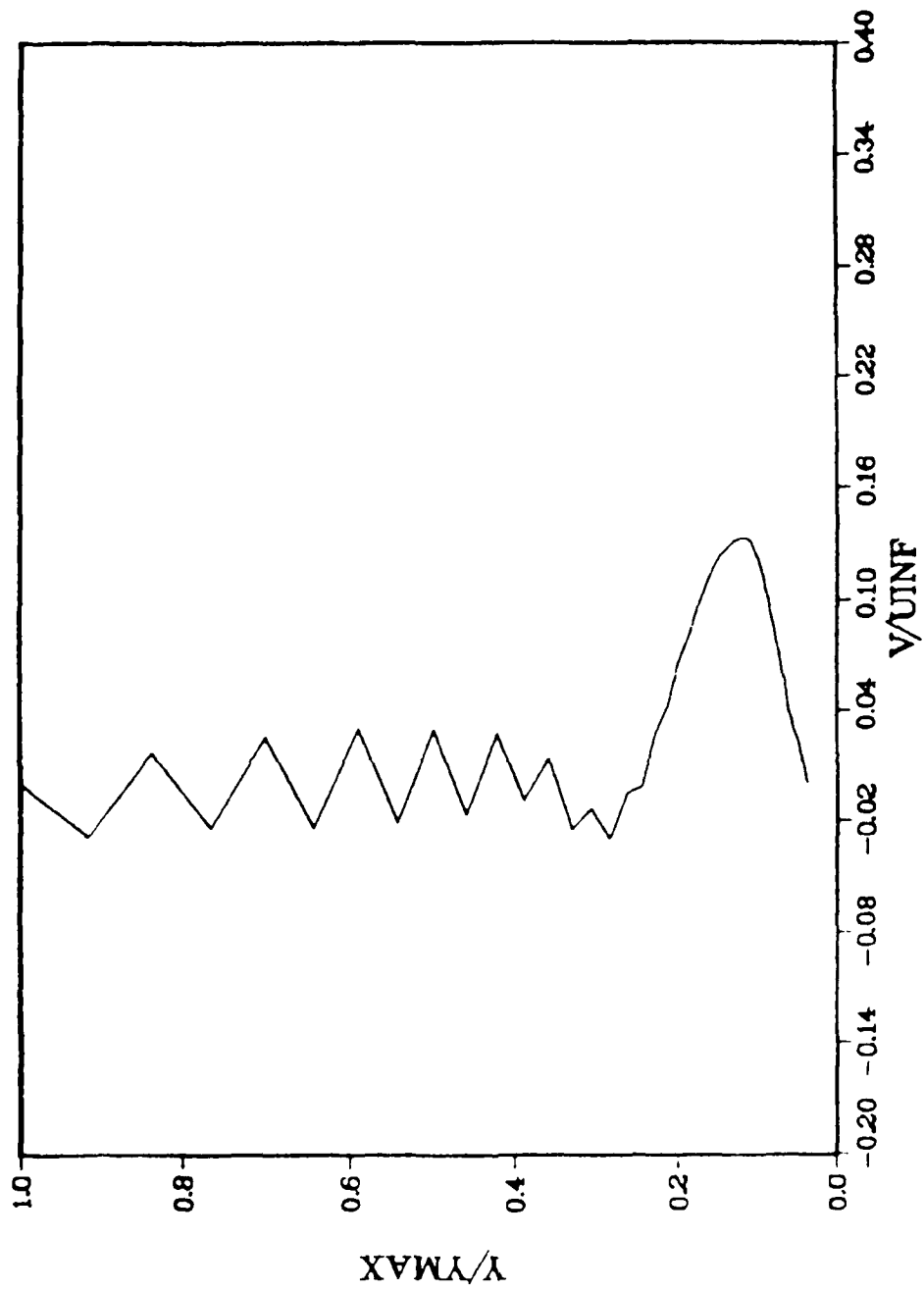
Figure 25. Vertical velocity profile at K = 47.

58

Figure 2b. Horizontal velocity profile at K = 57

59
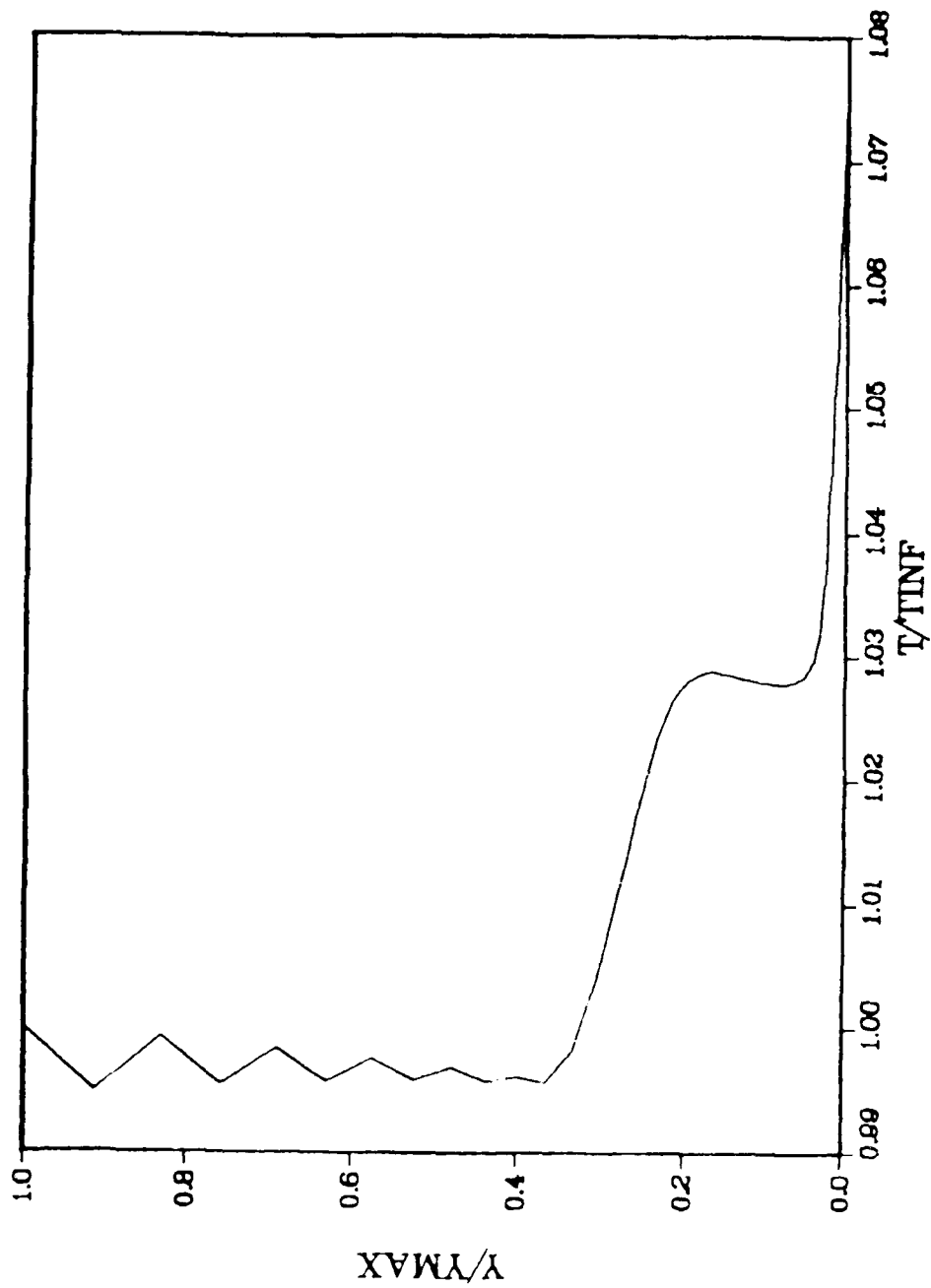
Figure 27. Temperature profile at K = 57.
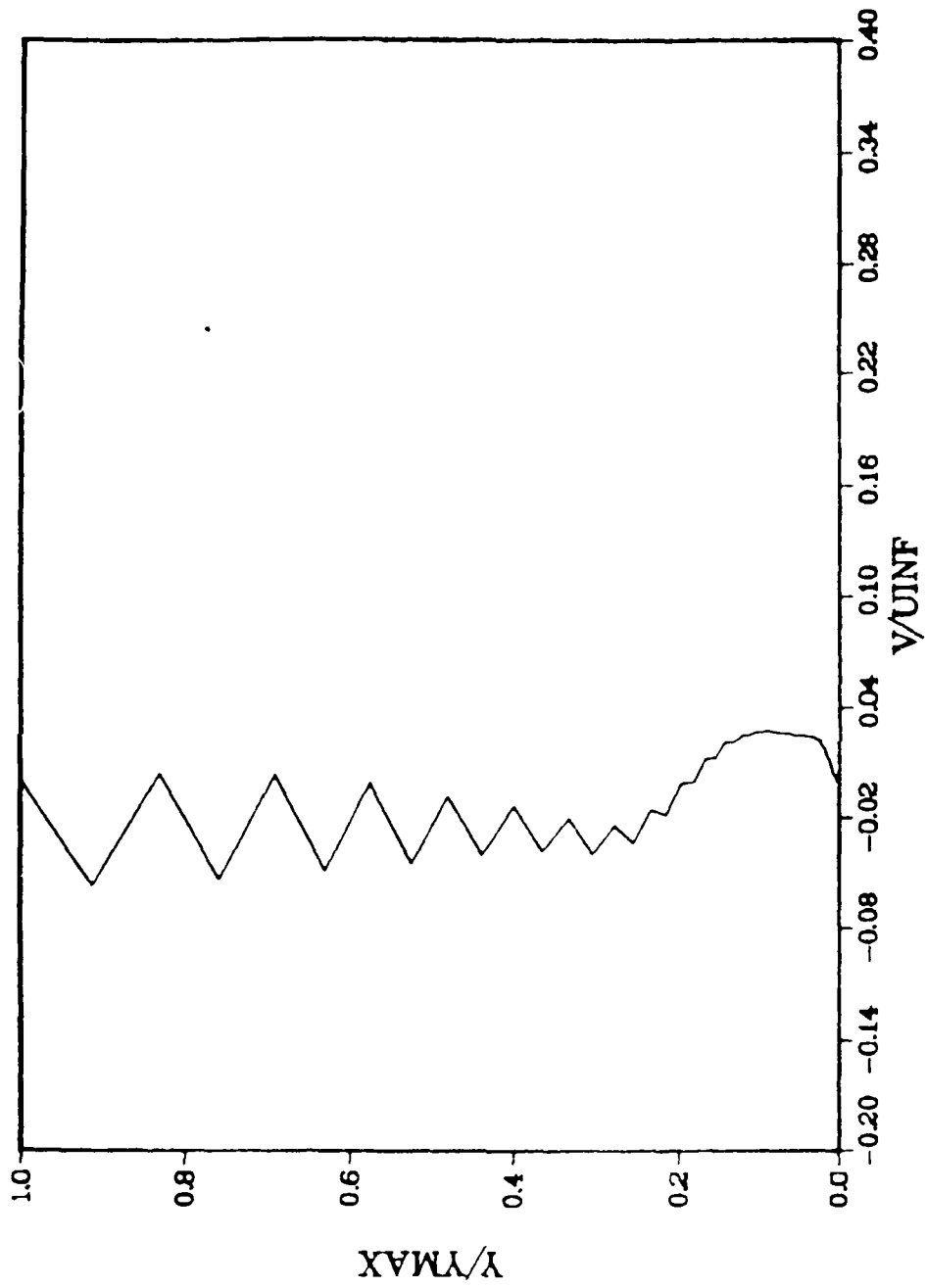
Figure 28. Vertical velocity profile at K = 57.
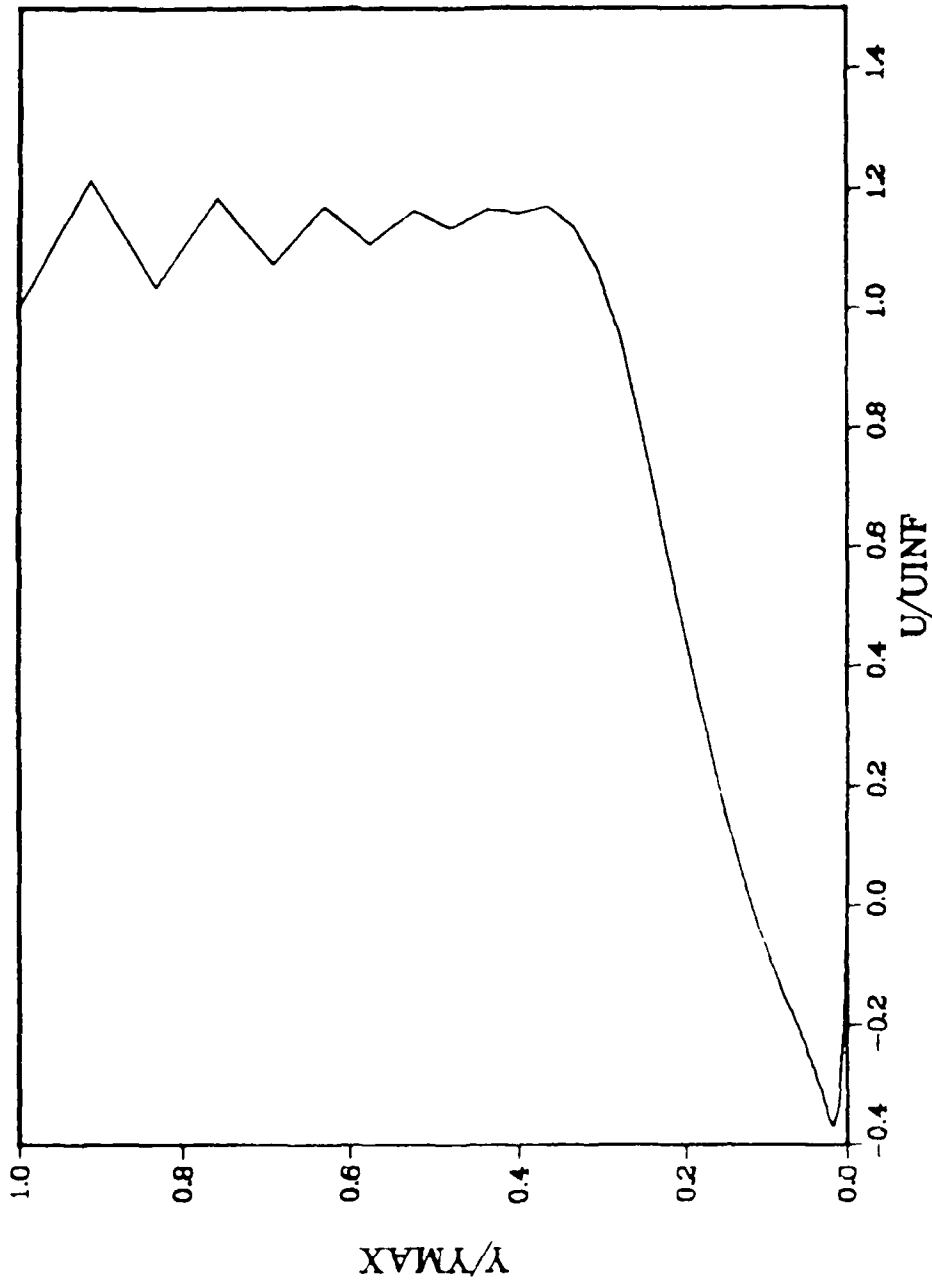
Figure 29. Horizontal velocity profile at K = 67.
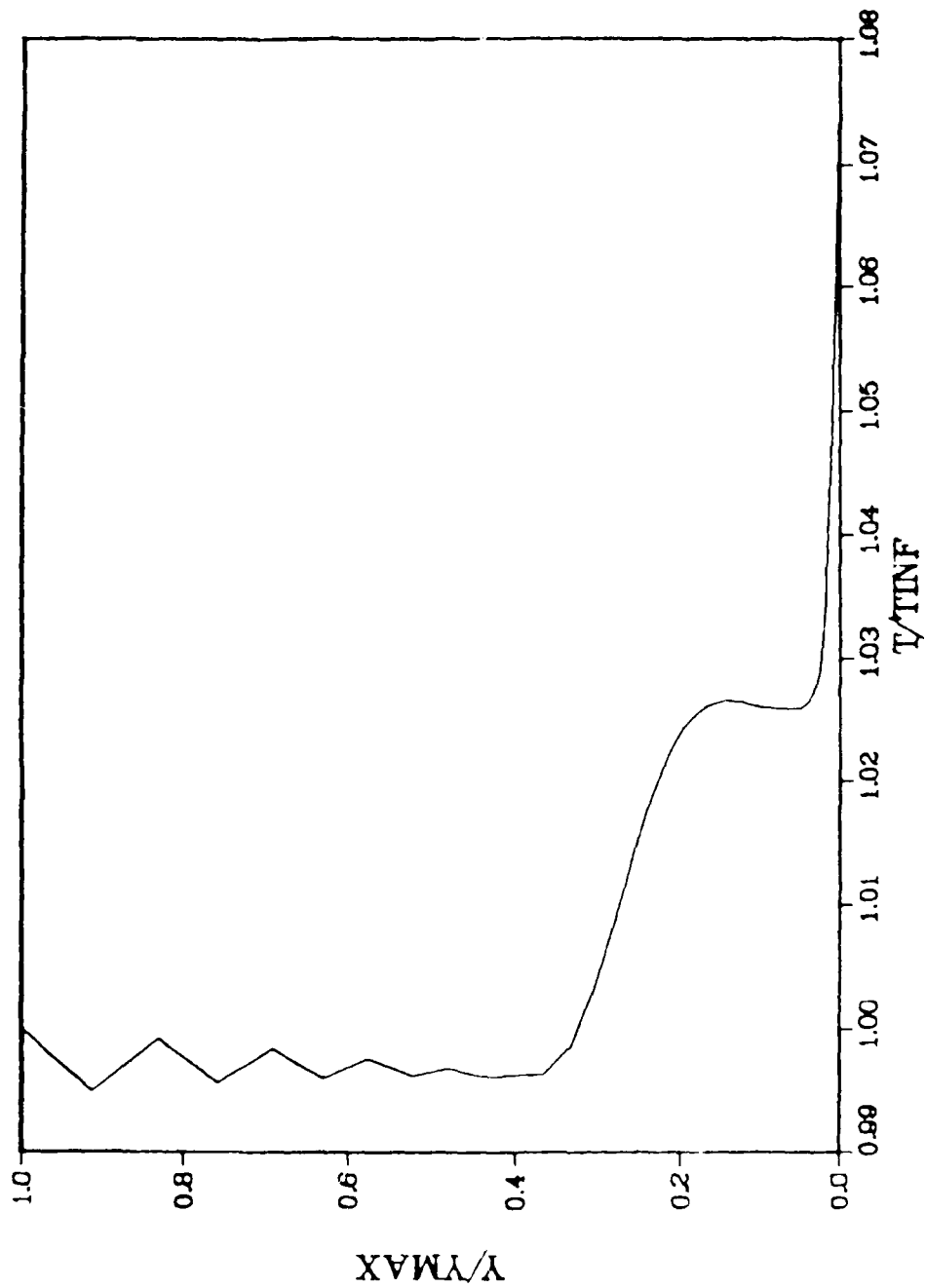
Figure 30. Temperature profile at K = 67.
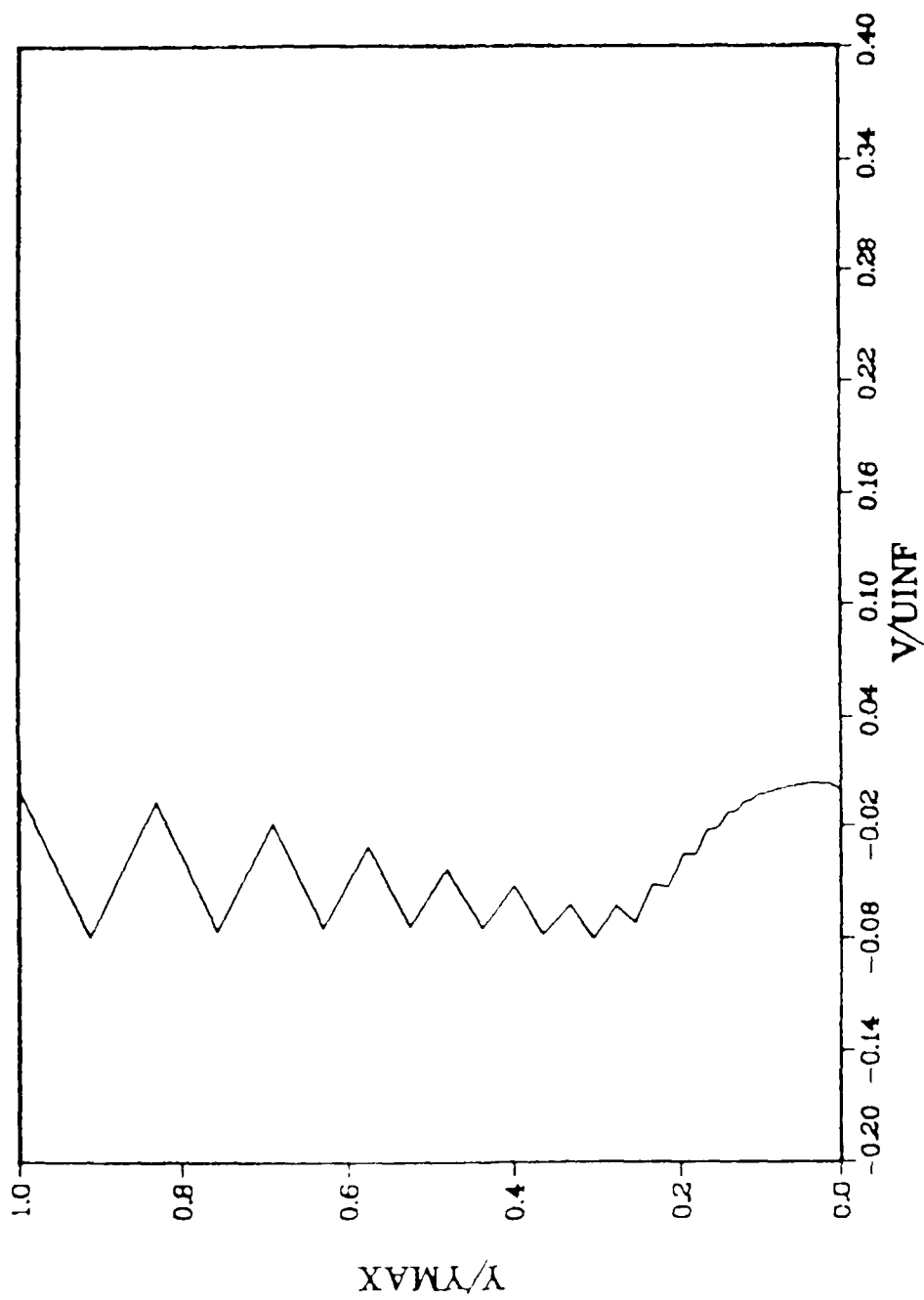
Figure 31. Vertical velocity profile at K = 67.
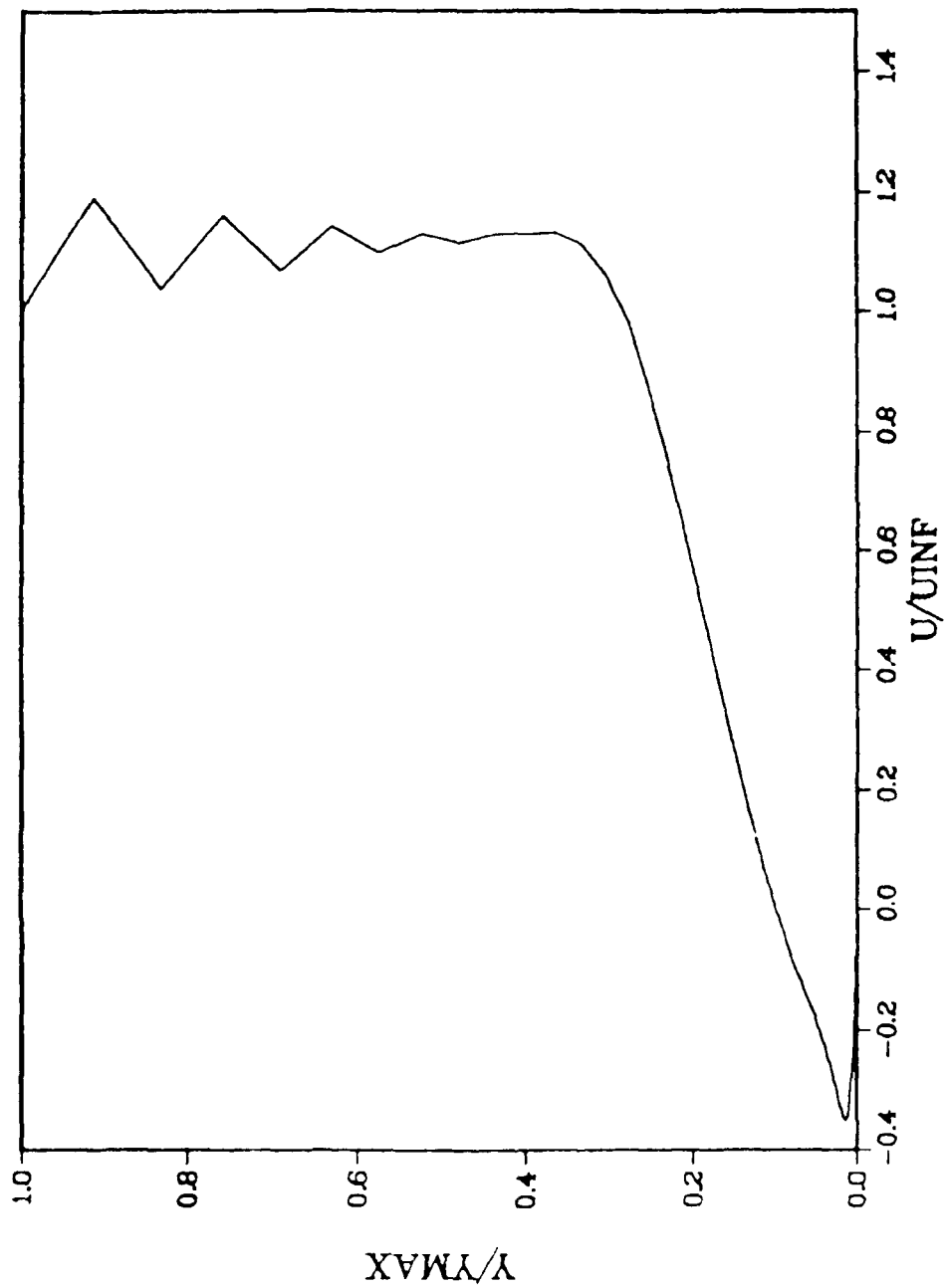
Figure 32. Horizontal velocity profile at K = 75.
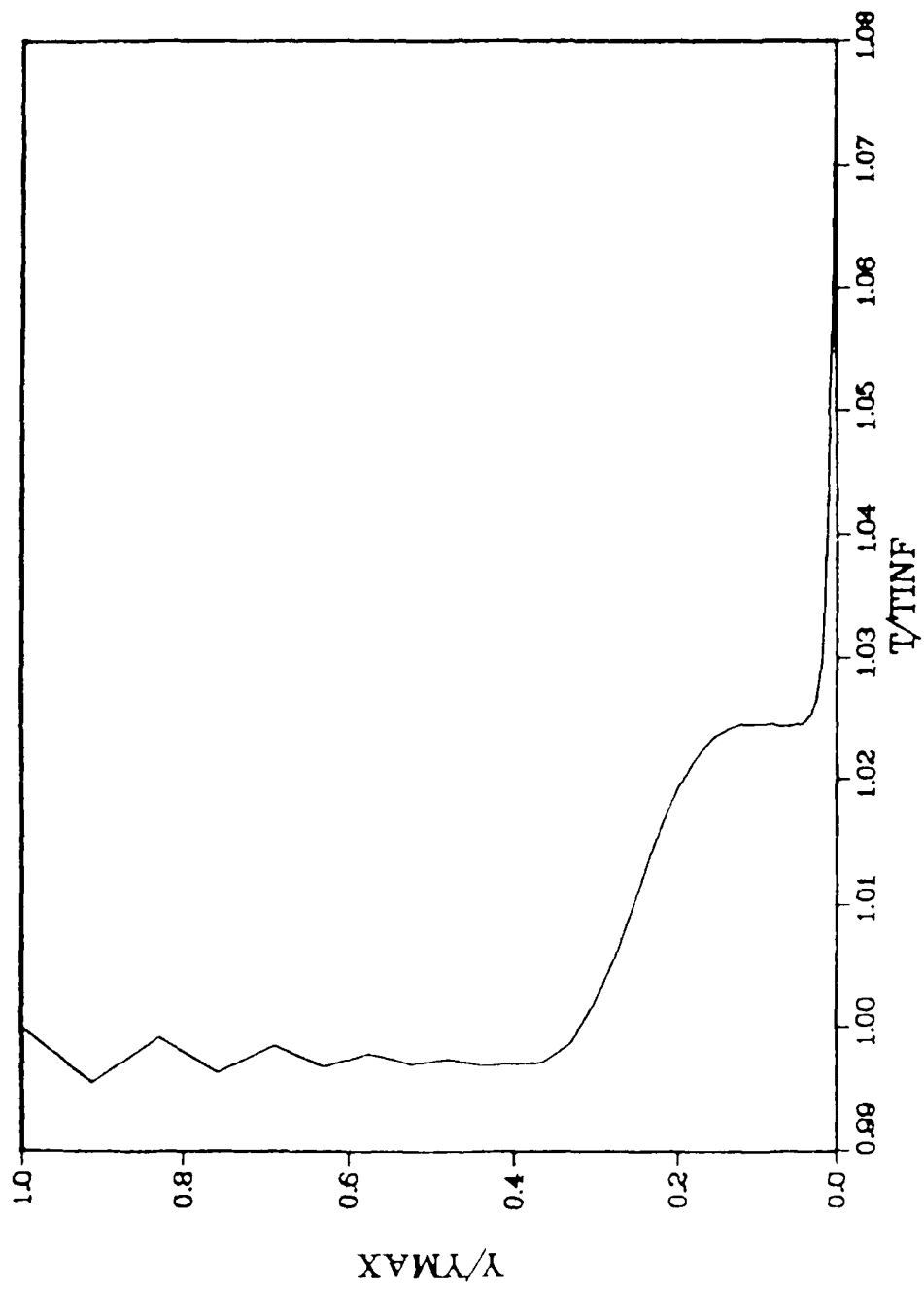
Figure 33. Temperature profile at K = 75.
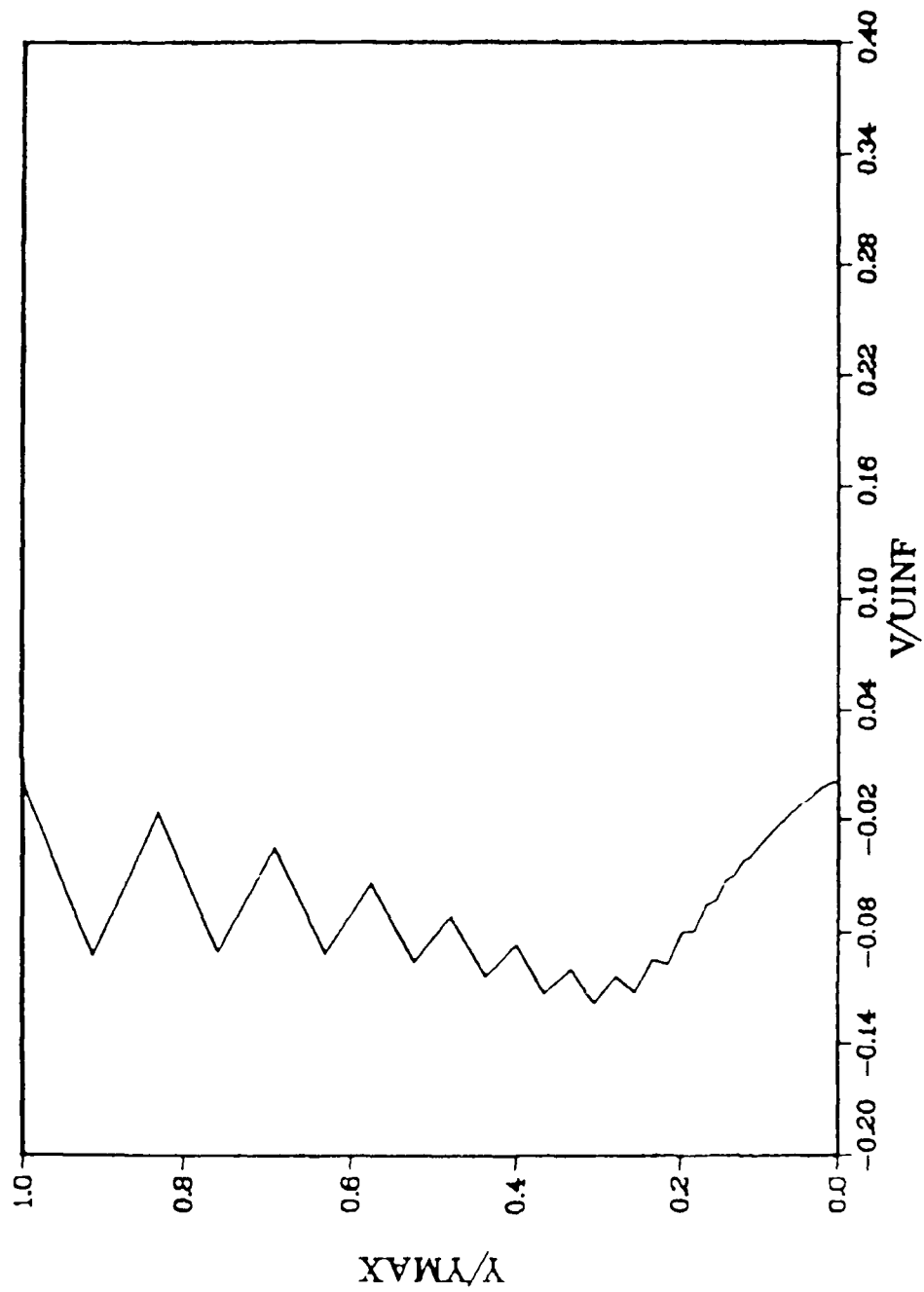
Figure 34. Vertical velocity profile at K = 75.
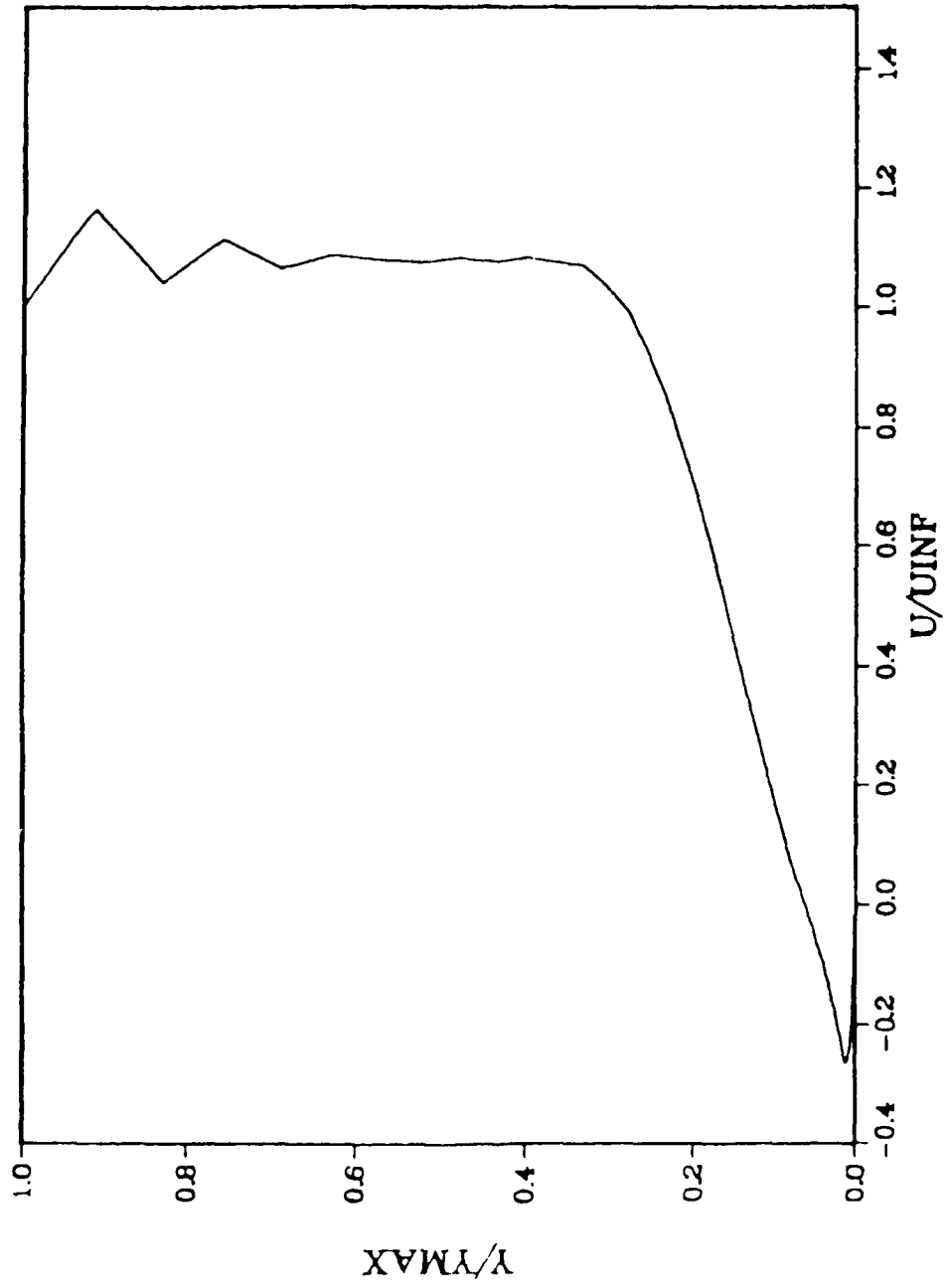
Figure 35. Horizontal velocity profile at K = 80.

68
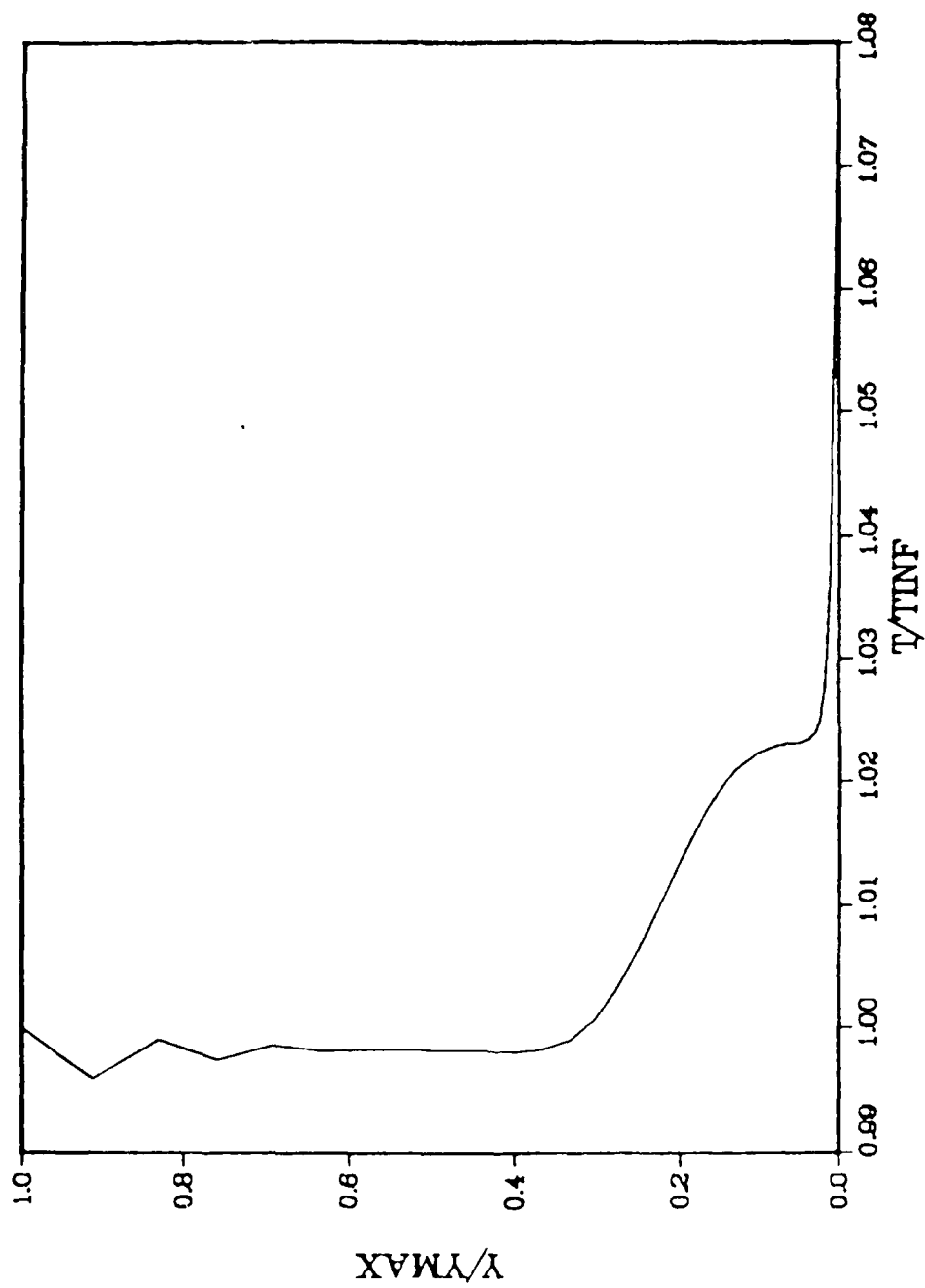
Figure 36. Temperature profile at K = 80.
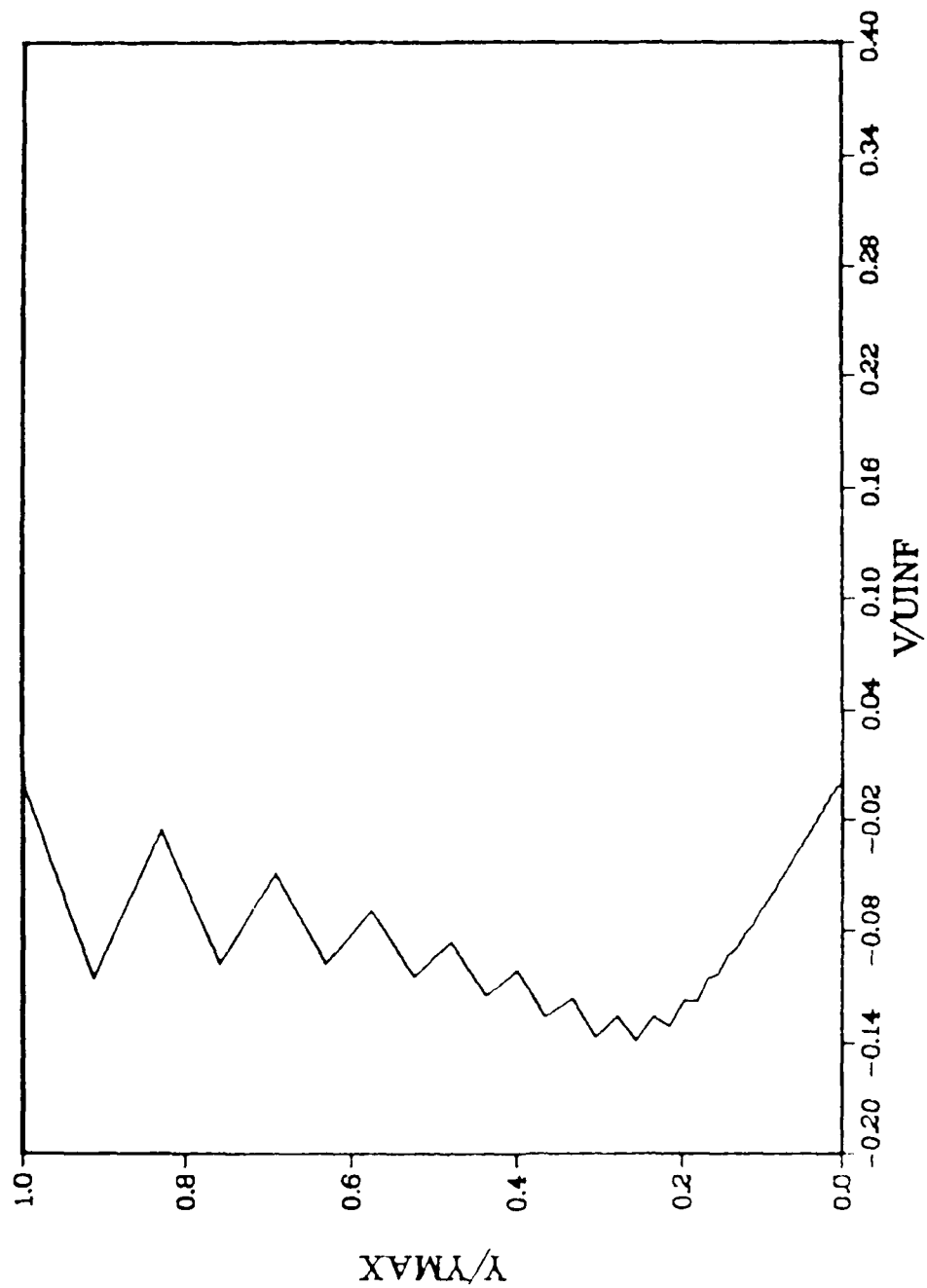
Figure 37. Vertical velocity profile at K = 80.
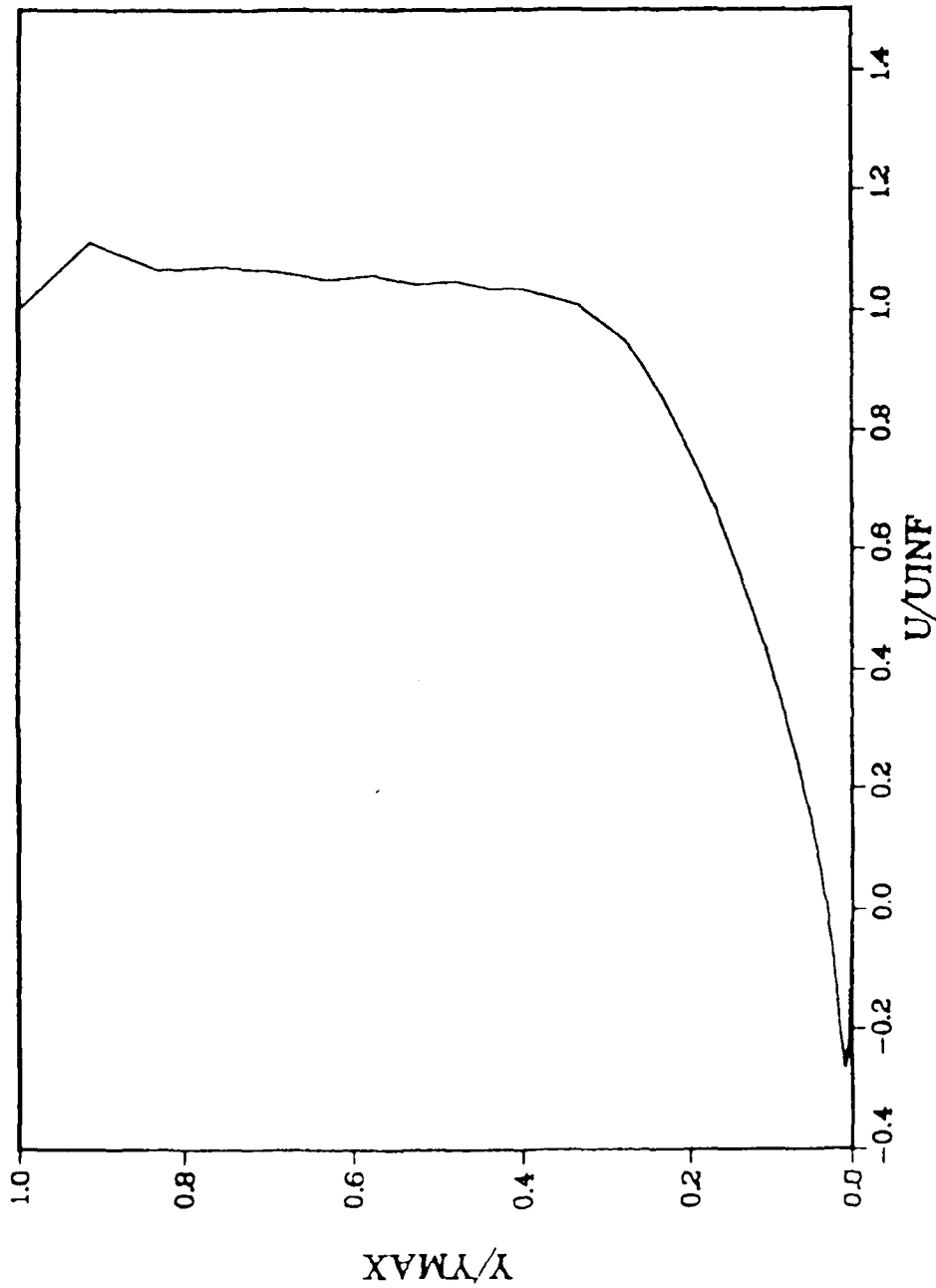
Figure 38. Horizontal velocity profile at K = 83.
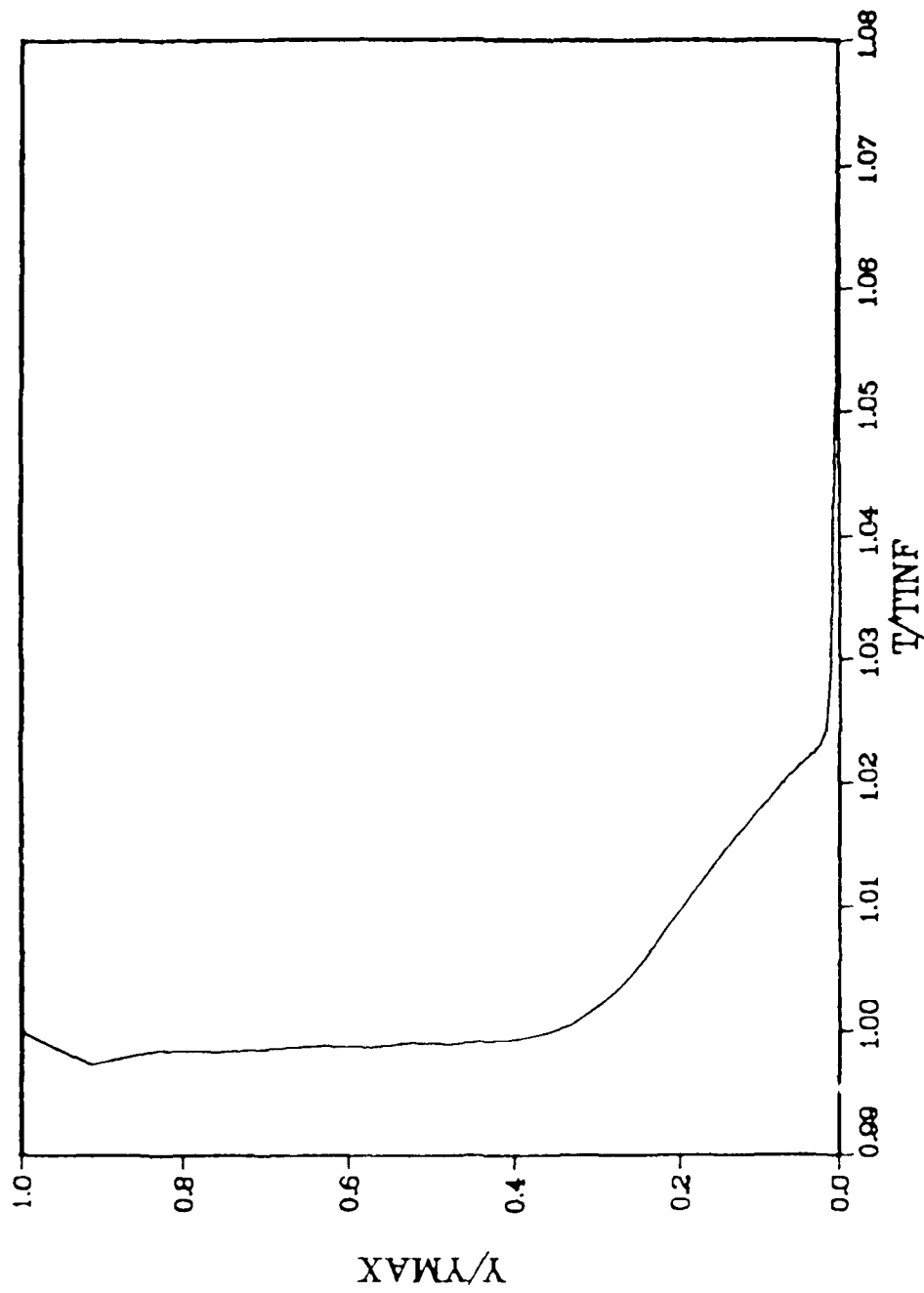
Figure 39. Temperature profile at K = 83.

72
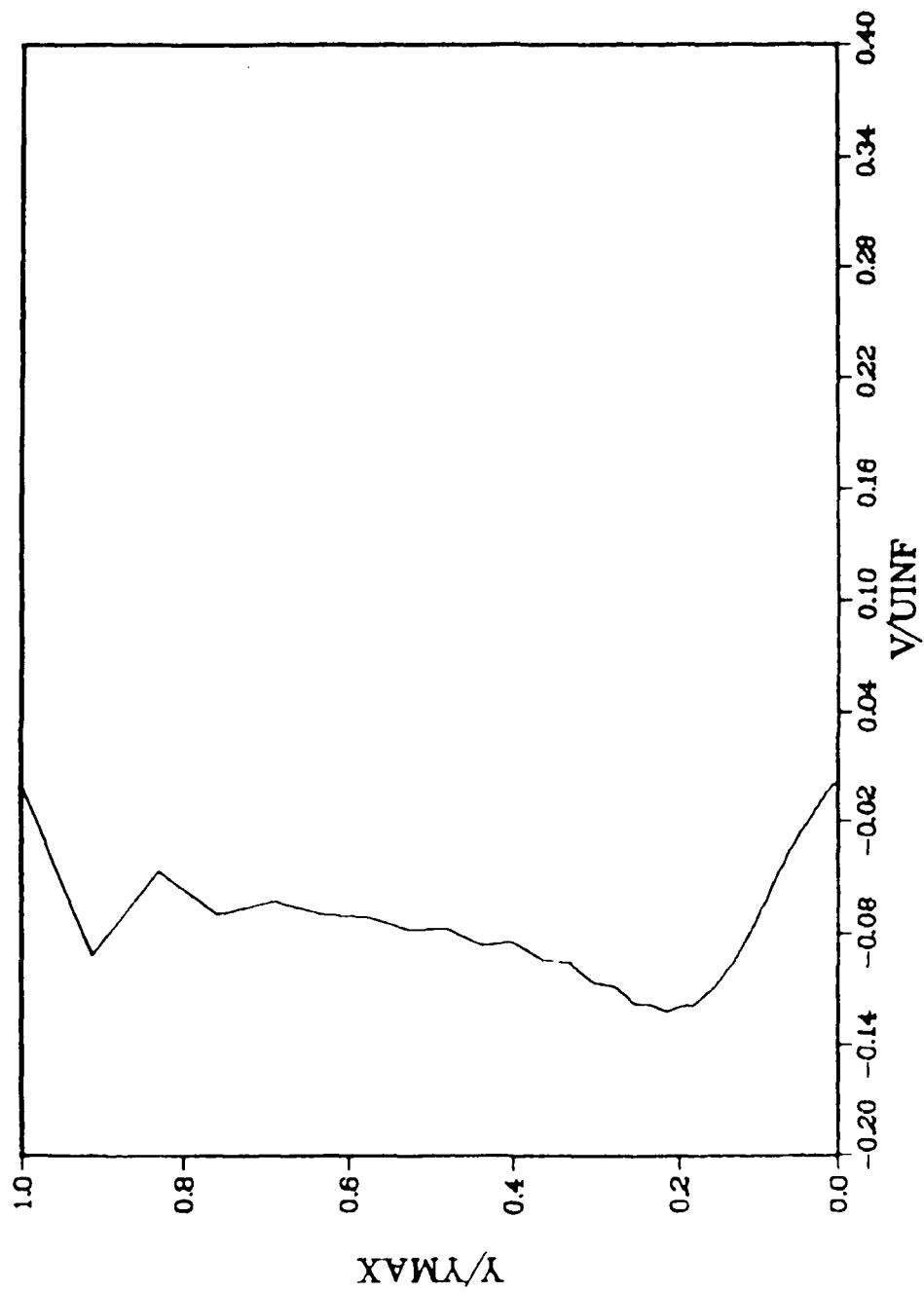
Figure 40. Vertical velocity profile at K = 83.

78
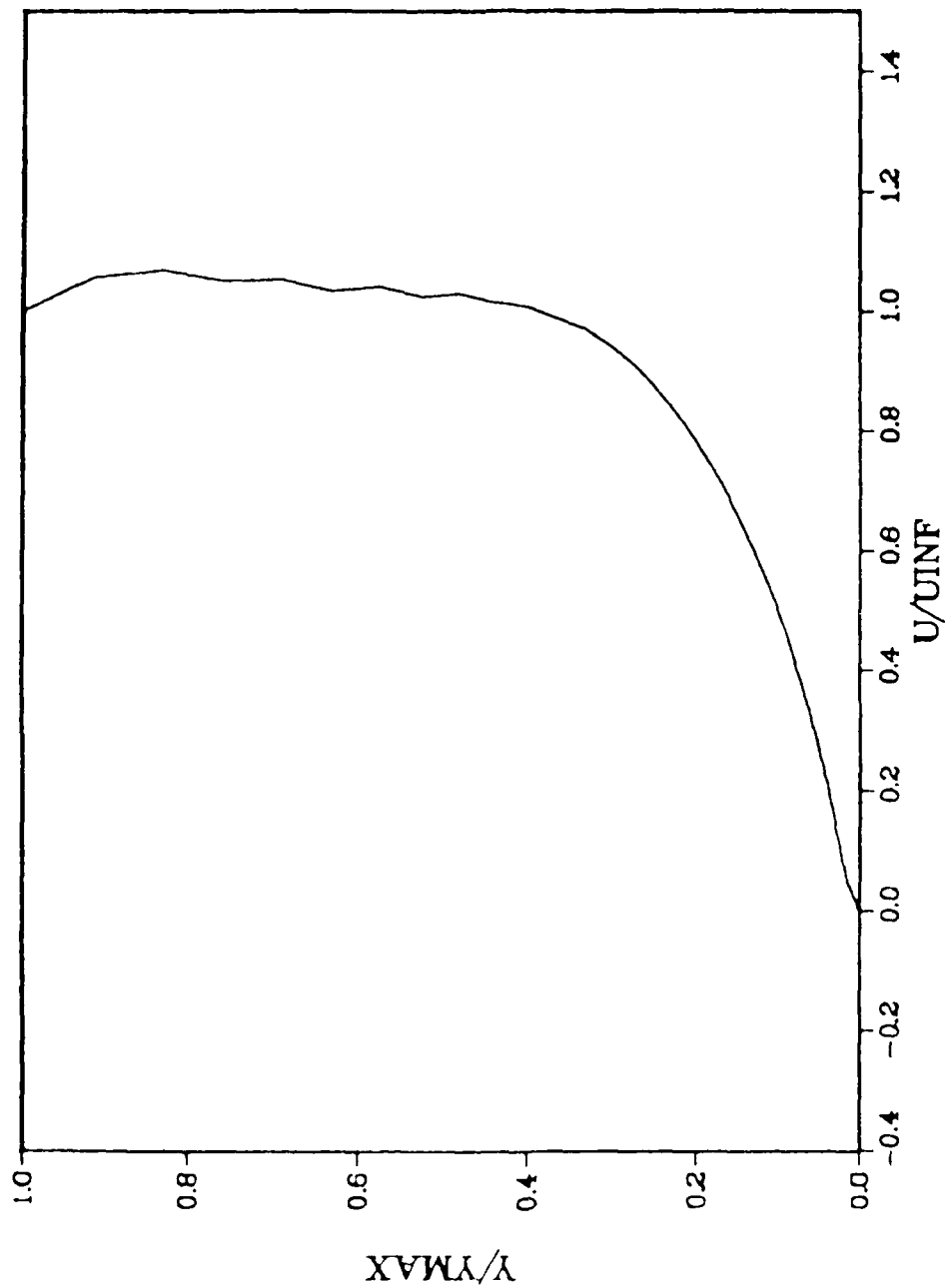
Figure 41. Horizontal velocity profile at K = 85.

76
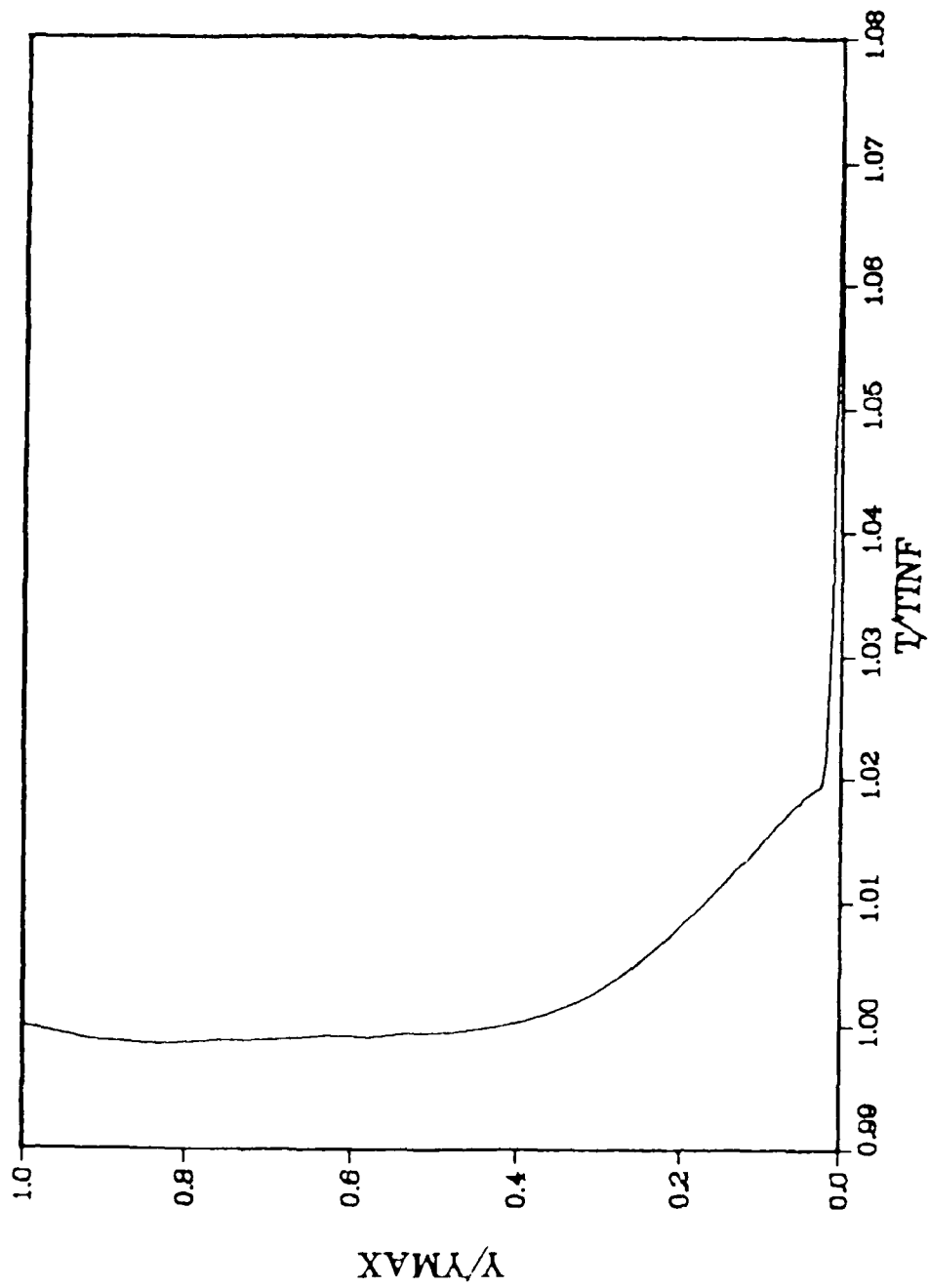
Figure 42. Temperature profile at K = 85.
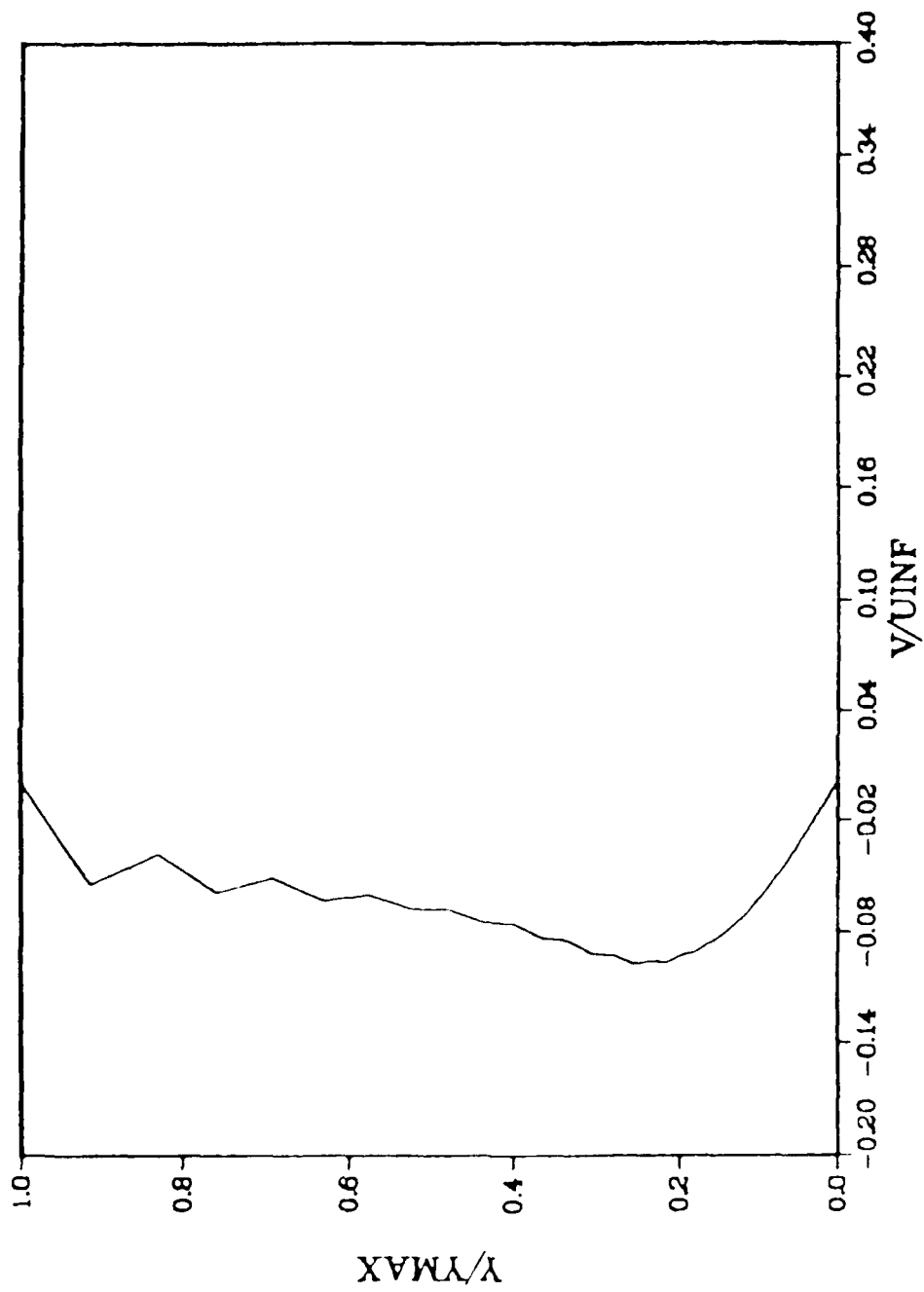
Figure 43. Vertical velocity profile at K = 85.
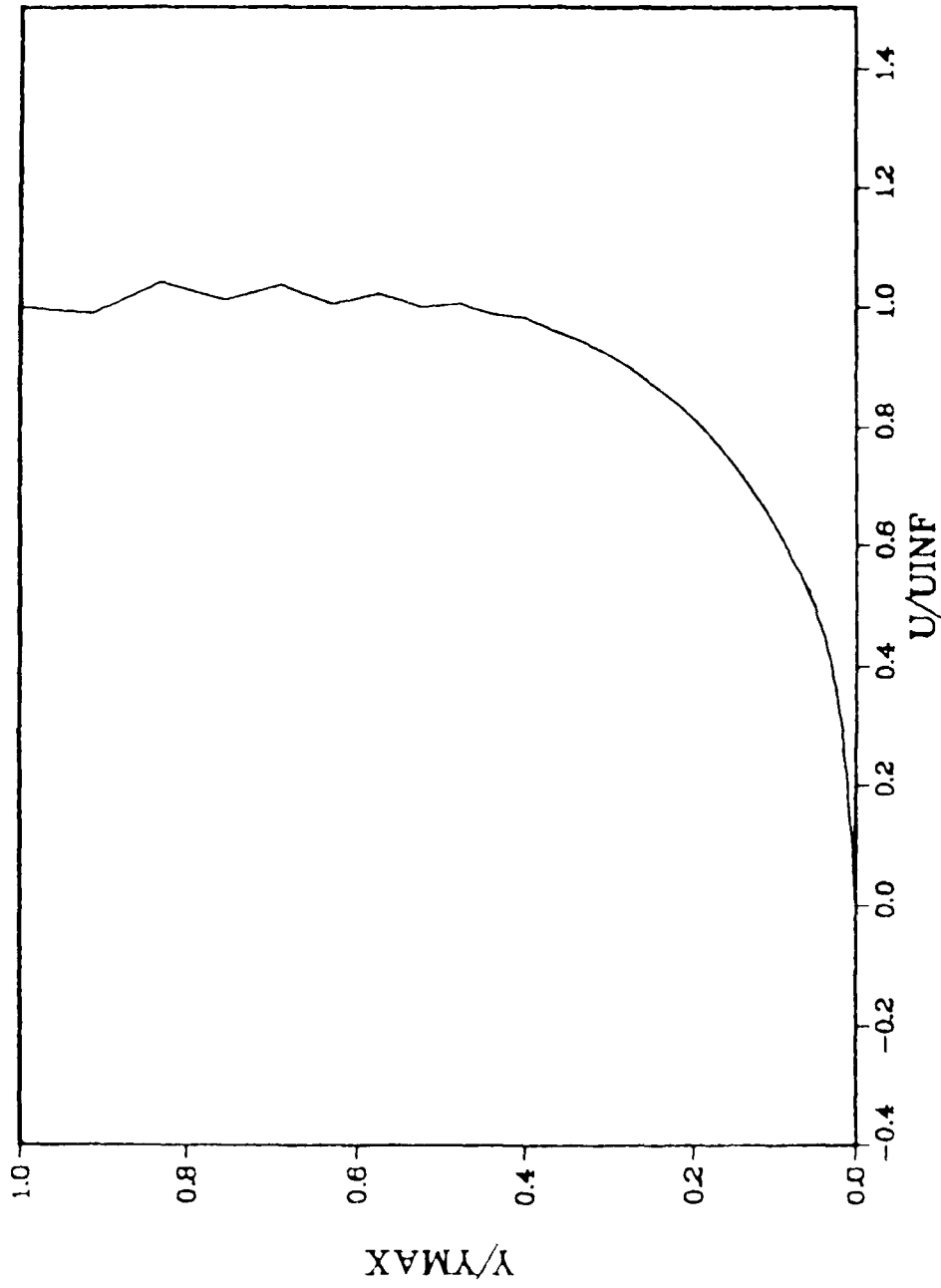
Figure 44. Horizontal velocity profile at K = 89.
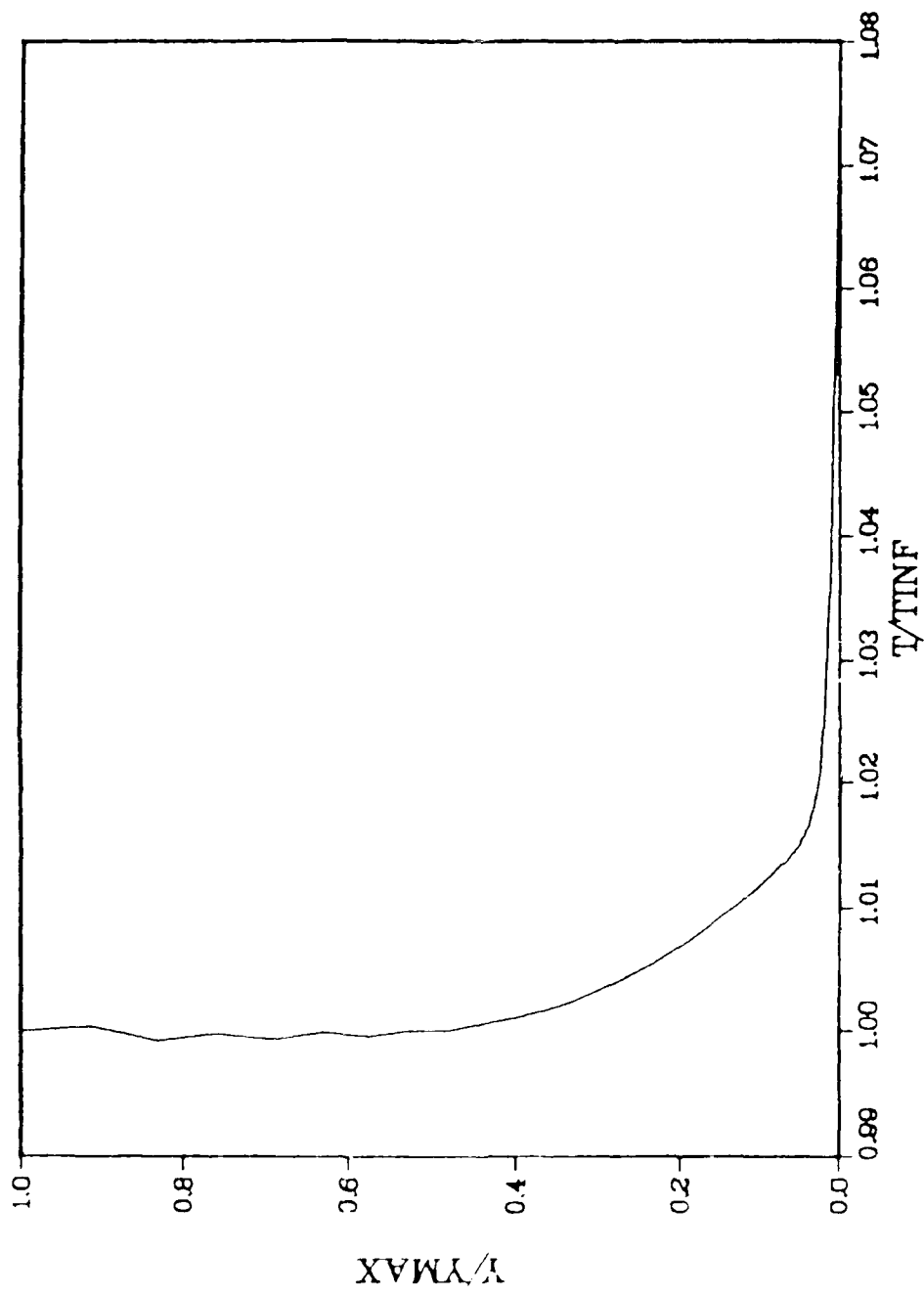
Figure 45. Temperature profile at K = 89.
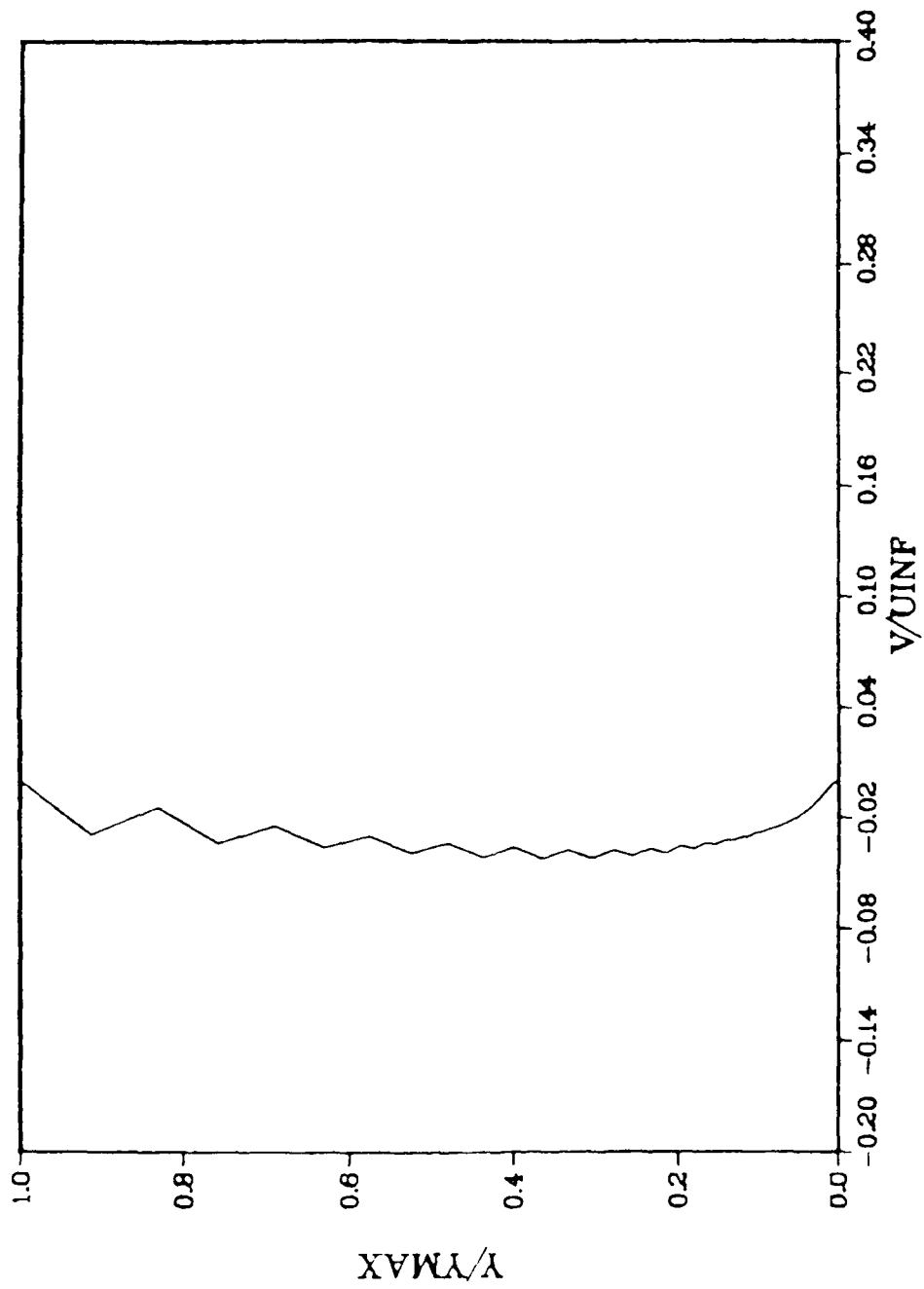
Figure 46. Vertical velocity profile at K = 89.
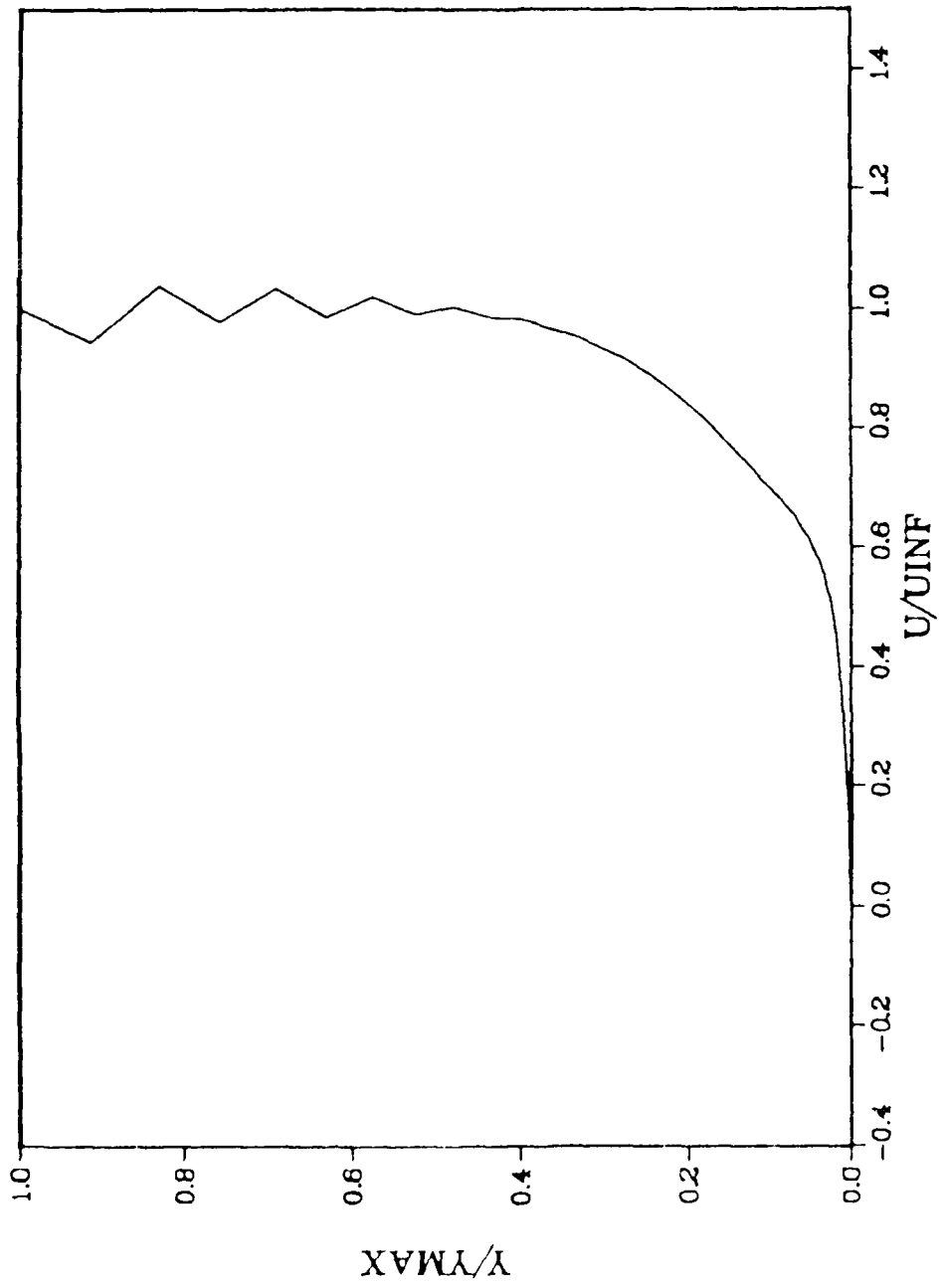
Figure 47. Horizontal velocity profile at K = 100.
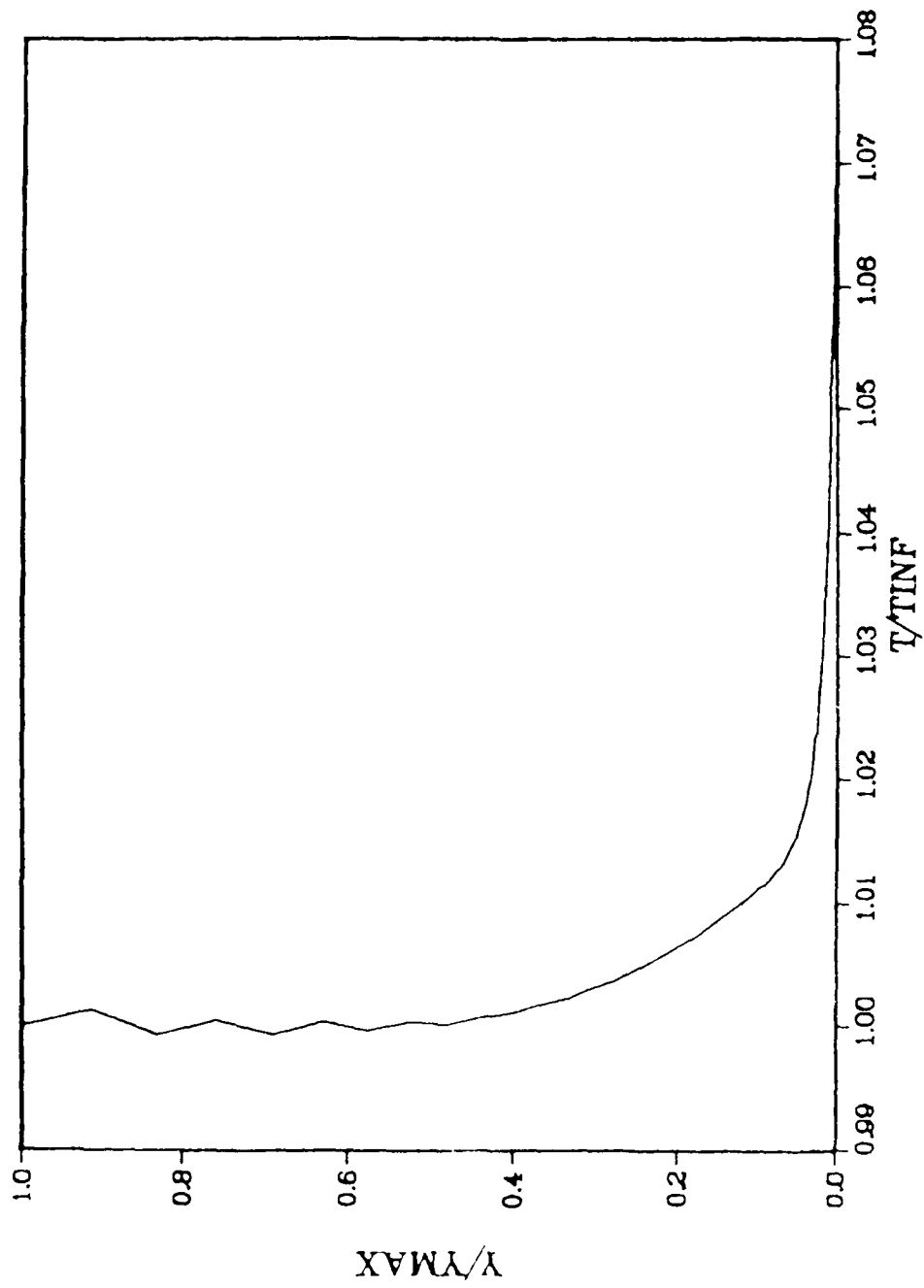
Figure 48. Temperature profile at K = 100.
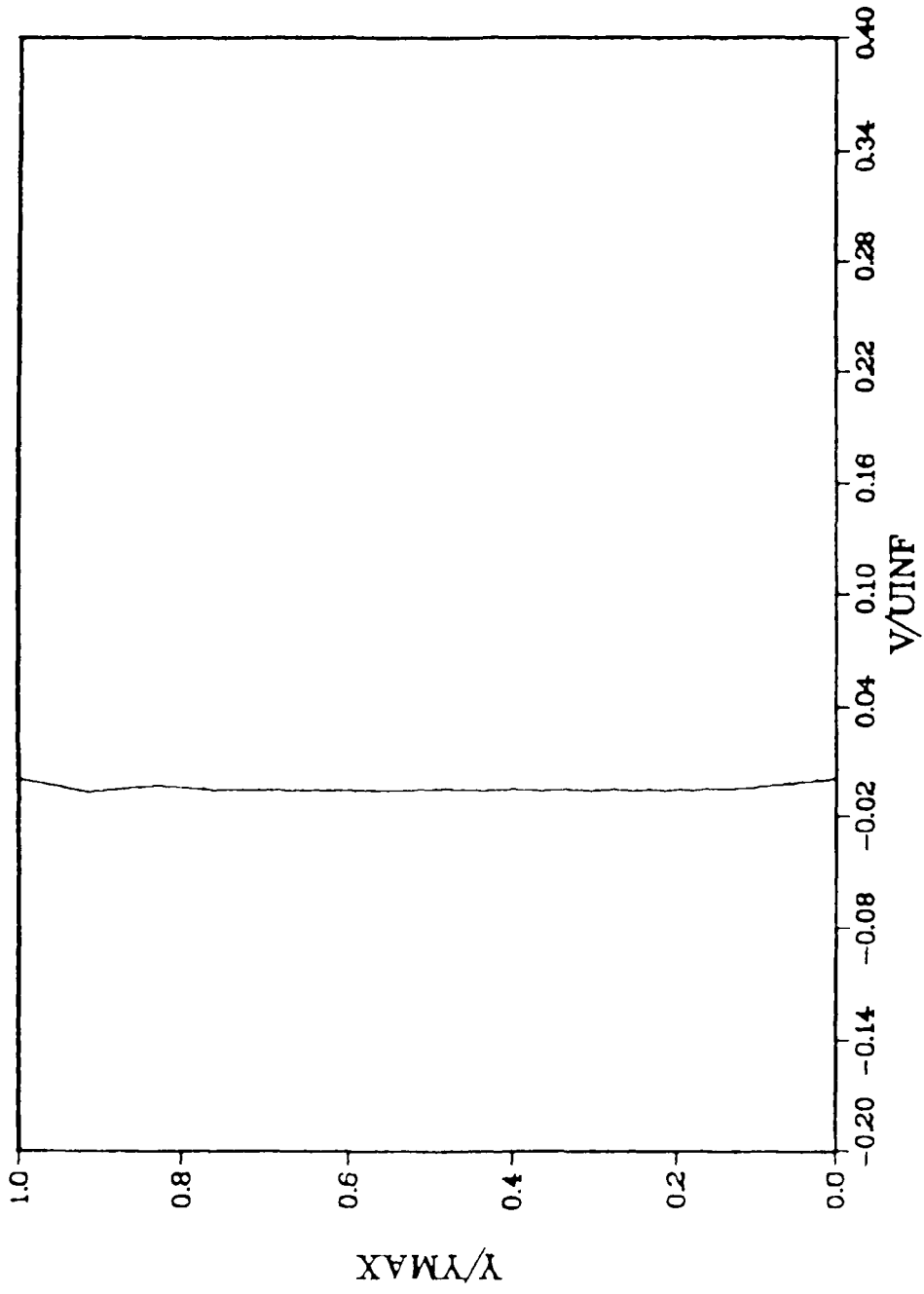
Figure 49. Vertical velocity profile at K = 100.
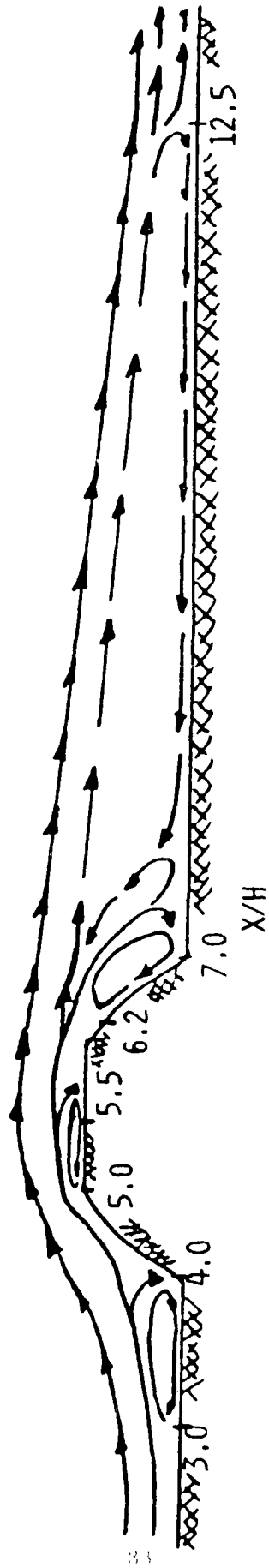
Figure 50. Calculated streamlines near the turbulator.
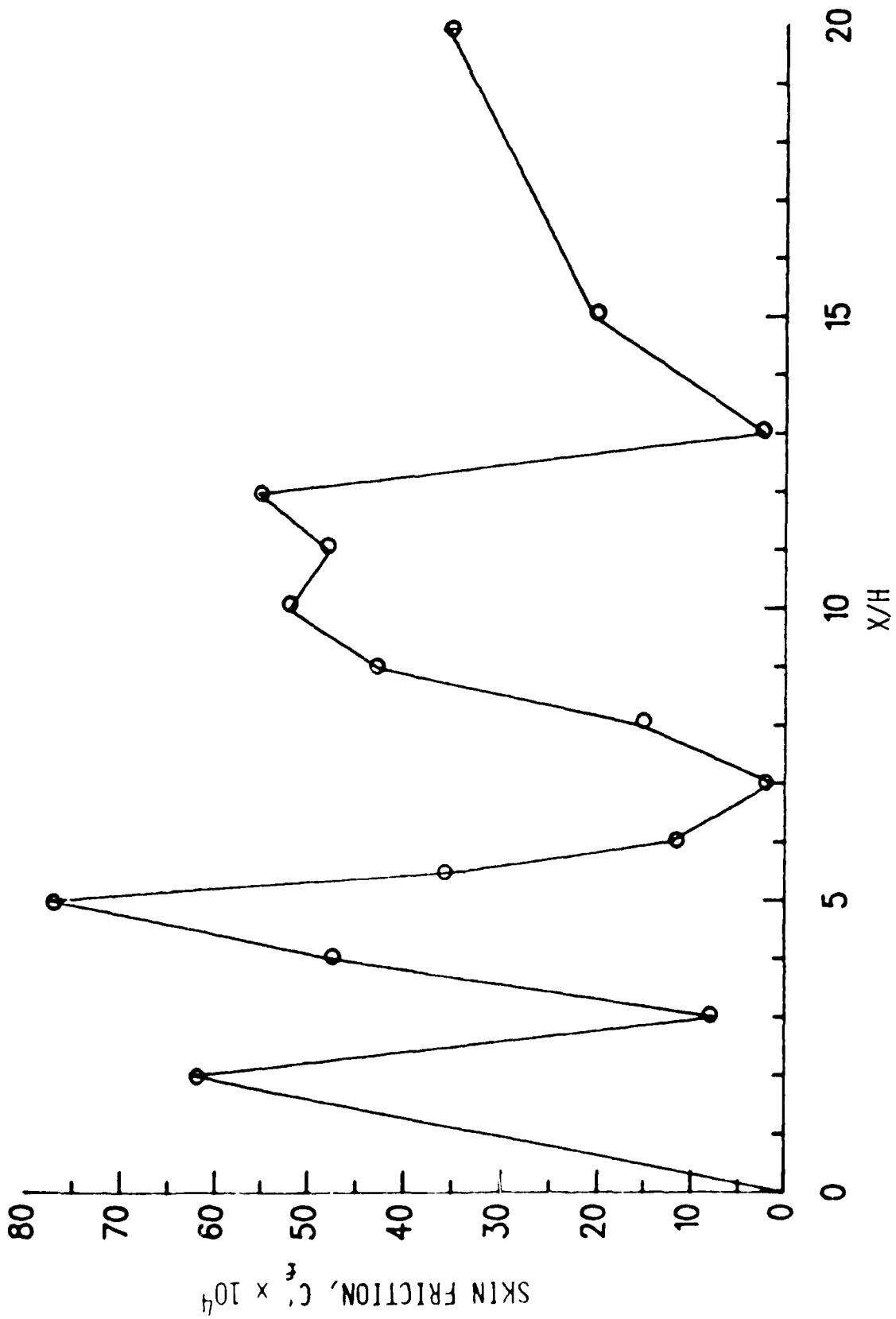
Figure 51. Calculated axial distribution of local skin friction.

SKIN FRICTION, $C_f' \times 10^4$

X/H
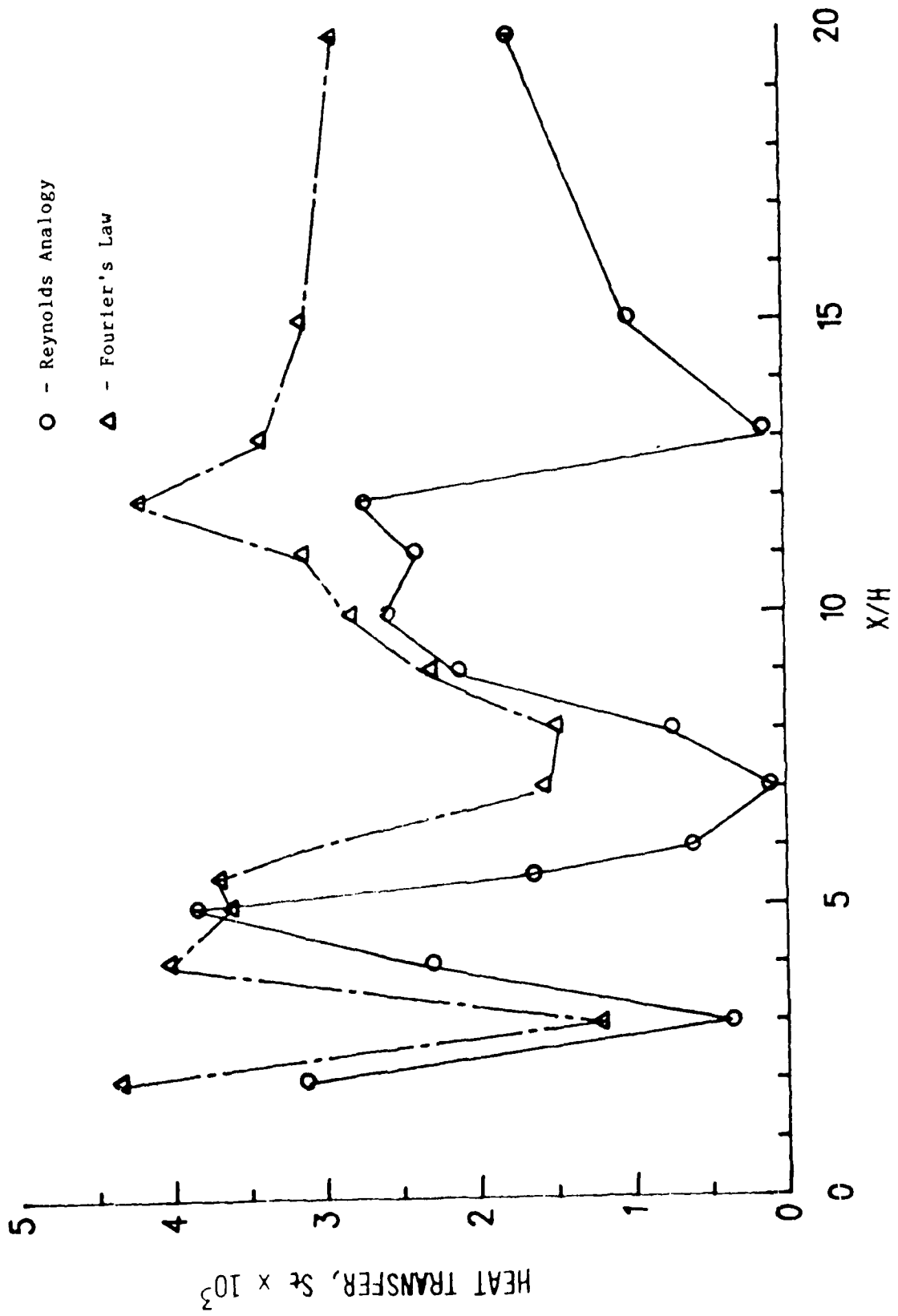
Figure 52. Calculated axial distribution of local heat transfer rate.

HEAT TRANSFER, St × 10³

X/H

O – Reynolds Analogy

△ – Fourier's Law